Spatiotemporal Analysis of Rainfall Erosivity and Climate Change Impact Assessment

Submitted in partial fulfilment of requirement for the degree of

Doctor of Philosophy

by

TAPASRANJAN DAS
(Roll No. – 176104104)

Under the guidance of

Prof. ARUP KUMAR SARMA

DEPARTMENT OF CIVIL ENGINEERING

INDIAN INSTITUTE OF TECHNOLOGY GUWAHATI

JANUARY 2026

DECLARATION

I, **Tapasranjan Das**, author of the Ph.D thesis **“Spatiotemporal Analysis of Rainfall Erosivity and Climate Change Impact Assessment”** would like to certify that

- The work presented in this thesis is original research work carried out by me.
- The research work has not been submitted for any degree or diploma or any other qualification either in this institute or in any other university.
- Whenever I have used resources [theory, concepts, texts, data, graphs, figures or any other things of similar nature] from other sources, a due credit by citing in the text of the thesis is clearly made.
- The work presented here is free from plagiarism to the best of my knowledge, and I take the responsibility for any issues.
- I also affirm that thesis supervisor is not responsible for any possible instance of plagiarism within this submitted work.

[TAPASRANJAN DAS]
(176104104)

Department of Civil Engineering
Indian Institute of Technology Guwahati
Guwahati – 781039, Assam India

CERTIFICATE

This is to certify that the work describes in this thesis entitled **"Spatiotemporal Analysis of Rainfall Erosivity and Climate Change Impact Assessment"** submitted by **Tapasranjan Das (Roll No. 176104104)** in partial fulfilment of the requirements for the award of the degree of Doctor of Philosophy is an authentic record of the results obtained from the research work carried out under my supervision in the Department of Civil Engineering, Indian Institute of Technology Guwahati, India and this work has not been submitted elsewhere for a degree.

Dr. Arup Kumar Sarma
Professor
Department of Civil Engineering
Indian Institute of Technology Guwahati
Guwahati - 781039

ACKNOWLEDGMENT

I would like to express my deepest sense of gratitude and heartfelt thanks to my supervisor, Prof. Arup Kumar Sarma, for his invaluable guidance, constant encouragement, and unwavering support throughout the course of my Ph.D. study. His patience, profound knowledge, and inspiring motivation have been instrumental in shaping my research and in the successful completion of this thesis. I am truly grateful for his generous nature and the precious time he devoted to guiding me at every stage of my work. It has been a great privilege and honour to work under his supervision, and I could not have asked for a better mentor and advisor for my Ph.D. research.

I extend my sincere gratitude to the members of my Doctoral Committee, Prof. Sudip Talukdar, Prof. Ajay Kalamdhad, Prof. Uday Shanker Dixit and Prof. Bimlesh Kumar for their valuable insights, constructive comments, and thoughtful suggestions which immensely enriched the quality and depth of my research. I am thankful to the Director of the Institute and the Head of the Department of Civil Engineering, IIT Guwahati, for providing me with the necessary facilities and a favourable research environment.

I wish to express my heartfelt appreciation to the then Executive Engineers of the Public Health Engineering Department, Government of Assam, Er. Bhagaban Uzir, Er. Gayatri Bhattacharyya, Er. Paragmoni Bora, Er. Ramjan Ali Khandakar, and Er. Gagan Talukder and to the Director, NERIWALM, Dr. Pradip Kumar Bora, for their kind cooperation and continuous support, which greatly facilitated my journey as a part-time research scholar.

I am deeply grateful to my fellow researchers Dr. Dipshikha Devi, Dr. Anupal Baruah, Dr. Gilbert Hinge, Dr. Santanu Pathak, Dr. Supratim Kaushik, Mr. Anurag Handique, and Ms. Bhaswatee Baishya, Mrs. Shakti Kalyani for their constant encouragement, insightful discussions, and invaluable companionship throughout the Ph.D. journey. I am also thankful to Tina, Arif, Raktim, Dipshikha, Kukil and Jusmita for their assistance during data collection and various administrative work, and to Mr. Ankur Saikia and Mr. Arif Rezza for their kind help with various software related works.

I owe my deepest gratitude to my family and friends for their unfailing support, love, and motivation throughout this long and challenging journey. Above all, I extend my heartfelt thanks to my wife, Mrs. Richma Devi, for her constant encouragement, understanding, and moral support, which gave me strength to persevere through many difficult times.

Finally, I bow in gratitude to the Almighty God for His abundant blessings, grace, and guidance, without which this endeavour would not have been possible.

[TAPASRANJAN DAS]

Abstract

Land or soil degradation is one of the most serious environmental challenges faced by the world today. It represents a reduction in the productive capacity and potential of land. In the Indian context, the magnitude of land degradation is particularly alarming. As per the Desertification and Land Degradation Atlas of India (2018-19) prepared by the Indian Space Research Organisation (ISRO), about 29.77% of the total geographical area of the country are undergoing land degradation. Among the various causes of land degradation water erosion emerges as the most dominant, affecting approximately 11.01% of the total geographic area. The Revised Universal Soil Loss Equation (RUSLE) is a widely applied empirical model for estimating soil loss due to inter-rill and rill erosion. It quantifies average annual soil loss as the product of five factors: rainfall erosivity (R), soil erodibility (K), slope length and steepness (LS), cover management (C), and conservation practice (P). Among these, the rainfall erosivity factor (R factor) represents the potential of rainfall to cause soil erosion. The R factor is defined as the mean annual value of the product of rainfall kinetic energy (E) and the maximum 30-minute intensity (I30) of individual erosive events. Thus, high temporal resolution rainfall data (≤30 minutes) are essential for accurate estimation of R factor. However, such datasets are scarce in developing countries like India.

In such circumstances, satellite-based rainfall datasets offer a valuable alternative. The Integrated Multi-satellitE Retrievals for GPM (IMERG) product provides global half-hourly rainfall data at fine spatial resolution of 0.1°. It enables the assessment of rainfall erosivity over data scarce regions. The present study utilizes the IMERG precipitation data (2001-2020) to compute the R factor over India to generate a high-resolution R factor map and to analyse the spatiotemporal variability. The spatial distribution of the R factor revealed large variability across various regions. The national average R factor is 2188.79 MJ.mm/ha.h.yr and ranges from 68.28 in the cold-arid regions of Himachal Pradesh to 18,864.2 in Assam. The erosivity hotspots were predominantly found in the North East India and the Western Ghats. The monthly and seasonal analyses discovered that the Southwest Monsoon (June-September) contributed the most to annual erosivity, while the

winter months carries minimal values. Long-term trend analysis (2001-2020) indicated high inter-annual variability but no consistent nationwide trend, with significant positive trends (1.82%) mainly in Rajasthan and parts of North East India.

Traditionally, the R factor has been expressed as an annual mean, and the corresponding soil loss estimated from it reflects the average annual soil loss. However, using the mean value for design purposes can be misleading in regions with high inter-annual rainfall variability. It may underestimate soil loss during extreme rainfall years and overestimate it during dry years. To overcome this limitation, the current study introduces return period-based analysis of rainfall erosivity, which accounts for variability in erosive events across different recurrence intervals. This probabilistic approach provides a more reliable basis for designing soil conservation structures. The R factor corresponding to 2, 5, 10, 25, 50 and 100 year return periods was estimated using IMERG half hourly data. It was observed that nearly 95% of the annual R factor values fell within the 2 to 5 year return period range. The majority of the cases relating to the maximum annual R factor correspond to a return period range of 25 to 50 years. The study demonstrated that dependence on mean annual R factor alone may underestimate soil loss potential. Thus, this return period-based approach provides a more realistic and robust framework for erosion control planning and infrastructure design.

The study also recognizes that while satellite-based rainfall data provide very good coverage in space and time, they can sometimes have errors or biases in certain regions. IMERG data tends to overestimate rainfall in high altitude mountainous region. To improve its accuracy, this research performs a calibration of IMERG (Late) data using the India Meteorological Department (IMD) daily gridded rainfall dataset. The study used the modified Daily Spatio-Temporal Disaggregation Calibration Algorithm (DSTDCA) for this purpose. This calibration merges the temporal distribution of IMERG with the IMD daily rainfall, resulting in a new dataset, which can be termed IMDMERG. The calibrated dataset was then used to regenerate erosivity maps for India. The IMERG (Final) dataset exhibited an overestimation bias of approximately 7% in annual rainfall relative to IMD daily gridded data. After calibration through the modified DSTDCA, the IMDMERG dataset successfully preserved daily rainfall totals with ground observations while retaining sub-daily distribution of IMERG. The R factor maps derived from IMDMERG identified new erosivity hotspots in the Western Ghats, Northeast India, and parts of the Eastern Ghats.

The research also explores the impact of climate change on rainfall erosivity. It focuses on how altered precipitation patterns could intensify soil erosion. The Intergovernmental Panel on Climate Change (IPCC) highlighted that increasing extreme rainfall events due to global warming could significantly enhance rainfall erosivity and accelerating land degradation. The study assesses future erosivity patterns of rainfall erosivity in the Pamohi watershed of Assam using climate projections from CMIP6 models under two Shared Socioeconomic Pathways (SSP245 and SSP585). However, since Global Climate Models provide rainfall data only at daily temporal resolution, two approaches were adopted: (i) developing a Multiple Linear Regression (MLR) model to estimate R factor directly from daily rainfall data and (ii) disaggregating daily rainfall into sub-daily intervals to compute R factor through the standard RUSLE method. The newly developed MLR model significantly outperformed existing widely used empirical models, showing a very low percentage error of 2.86 %. The historical R factor estimated by both the approaches was found to be similar to the R factor computed by observed half hourly dataset. The findings of this study were compared with climate change analyses conducted at global, national, and regional scales, and a strong consistency was observed with the results obtained from the rainfall disaggregation approach. However, the increasing trend in rainfall erosivity was also maintained in the MLR based empirical model. Comparative evaluation of both methods suggested that while the MLR approach is computationally efficient and suitable for large-scale applications, it tends to smooth local extremes and underestimate peak erosivity. The disaggregation method, though more data-intensive, better captured rainfall intensity dynamics.

This research advances the understanding of rainfall erosivity over India by integrating high-resolution satellite rainfall data, ground-based calibration, return period analysis, and climate change assessment. The outcomes of this study are expected to serve as a scientific basis for policymakers and environmental planners in developing sustainable soil conservation and erosion mitigation strategies.

Keywords: RUSLE, Rainfall Erosivity Factor, IMERG, Return Period, Climate Change

Table of Contents

List of Figures

List of Tables

List of Symbols

Symbols	Description
R	Rainfall Erosivity Factor
K	Soil Erodibility Factor
LS	Slope and Steepness Factor
C	Cover Management Factor
P	Conservation Practice Factor
E	Kinetic Energy of a Rainfall Event
I30 or I_{30}	Maximum 30 minute intensity of a Rainfall Event
EI_{30} or EI30	Multiplication of E and I30
S	Mann-Kendall test statistic
Z	Standardized Mann Kendall statistic
Φ	Laplace Integral
Γ	Gamma Function
R^2	Coefficient of Determination
i	Rainfall Intensity
v_r	Rainfall depth
ε	Random error term of Multiple Linear Regression
P_c	Pearson correlation coefficient

List of Abbreviations

Terms	Abbreviations
ISRO	Indian Space Research Organisation
RUSLE	Revised Universal Soil Loss Equation
IMERG	Integrated Multi-satellitE Retrievals for GPM
GPM	Global Precipitation Measurement
IMD	India Meteorological Department
DSTDCA	Daily Spatio Temporal Disaggregation Calibration Algorithm
IPCC	Intergovernmental Panel on Climate Change
CMIP	Coupled Model Intercomparison Project
SSP	Shared Socioeconomic Pathways
MLR	Multiple Linear Regression
GPCC	Global Precipitation Climatology Centre
GCM	Global Climate Model
USLE	Universal Soil Loss Equation
MFI	Modified Fournier Index
PCI	Precipitation Concentration Index
PERSIANN	Precipitation Estimation from Remotely Sensed Information using Artificial Neural Networks
IR	Infrared
CMORPH	Climate Prediction Center (CPC) MORPHing
PMW	Passive Microwave
TRMM	Tropical Rainfall Measurement Mission
TMPA	TRMM Multisatellite Precipitation Analysis
JWD	Joss Waldvogel Disdrometer
GSMaP	Global Satellite Mapping of Precipitation
CART	Classification And Regression Tree
GPCP	Global Precipitation Climatology Project
SG	Satellite Gauge
PDF	Probability Density Function
OI	Optimal Interpolation

APHRODITE	Asian Precipitation – High-Resolved Observational Data Integration Towards Evaluation
NOAA	National Oceanic Atmospheric Administration
RCP	Representative Concentration Pathway
GPR	Gaussian Process Regression
UCRW	Upper Charles River Watershed
IDF	Intensity Duration Frequency
NASA	National Aeronautics and Space Administration
NITI	National Institution for Transforming India
CDF	Cumulative Distribution Function
EDF	Empirical Distribution Function
KS	Kolmogorov-Smirnov test
IDW	Inverse Distance Weighted interpolation
UTC	Coordinated Universal Time or Universal Time Coordinated
IST	Indian Standard Time
NSE	Nash-Suttcliffe efficiency
RMSE	Root Mean Square Error
P.E	Percentage Error
MAE	Mean Absolute Error
PBIAS	Percent Bias
VIF	Variance Inflation Factor
SE	Standard Error
CI	Confidence Interval
PSO	Particle Swarm Optimization
IMDAA	Indian Monsoon Data Assimilation and Analysis

Chapter 1

Introduction

1.1 General

Land or soil degradation is one of the most serious issues of the present time. Land degradation, in general, may refer as the reduction in the productive capacity and productive potential of the soil (Stocking 2001). Soil degradation may also be referred as physical, chemical and biological decline of soil quality. The topsoil constitutes almost all the nutrients required for agriculture. A healthy soil is also crucial for carbon sequestration as it can store more carbon in comparison to living plant and atmosphere. Degraded land reduces the percolating capacity and water storage ability of the soil mass hence affects the productivity (Gobinath et al., 2022). According to a study performed by United Nation, nearly one-third of the world's arable land has vanished in the past forty years. If the present loss rates continue, the world's topsoil might all become unusable within 60 years (Maximillian et al., 2019).

As per Desertification and Land degradation atlas of India prepared in the year 2018-19 by Indian Space Research Organisation (ISRO), 97.85 Million Ha, 29.77% of the Total Geographical Area of the country is undergoing Land Degradation. India holds the second position of most populated country in the world and first in terms of livestock population. India is also the second largest producer of food and agriculture (ISRO, 2021). Thus, the land mass of India experiences tremendous pressure and in turn raises the possibility of Land degradation in the country. Land degradation triggers various problems, which are partly irreversible and causes multiple social or economic issues. Various causes of Land Degradation are water erosion, wind erosion, vegetation degradation, salinity, water logging, anthropogenic etc. The most significant process of Land Degradation of the country is water erosion. Approximately 36.20 Million Ha, 11.01 % of Total Geographic Area is undergoing Land Degradation due to Water Erosion (ISRO, 2021).

Loss or detachment of the topsoil is the primary result of water erosion, and the soil loss again leads to various other environmental problems (Issaka and Ashraf, 2017; McCool and Williams, 2008). The quantity of soil loss can be estimated by a widely used method called Revised Universal Soil Loss Equation (RUSLE). It is basically used for computing soil loss due to inter-rill and rill erosion. In this method the annual average soil loss of an area is estimated by multiplying five factors, viz. rainfall erosivity factor (R), soil erodibility factor (K), slope length and steepness factor (LS), cover management factor (C) and conservation practice (P) factor (Renard *et al.* 1997; Wischmeier & Smith 1978). The term used to describe the capacity of rainfall to induce soil erosion is called the rainfall erosivity. The erosivity of rainfall is a vital factor that significantly fluctuates and contributes to soil erosion, especially concerning the effects of changing climate. The rise in the number of intense and short-duration rainfall events leads to a corresponding increase in events characterized by elevated erosive power (Gonzalez-Hidalgo et al., 2012). The Rainfall erosivity factor, popularly known as the R factor of RUSLE, is widely recognised as a measure of expressing the erosive potential of rainfall. The R factor denotes the annual mean of EI_{30} of each erosive rainfall event, where E represents the rainfall kinetic energy expressed in terms of intensity and rainfall depth, and I_{30} is the maximum 30-minute intensity of a rainfall event (Renard et al., 1997).

Very high temporal resolution (≤ 30 min) rainfall data is required to calculate the long-term average R factor (Renard et al., 1997). But in most part of the world such high temporal resolution gauge data rainfall is very scarce. Though it can be found in some IMD stations in India, but it is difficult to find in digitised form which has made the rainfall erosivity study a tough job in India. The modern age satellite rainfall data has enough potential to contribute to the rainfall erosivity study of data scarce region. A popular high spatiotemporal resolution satellite precipitation product of recent time called IMERG (Integrated Multi-satellitE Retrievals for GPM (Global Precipitation Measurement)) has been widely used in many hydrologic studies globally and in India also. In the present study, IMERG rainfall data have been utilized to estimate the Rainfall Erosivity Factor, with the aim of examining the suitability of satellite-based precipitation products for erosivity assessment.

Traditionally, the R factor denotes the mean annual value; consequently the soil loss evaluated based on this corresponds to the average annual soil loss (Wischmeier and Smith 1978). However, there are some drawbacks to using the average annual soil loss. While designing soil conservation structures, relying on average soil loss is appropriate only if the annual soil loss data series follows a normal distribution and shows low variability over the year. Utilizing average soil loss in regions characterized by significant annual rainfall variability leads to overestimation of soil loss during dry years and underestimation during wet years (Mannaerts and Gabriels, 2000; Pampalone and Ferro, 2020). Taking the average annual value in designing soil conservation structures can sometimes be unreliable and unsafe. Moreover, understanding soil erosion processes in future scenarios holds significant importance for managers and decision-makers. However, accurately forecasting rainfall erosivity and subsequent soil erosion proves challenging because of inherent uncertainties associated with rainfall storms, which exhibit day-to-day variations in a seemingly random and unpredictable manner (Sadeghi and Hazbavi, 2015). In many regions of India, deforestation is widely happening due to shifting cultivation, natural calamities, anthropogenic pressure and developmental activities. The resulting deforested regions are most likely to be eroded by the action of water erosion. The effects of water-causing erosion are not limited to only soil fertility loss. It is also creating various other environmental issues such as waterlogging, silting of drains, flash floods and decrease in groundwater. To control soil erosion, it is commonly recommended to implement soil conservation measures, construct silt traps, and carry out extensive afforestation programs. However, due to the consideration of average soil loss estimation in designing such structure, often causes failure.

To overcome this problem, probabilistic and statistical approach, such as frequency distribution analysis with the help of historical data can offer valuable insights by estimating variable magnitudes associated with different return periods (Mannaerts and Gabriels, 2000). The return period refers to the interval between the recurrence of an event of certain magnitude expressed in year.

Generally, such studies used rain gauge data and estimation in transition areas are spatially interpolated from the nearest points. Due to the application of interpolation methods, there is a strong probability that a significant level of uncertainty will be observed in the rainfall erosivity values of transition areas. Moreover, such stations are not uniformly distributed, which leads to erroneous results in areas with limited number of stations or no stations. However, one of the key advantages of satellite-based precipitation products lies in their ability to effectively capture the spatial variability of rainfall, particularly in regions that are sparsely or poorly gauged. This makes them a valuable resource for large-scale hydrological and climatological studies. Thus, this study also explores the use of satellite-based precipitation products in conducting return period analysis of R factor.

However, despite their many benefits, satellite-based rainfall datasets also have some limitations. Satellite-derived precipitation estimates, such as those from IMERG, inherently carry uncertainties that vary across regions. Notably, IMERG has been found to overestimate daily and hourly rainfall in high-altitude areas (Xu et al., 2019). This is primarily because satellites estimate precipitation indirectly, relying on remote sensing algorithms that are susceptible to various sources of error. Accordingly, calibration with ground-based observations becomes essential to enhance the accuracy and reliability of satellite precipitation datasets (Huffman et al., 2019). The IMERG product is calibrated globally on a monthly scale using the GPCC (Global Precipitation Climatology Centre) dataset at a 1°/ monthly resolution. As a result, IMERG performs well when analysed at monthly timescales, but its accuracy deteriorates when applied to finer temporal resolutions (Ma et al., 2020). To address this issue, the present study undertakes a calibration of IMERG (Late) half-hourly precipitation data using IMD daily gridded rainfall. This step is aimed at improving the performance of the IMERG dataset at the finer temporal scale required for accurate estimation of rainfall erosivity and soil loss.

In addition, this study also addresses a critical issue of the present time, the impact of climate change on rainfall erosivity. Intergovernmental Panel for Climate Change (IPCC) reported in 2019 that the climate change could exacerbate the current land degradation and soil erosion scenario due to extreme precipitation events. The intensification of rainfall will directly enhance its erosive potential and accordingly rainfall erosivity will be increased. As per RUSLE method the soil loss from an area is directly influenced by rainfall erosivity factor, provided that all other factors remain unchanged, thus it is evident that any alteration in rainfall patterns due to climate change will significantly impact soil erosion dynamics (Nearing, 2001). The interaction between shifting climatic patterns and changing land use practices can substantially accelerate global water-induced soil erosion. Projections indicate that these combined influences may lead to an estimated 30% to 60% rise in soil erosion rates (Borrelli et al., 2020; Panagos et al., 2022a). A comprehensive understanding of how climate change influences the R-factor is crucial for devising improved land resource management strategies.

However, the future precipitation data from GCMs (Global Climate Model) are provided on a daily scale, whereas the standard RUSLE methodology necessitates sub-daily rainfall data for accurate computation of the R factor (Renard et al., 1997). To address this challenge, two potential approaches are available. The first approach is to formulate an equation that enables the assessment of the R Factor directly from daily rainfall data. The second approach entails disaggregating daily rainfall into sub-daily intervals, enabling the direct application of the standard method for R Factor estimation. Rainfall disaggregation models are basically employed to derive sub-daily rainfall time series from daily data. Generally, the first approach is more commonly used. Thus, in this research work an effort has been undertaken to disaggregate the daily rainfall to sub-daily rainfall and rainfall erosivity factor is calculated by standard method. To further enhance understanding, an empirical relationship is also developed to estimate rainfall erosivity from daily rainfall. Researchers and stakeholders often use empirical formulas derived in other regions. While convenient, this practice can lead to significant errors. Therefore, development of a region-specific empirical equation for the R factor is needed to improve the reliability of rainfall erosivity estimates and enhance the effectiveness of soil conservation planning. This allows a comparative analysis between the two methods. This dual approach enables a thorough evaluation of future erosivity under climate change and helps in comparing it with existing studies to assess the reliability of projections.

1.2 Broad Objectives of the study

The primary goal of this study is to analyze the rainfall erosivity of India and the effect of climate change on rainfall erosivity. The objectives of this study are as follows:

1. To prepare the rainfall erosivity map of India using IMERG 0.1° half hourly rainfall data and perform analysis of spatiotemporal variation.
2. To perform return period analysis for annual rainfall erosivity factor of India.
3. To calibrate the IMERG half hourly data using IMD daily gridded data to generate 0.25 degree half hourly precipitation dataset.
4. To study the effect of climate change on rainfall erosivity factor.

1.3 Organisation of the Thesis

In addition to the basic introduction and the broad objectives of this research, a synoptic view of the organisation of rest of the chapters of the thesis are presented in Chapter-1.

Chapter-2 gives a systematic and detailed review of the previous works on the research area to have up-to-date knowledge on various themes relevant to this study. This is followed by a critical assessment of the literature stating the necessity for further research. Finally, the scope of present work is stated clearly mentioning the goal of the research.

Chapter - 3 focuses on the spatiotemporal analysis of rainfall erosivity across India. A rainfall erosivity (R factor) map of India is generated using satellite precipitation data. The outputs are validated and compared with ground-based rainfall erosivity maps as well as data derived from a single rain gauge station. Sensitivity analysis is also performed to assess the influence of input variables on the computed R factor.

Chapter - 4 incorporates the return period analysis into the assessment of rainfall erosivity. Suitable theoretical probability distributions are fitted to annual R factor values to determine the best-fitting model. The R factor corresponding to different return periods is computed, and trend analysis is conducted to understand temporal variations in annual erosivity.

Chapter - 5 addresses the calibration of IMERG satellite precipitation data using IMD daily gridded rainfall data. This chapter outlines the calibration procedure and application in generating Rainfall Erosivity Map of India.

Chapter - 6 investigates the impact of climate change on rainfall erosivity in India. Two distinct methodologies are employed viz. rainfall disaggregation and the development of an empirical equation, to estimate future changes in rainfall erosivity under different climate scenarios. The spatial and temporal patterns of projected changes are thoroughly analyzed.

Finally, Chapter - 7 gives a summary and conclusion of the research work performed. The limitations and future scopes of the research will also be described here.

Chapter 2

Literature Review

2.1 Introduction

As per Desertification and Land degradation atlas of India prepared in the year 2018-19 by Indian Space Research Organisation (ISRO), 97.85 Million Ha, 29.77% of the Total Geographical Area of the country is undergoing Land Degradation (ISRO, 2021). The most significant process of Land Degradation of the country is water erosion. Approximately 36.20 Million Ha, 11.01 % of Total Geographic Area is undergoing Land Degradation due to Water Erosion (ISRO, 2021). The erosive power of rainfall often termed as Rainfall Erosivity (Lal, 2001) is among the prime driver of water erosion in an area. The rainfall erosivity factor has its origin in the term, "Potential Erosivity", one of the three terms to define the process of soil erosion due to water, proposed by Cook (1937). The term Potential Erosivity is the capacity of rainfall and runoff to initiate soil erosion from a standard area. The modern rainfall erosivity factor was first proposed by Wischmeier and Smith (1958) Wischmeier (1959) in the handbook of Universal Soil Loss Equation. The rainfall erosivity factor is one of the five factors used for computing the soil loss of an area. They defined the rainfall erosivity factor for each erosive rainfall event, is defined as the mean annual summation of a term EI_{30} of each erosive rainfall event, where E is the kinetic energy and I_{30} is the maximum 30 minute intensity. Renard et al. (1997) introduced the Revised Universal Soil Loss Equation (RUSLE), building upon earlier formulations. While they retained the original approach for estimating rainfall erosivity, they changed the equation for calculation of the kinetic energy of erosive rainfall events. The most recent version, RUSLE2 (USDA-Agricultural Research Service, 2013), updated the equation for kinetic energy by slightly changing a coefficient. Despite the release of the updated RUSLE2, the original RUSLE continues to be widely used in studies across the globe. In the present study as well, the RUSLE formulation has been adopted.

The literature reviewed in this chapter will broadly encompass the following thematic areas:

1. Rainfall Erosivity studies in India
2. Sub-Daily Precipitation products and its application in Rainfall Erosivity studies
3. Return period analysis and its application in Rainfall Erosivity studies

4. Calibration of satellite-based rainfall dataset
5. Climate change studies on Rainfall Erosivity
6. Application of Empirical equation on Rainfall Erosivity studies
7. Method of Rainfall Disaggregation and its application in various field including Rainfall Erosivity analysis

2.2 Rainfall Erosivity Studies in India

The quantification and spatial representation of rainfall erosivity have been of considerable interest to hydrologists and soil conservationists in India since the late 1970s. The first national-level rainfall erosivity factor map was developed by Babu et al. (1978), marking a pioneering effort to provide a spatially distributed assessment of erosivity for the entire country. This study utilized rainfall data from 44 rain gauge stations. They applied interpolation techniques to prepare the R factor map of India. The study is limited in terms of number of stations. However, it provided a crucial baseline for subsequent erosivity assessments in the country. In the similar line, Das and Babu (1979) proposed a systematic procedure for calculating rainfall erosion indices (EI) in metric units. This work was an important step towards standardization in the Indian context. Their methodology enabled direct computation of EI values. It also provided a framework for converting existing EI data into the metric system. They also explored the feasibility of estimating rainfall energy and erosivity indices using the product of total rainfall and maximum rainfall intensity. They proposed a relatively simple way to compute R factor where high temporal resolution data is not available. During the late 1980s, some advancements were happened in computerized data management which helped more structured erosivity assessments. Karale et al. (1989) developed a software module called ‘WEIGHT’, which is designed to compute erosivity values for mapping units. These mapping units are related to combinations of climate, physiography, slope, land use and cover, soil properties, and the influence of erosion control measures.

Hadda et al. (1991) provided more understanding by linking daily rainfall and erosivity through deterministic and random components. Their analysis showed that the deterministic relationship was best captured by a power-law function. This alone explained the erosivity-rainfall relationship with a strong correlation coefficient of 0.87. In the subsequent decade, refinement of national scale erosivity mapping continued. Babu et al. (2004) prepared a more detailed R-factor map of India. They incorporated data from 123 recording type rain gauge stations. They also extended their analysis to 500 non-recording stations by applying empirical relationships between annual/seasonal mean rainfall and EI values. This allowed them to use a total of 623 stations, which significantly improves the spatial resolution and reliability of erosivity estimates as compared to their earlier work. At the station scale, Sharda and Ojasvi (2006) developed a rainfall erosivity computation model based on daily rainfall data from Dehradun. They found that a logarithmic functional form best described the relationship between rainfall and erosivity. Their work provided a practical approach for local scale erosivity estimation. Similarly, Nandgude et al. (2013) conducted a study in the Wakavali region of Maharashtra using self-recording rain gauge data. They observed that rainfall depth contributed more considerably to total kinetic energy than rainfall intensity.

An important contribution at the national scale was made by Tiwari et al. (2016). They used 101 years of monthly rainfall data from 52 spatial points across India. They prepared a rainfall erosivity factor map using the Modified Fournier Index (MFI), which revealed strong spatial variability. The North-Eastern region shows the highest erosivity values and Northern and North-Western regions having the lowest. This study provided long-term understanding into the spatial distribution of erosivity in India. Some more improvement of erosivity estimation methods was attempted by Dash et al. (2018). They compared six different kinetic energy and intensity relationships for the Eastern Ghat region of India. Their analysis indicated that different equations produced divergent results under low rainfall intensity conditions and similar result under high intensity. As per their study the equation proposed by Brown and Foster (1987) and recommended in the RUSLE handbook, gives the best results. However, they mentioned that this equation required high temporal resolution rainfall data, which is often scarce in India and due to this limitation, Dash et al. (2019) proposed regression equations for estimating R factor values using readily available daily, monthly, and annual rainfall data.

In the recent time, Singh and Singh (2020a, 2020b) carried out two detailed studies in the Suketi River catchment of the Himachal Himalayas. This research together provided an in-depth perspective of rainfall erosivity, erosivity density, and rainfall seasonality during 1971–2015. The first study assessed erosivity and erosivity density using daily rainfall records from three sparsely distributed stations. They observed that more than 90% of total erosivity occurred during summer and monsoon seasons. The findings underscore the seasonal concentration of erosive rainfall and its probable effects on soil erosion in mountainous catchments. The second study focused on rainfall seasonality, distribution, and erosivity using non-parametric indices such as the Seasonality Index (SI), Precipitation Concentration Index (PCI), and Modified Fournier Index (MFI). Their findings revealed pronounced fluctuations over time and strong spatial heterogeneity of rainfall erosivity and seasonality.

Overall, the literature demonstrates a progressive evolution in rainfall erosivity research in India. The studies started from early national-scale interpolations using limited rain gauge data to sophisticated approaches integrating statistical models, empirical relationships, and long-term climatic indices. These studies not only emphasize the methodological advancements but also underscore the challenges caused by data scarcity. The studies also pointed out the need for high temporal resolution observations and the complex spatial variability of rainfall erosivity over India.

2.3 Sub-Daily Satellite Precipitation Product

The accurate estimation of precipitation at fine temporal and spatial scales is important for hydrological studies, climate monitoring and water resource management. The rain gauge measurements offer high accuracy, but they are often sparsely distributed, particularly in remote, mountainous, or developing regions. This makes it tough to study large-scale hydrological and climatological analyses. To overcome this limitation, satellite-based precipitation estimation systems have been developed, offering near-global coverage and the capability to supplement or replace ground observations.

The PERSIANN (Precipitation Estimation from Remotely Sensed Information using Artificial Neural Networks) is one of the first important dataset developed at the University of Arizona (Hsu et al., 1997). PERSIANN uses an adaptive Artificial Neural Network (ANN) framework to estimate rainfall rates using infrared (IR) satellite imagery in combination with ground-surface information. A distinct feature of PERSIANN is its adaptive recursive updating mechanism. Due to this mechanism the ANN parameters are continuously updated whenever ground-based observations are available. This adaptive capability enables the system to respond effectively to regional and seasonal variations in precipitation patterns.

The Climate Prediction Center Morphing technique (CMORPH) represents another significant advancement in satellite-based precipitation estimation. CMORPH combines high-quality precipitation estimates derived from passive microwave (PMW) sensors with motion information extracted from geostationary IR imagery. The PMW derived estimates are propagated forward and backward in time using motion vectors. The time-weighted linear interpolation is employed to maintain temporal continuity between PMW overpasses. This approach ensures both spatial and temporal completeness and remains independent of the IR temperature field. The spatial and temporal resolution of CMORPH is 8 km and half-hourly respectively and the dataset is available from November 2002 to till date (Joyce et al., 2004).

The Tropical Rainfall Measuring Mission (TRMM) Multisatellite Precipitation Analysis (TMPA) further advanced satellite-based rainfall estimation. TMPA utilizes a calibration-based sequential scheme to merge precipitation data from multiple satellites and incorporates gauge analyses wherever feasible. This methodology enables the generation of precipitation estimates at relatively fine spatial (0.25° × 0.25°) and temporal (3 hourly) resolutions. TMPA data are available both in real time and after real time. The after real time integrated with gauge observations. TMPA covers the latitude band between 50°N and 50°S and is available from 1998 to 2015 (Huffman et al., 2007).

The Integrated Multi-satelliE Retrievals for GPM (IMERG) represents the latest advancement in sub-daily, global satellite precipitation products. It is developed under the Global Precipitation Measurement (GPM) mission and serves as the successor to TRMM TMPA. It provides global precipitation estimates at 0.1° × 0.1° spatial resolution and half-hourly temporal resolution. IMERG integrates PMW observations from the GPM constellation with IR satellite data, reanalysis fields, and gauge measurements to produce high quality precipitation product. (Huffman et al., 2019). IMERG is a very useful tool for present water and climate studies because it gives more detailed data over time and space and combines information from many sources.

Collectively, these sub-daily satellite precipitation products have greatly improved the ability to monitor and analyse rainfall at regional to global scales. This has helped in better flood forecasting, water resource management and climate impact assessments. In the present study, the IMERG satellite precipitation product has been employed.

2.3.1 Use of IMERG Satellite Precipitation Product in India

The Integrated Multi-satellitE Retrievals for GPM (IMERG) dataset has emerged as one of the most reliable satellite-based precipitation products over India. As compared to other satellite rainfall products, IMERG shows better accuracy and reliability across various temporal and spatial scales (Reddy et al., 2019; Singh et al., 2019). Its high spatiotemporal resolution offers strong potential to improve rainfall monitoring over the Indian subcontinent (Prakash et al., 2016).

Murali Krishna et al. (2017) conducted an evaluation of IMERG rainfall estimates by comparing them with ground-based rain gauge measurements, the Tropical Rainfall Measuring Mission (TRMM) 3B42 product and Joss-Waldvogel Disdrometer (JWD) observations. Their study includes sub-daily, diurnal, monthly, and seasonal periods. The results validated IMERG as a reliable tool for rainfall estimation in India and highlighted its significant improvements over older products such as TRMM. However, the study also noted limitations of IMERG in regions with complex terrain or very high precipitation. Prakash et al. (2018) further evaluated high-resolution satellite rainfall products over India with a focus on the southwest monsoon season. Their analysis revealed that IMERG generally outperforms other satellite datasets such as Global Satellite Mapping of Precipitation (GSMaP) and TMPA in capturing medium to heavy rainfall events. The GSMaP exhibited lower errors in low rainfall areas and it slightly underestimated large scale monsoon features The TMPA was found to be less accurate overall, especially in low to moderate rainfall regions. This study also noted that all satellite products challenges in mountainous regions and rain-shadow areas.

Several studies have also got similar findings and collectively indicate that IMERG is a reliable, high resolution satellite rainfall product that effectively captures medium to heavy precipitation and aligns well with Indian Meteorological Department (IMD) observations (Bushair et al., 2019; Mahmoud et al., 2021; Mukhopadhyay et al., 2019; Singh et al., 2018; Thakur et al., 2020b; Verma and Ghosh, 2018). However, IMERG tends to underestimate extreme rainfall events, thus there is a need for further refinements to enhance its operational utility during severe weather scenarios. The utility of IMERG in extreme rainfall and hazard assessment has also been investigated. Thakur et al. (2020a) analysed its role in triggering landslides in the Western Ghats. They found substantial rain rates exceeding 60 mm/h in half-hourly data. The study concluded that IMERG is a reliable tool for monitoring heavy rainfall events with possibility to trigger landslides. In addition to performance evaluations, several studies have explored methods to improve the accuracy of IMERG rainfall estimates by correcting errors and biases. Bhuiyan et al. (2020) utilized machine learning-based stochastic error correction over the Brahmaputra river basin, while Chaudhary and Dhanya (2020) applied CART-based bias correction techniques across India. Overall, the literature indicates that IMERG represents a substantial advancement in satellite precipitation estimation over India.

2.3.2 Use of Satellite Precipitation Product in Rainfall Erosivity Study

Accurate estimation and spatial mapping of rainfall erosivity are fundamental for effective soil conservation planning. However, achieving this remains a major challenge in regions where ground-based rainfall observations are limited. The emergence of satellite-based precipitation products, such as the TRMM, IMERG, CMORPH etc., has significantly enhanced the capability to assess rainfall erosivity from regional to global scales with improved temporal and spatial resolution.

Vrieling et al. (2014, 2010) evaluated rainfall erosivity across Africa using 3 hourly TRMM Multi-satellite Precipitation Analysis (TMPA) data. The study reported a moderate correlation (r = 0.71) between TRMM-derived erosivity estimates and station-based measurements. Similarly, Zhu et al. (2011) developed a novel method for estimating rainfall erosivity in the Daling River Basin, China, by combining TRMM 3B42 data with the maximum 180 minute rainfall intensity and rainfall energy. Their TRMM-derived erosivity values presented strong agreement with interpolated rain gauge data. In another study, Fan et al. (2013) utilized TRMM 3B42 data to estimate rainfall erosivity across the Tibetan Plateau for the period 2000 to 2010. They validated their result with station data and the spatial patterns of erosivity were found to align closely with rainfall distribution.

In India, Dutta et al. (2015) used TRMM data to estimate the rainfall erosivity factor (R) for the Sanjal watershed in Jharkhand adapting the RUSLE guidelines. Although the study took the advantage of high temporal resolution satellite derived rainfall estimates, it relied on an empirical annual rainfall based relationship to compute R factor. Li et al. (2020) further explored the influence of temporal resolution on R factor estimation in the Poyang Lake Basin, China, using multiple TRMM products. Their analysis showed that the 3 hourly TRMM 3B42 product underestimated monthly erosivity.

Chen et al. (2021) compared the IMERG Final run and TMPA 3B42-V7 products with gauge-based rainfall data from 2,417 stations across China. Both datasets exhibited strong spatial correlations with observed values (r = 0.944 for IMERG Final run and r = 0.909 for TMPA), with IMERG Final run demonstrating superior performance and broader applicability across diverse climatic regions and timescales. Despite the availability of

30-minute temporal resolution data of IMERG Final run, the study utilized daily data and applied the daily rainfall erosivity model proposed by Xie et al. (2016) for computing R factor.

In addition to TRMM and IMERG, several other satellite-based precipitation products have also been utilized in rainfall erosivity studies. At the continental scale, Kim et al. (2020) employed CMORPH satellite data to map rainfall erosivity across the contiguous United States, the first such effort using half-hourly satellite precipitation estimates and the erosivity factor (R) was computed following the standard methodology of the RUSLE handbook. The results revealed high spatial variability of erosivity and tropical and coastal regions showing the greatest erosivity magnitudes. However, corrections were required in coastal zones where CMORPH underestimated rainfall erosivity relative to rain gauge assessments.

To further improve satellite based erosivity estimates, Teng et al. (2017) proposed a data-merging approach that combined TRMM 3B42 data with observed rainfall measurements using collocated cokriging (ColCOK). This method produced more accurate rainfall and erosivity distributions compared to TRMM alone or block kriging. Similarly, Fenta et al. (2017) utilized multisource rainfall datasets such as CHIRPS to assess rainfall erosivity across Eastern Africa.

Overall, these studies demonstrate that satellite precipitation products such as TRMM, IMERG and CMORPH have become indispensable tools for assessing rainfall erosivity, specifically in regions with limited ground observations. Since these products captures the spatial and temporal dynamics of rainfall at fine resolution, they enable more robust and comprehensive evaluations of erosivity.

2.4 Return Period Analysis

The concept of return period was first introduced by Fuller (1914) and it has a legacy of more than a century and continues to hold significant importance in hydrology as well as other branches of geoscience (Volpi et al., 2015). Despite its long history, the concept remains highly relevant and is widely used in many recent studies. For example, Alam et al. (2018) conducted a research on finding the best-fit probability distributions and return periods for maximum monthly rainfall in Bangladesh. They presented the return levels corresponding to 10 year, 25 year, 50 year and 100 year return period. Perez et al. (2021) studied the rainfall time series with application to calculation of return periods. They established benchmark precipitation values and derived more reliable return period estimates, even in situations where long-term historical rainfall records were not available. The statistical analysis produces return period curves, showing how often extreme rainfall of different intensities is likely to occur. The concept of return period is most widely used in flood frequency analysis, helping to understand how often extreme floods are likely to occur. Some of the recent studies includes, a study by Kousar et al. (2020), where they found the best-fitting distribution and used that to estimate design floods (maximum flow) for 5, 10, 25, 50, 100, 200, 500, and 1000 years in the Ume River, Sweden. Mangukiya et al. (2022) performed the flood frequency analysis and inundation mapping for lower Narmada Basin, India. The main objective of the study was to project peak floods corresponding to various return periods (10, 25, 50, and 100 years) and to map the expected flood inundation under those scenarios. However, only a few studies have explored the application of the return period concept in the context of rainfall erosivity.

2.4.1 Use of Return Period in Rainfall Erosivity Study

Ferro et al. (1991) used the return period concept in Sicily, Italy and an erosion risk index was developed during the study, which is a ratio between 50 years return period R factor and the mean annual R value calculated as per Wischmeier and Smith (1978). A significant discovery from their research was that locations with comparable mean R values exhibited substantial variation in erosion risk index values. This suggests that regions with identical average annual R factor may exhibit varying R factors corresponding to a return period. Thus, as a result two area will be considered as equally erosive by rain if the mean annual R factor is same, but which may not be true all the time. In the same line, Aronica and Ferro (1997) determined the erosion risk index in Calabrian Region. They computed the R factor as per Arnoldous (1980) and found similar results. Diodato and Bellocchi (2009) analysed 138 years (1869 to 2006) rainfall data to study the variability of erosivity and erosive extremes at Benevento, South Italy. They computed correlation coefficient of seasonal contribution and annual erosivity for two return periods, 2 year and 50 years. It was found that autumn season shows the highly significant positive correlation for both the return periods. Martins et al. (2010) conducted a return period analysis of rainfall erosivity in an experimental watershed at Aracruz, Brazil, and reported that the return period of the annual average R factor was 3.4 years. Taguas et al. (2011) in southern Spain found that the annual average rainfall erosivity falls between 2 and 5 year return period value. Both the above studies show the level of underestimation of soil erosion in designing soil conservation structure when the average rainfall erosivity is used. The hypothesis proposed by Bagarello et al. (2011) states that in designing soil conservation structure, it is not enough to just consider the average soil loss. Instead, designs should account for soil loss associated with a specific return period. They found that the frequency distribution of soil loss events closely follows the frequency distribution of rainfall erosivity events. Based on this finding, they proposed that annual soil loss corresponding to a given return period can be estimated indirectly from rainfall erosivity records, using a frequency factor. Sadeghi et al. (2017) evaluated spatiotemporal variation of R factor for various return period using data from 70 rain gauge station in Iran. Return period analysis of soil erosion and sediment yield provide the stakeholders to choose best option for soil erosion control and management structure utilizing information of past events. However, the ultimate decision-making process is influenced by several factors, including project costs, objectives, and other relevant considerations (Sadeghi et al., 2017). In a recent study conducted by Zhou et al. (2023) in Three Gorges Reservoir, China, researchers found that Rainfall erosivity is the main driver of erosion on bare uplands. The study focused on identifying which types of rainfall events exert greater influence on soil erosion in different seasons. They found that in the dry season, rare but strong rainfall events (with return periods between 5 and 20 years) caused most of the soil erosion, contributing more than 65% of total erosion. In the wet season, more common rainfall events (with return periods 1–2 years) contributed almost 50% of the total erosion.

2.5 Calibration of satellite rainfall dataset

Satellite estimates are indirect measurements, and they inherently contain regional and seasonal systematic biases and random errors. To correct these, satellite precipitation data are often calibrated with ground-based observations. The Global Precipitation Climatology Project (GPCP) played a pioneering role in developing calibration algorithms for satellite-only precipitation estimates, particularly in generating its widely used Satellite Gauge (SG) products at 2.5° monthly resolution. To correct regional biases in multi-satellite estimates, the satellite-only fields were first adjusted by multiplying them with a ratio. The ratio is between the large-scale average from gauge analyses and the corresponding large-scale average of the multi-satellite estimate, calculated using a 5 × 5 moving window. This bias-adjusted satellite field was then merged with the gauge analysis through inverse error variance weighting, which yields the final SG precipitation product (Adler et al., 2018, 2003; Huffman et al., 1997).

Mitra et al. (2009) combined the TMPA satellite product with rainfall data from IMD rain gauges to create a daily merged gauge satellite dataset, named as NMSG having a spatial resolution of 1°. The NMSG product offers enhanced accuracy and reliability by integrating gauge observations with satellite estimates and making it a more robust representation of daily precipitation. A two-step strategy has been developed by Xie and Xiong (2011) to improve multi-satellite precipitation estimates by integrating them with gauge observations. In the first step, multi-satellite data is adjusted so that its rainfall distribution matches the gauge data. The systematic biases in the multi-satellite precipitation fields are removed through probability density function (PDF) matching between satellite and gauge data. In the second step, the bias-corrected CMORPH is treated as the first guess. The gauge analysis is treated as the observation. The optimal interpolation (OI) method is used to adjust the first guess toward the gauge observations, based on their error statistics. Mega et al. (2014) describe the development of the GSMaP_Gauge product, where the original GSMaP satellite precipitation estimates are bias-corrected using a Probability Density Function (PDF) matching technique, and then further adjusted with CPC daily gauge analysis (0.5^o resolution). This two-step procedure improves the agreement of GSMaP with ground observations.

The IMERG (Integrated Multi-satellitE Retrievals for GPM) final run product corrected multi-satellite only precipitation estimates (0.1°/half-hourly) at the monthly scale by leveraging the 1° monthly precipitation datasets from the Global Precipitation Climatology Centre (GPCC) (Huffman et al., 2019). Gairola et al. (2015) improved rainfall estimation over India, particularly during the southwest monsoon season, by combining data from, Kalpana-1 satellite and Rain gauge data. The technique used is called successive correction method or objective analysis. The objectively analysed rainfall showed noticeable improvement over satellite-only estimates, especially in southern India. Ma et al. (2020) designed a new calibration method called the Daily Spatio-Temporal Disaggregation Calibration Algorithm (DSTDCA) to calibrate IMERG (0.1^o/ half hourly) precipitation data at daily scale by using APHRODITE (Asian Precipitation - Highly-Resolved Observational Data Integration Towards Evaluation) (0.25^o/ daily) ground based gridded dataset over Asia. They named the new dataset as AIMERG having 0.1^o spatial resolution and half hourly temporal resolution. The IMERG half-hourly (0.1°) data are aggregated to daily scale to derive spatial disaggregation weights using a 3×3 moving window. The spatial weights capture relative rainfall patterns by comparing central grid values with neighbourhood averages. The temporal disaggregation weights are computed as ratios of half-hourly to daily IMERG rainfall. The daily APHRODITE (0.25°) data are combined with IMERG spatial weights for spatial calibration. Finally, calibrated daily IMERG data is downscaled to half-hourly using temporal weights, producing high-resolution rainfall estimates. Xu et al. (2021) used the DSTDCA algorithm developed by Ma et al. (2020) to improve the IMERG estimates by using daily precipitation data from National Oceanic and Atmospheric Administration (NOAA) Climate Prediction Center (CPC) over Beijing-Tianjin-Hebei urban agglomeration. The IMERG Calibrated data of this study performed much better than IMERG (Final). Kumar et al. (2022) adjusted the high-resolution rainfall product GSMaP (Global Satellite Mapping of Precipitation) (0.1°/ hourly) over India using IMD rain gauge gridded measurement (0.25°/ daily). They used the procedure developed by Mega et al. (2014).

2.6 Climate change study on Rainfall Erosivity

Intergovernmental Panel for Climate Change (IPCC) reported in 2019 that the climate change could exacerbate the current land degradation and soil erosion scenario due to extreme precipitation events. The intensification of rainfall will directly enhance its erosive potential and accordingly rainfall erosivity will be increased. As per RUSLE method the soil loss from an area is directly influenced by rainfall erosivity factor, provided that all other factors remain unchanged, thus it is evident that any alteration in rainfall patterns due to climate change will significantly impact soil erosion dynamics (Nearing, 2001). The interaction between shifting climatic patterns and changing land use practices can substantially accelerate global water-induced soil erosion. Projections indicate that these combined influences may lead to an estimated 30% to 60% rise in soil erosion rates (Borrelli et al., 2020; Panagos et al., 2022a). A detail understanding of how climate change influences the R factor is crucial for devising improved land resource management strategies.

2.6.1 Regional Studies

Nearing (2001) was one of the pioneering researchers to explore the effect of climate change on rainfall erosivity. They used empirical formula proposed by Arnoldous (1980). They used two Atmosphere-Ocean Global Climate Models to simulate how rainfall might change under climate change scenarios in the 21st century in the United States. They then used these rainfall projections to estimate how rainfall erosivity might change over time. In Africa, Maeda et al. (2010) investigated the Eastern Arc Mountains in Kenya, a region vulnerable to soil erosion due to steep slopes and intensive rainfall. They computed the R factor using the method developed by Renard and Freimund (1994) and analysed under three climate change scenarios (A1B, A2, B1) based on ECHAM5 GCM projections. In Japan, Shiono et al. (2013) examined future rainfall erosivity in farmland areas using the method proposed by Yu et al. (2001). They utilized daily precipitation data from the regional climate model RCM20 under the A2 scenario to project changes in R-factor. Southeast Asia has been represented by studies such as Plangoen and Babel (2014) for the Upper Nan watershed in Thailand, where the R-factor was estimated based on the observed relationship between monthly precipitation and rainfall erosivity. They used four climate models under A2 and B2 scenarios to predict R-factor changes from 2011 to 2098. Pheerawat and Udmale (2017) similarly investigated the Huai Luang watershed in Northeastern Thailand, establishing a relationship between monthly precipitation and monthly R-Factor to compute the future R factors under RCP4.5 and RCP8.5 scenarios. In Australia, Yang et al. (2015) developed a daily rainfall erosivity model for the Greater Sydney Region and used high-resolution (2-km) regional climate model projections for 2040–2059.

In Brazil, de Mello et al. (2015) projected future increases in rainfall erosive power in the Grande River Basin using empirical approach of Renard and Freimund (1994) for computing R factor under the A1B scenario, analysing three time slices: 2011–2040, 2041–2070, and 2071–2098. Almagro et al. (2017) used downscaled outputs from HadGEM2-ES and MIROC5 under RCP4.5 and RCP8.5 and applied 84 region-specific regression equations (Oliveira et al., 2014) to estimate historical and projected R-factor values. In the United States, Biasutti and Seager (2015) employed downscaled rainfall data from 21 CMIP5 models, calculating R-factor using Renard and Freimund (1994), and concluded that rainfall erosivity is expected to increase under climate change across most regions.

Central Asia has been investigated by Duulatov et al. (2019) and Gafforov et al. (2020). Both studies used Renard and Freimund (1994) and analysed multiple GCMs under RCP2.6, RCP4.5, and RCP8.5 emission scenarios for future periods ranging from 2030 to 2070. In Southern Europe, Vantas et al. (2020) estimated R factor using monthly erosivity density in Greece, while Panagos et al. (2022, 2017) applied Gaussian Process Regression to project future R factor under multiple GCMs and emission scenarios. Unlike conventional regression models, GPR treats regression as a probabilistic problem. These studies underscore the importance of statistical and machine learning approaches in capturing regional variations in rainfall erosivity under climate change.

China has performed several studies assessing future rainfall erosivity under different warming scenarios. Li et al. (2021) predicted rainfall erosivity under stabilized 1.5–2°C warming using a daily data approach proposed by Zhang et al. (2002). Wang et al. (2023) evaluated rainfall erosivity using bias-adjusted CMIP6 models under SSP126 and SSP585 scenarios and employed the method of Xie et al. (2016) for R factor computation. These studies indicate that large portions of China may experience significant increases in rainfall erosivity.

In Iran, Azari et al. (2021) examined future R factor variations across different homogeneous precipitation zones, using regression equations under three GCMs (RCP4.5 and RCP8.5). Hateffard et al. (2021) focused on central Iran, computing R-factor using the empirical formula of Arnoldous (1980) with HadGEM2-ES projections under RCP2.6, 4.5, and 8.5 for 2050 and 2070.

2.6.2 Global Studies

Global-scale studies on rainfall erosivity provide insights into broad patterns of climate change impacts on soil erosion. Panagos et al. (2022b) conducted the first global-scale projection of rainfall erosivity under climate change, employing 19 GCMs with RCP2.6, 4.5, and 8.5 emission scenarios. They applied Gaussian Process Regression (GPR) to predict the R-factor for the periods 2041–2060 and 2061–2080. More recently, Chen et al. (2024) examined rainfall erosivity at a global scale, establishing a strong power-law relationship between precipitation and the R-factor. They used multiple CMIP6 Shared Socioeconomic Pathway (SSP) scenarios (SSP126, SSP245, SSP585) to estimate future R-factor values, providing one of the most comprehensive assessments of projected global rainfall erosivity.

2.6.3 Indian Studies

India has been the focus of several studies assessing future rainfall erosivity under both river basin and regional scales. Mondal et al. (2016) examined part of the Narmada River Basin, computing R-factor using the Arnoldous (1980) method applied to HadCM3 (A2, B2) and CGCM3 (A1B, A2) projections. Khare et al. (2017) assessed the Mandakini

River Basin using statistically downscaled HadCM3 outputs under the A2 scenario, applying the empirical approach proposed by Babu et al. (2004) for R-factor computation. Towheed and Roshni (2021) studied the Kosi River Basin, employing Renard and Freimund (1994) with four GCMs under RCP2.6, RCP4.5, and RCP8.5 scenarios, while Das and Jain (2023) predicted future R-factor under CMIP6 SSP245 and SSP585 using Gaussian Process Regression for entire India. Islam and Chakma (2024) analysed the Jhelum Catchment using six CMIP6 models and the R factor was computed by an equation derived using Modified Fournier Index (Renard and Freimund, 1994).

2.6.4 R factor Estimation Methods

Across global, regional, and Indian studies, empirical methods such as Arnoldous (1980) and Renard and Freimund (1994) remain widely applied due to their simplicity and ability to estimate R-factor from available rainfall data. The Babu et al. (2004) and Yu et al. (2001) methods are found to be used in some basin-specific studies. The Modified Fournier Index (MFI), often combined with regression equations (Renard and Freimund, 1994), has been applied to quantify R-factor across heterogeneous climatic zones, as seen in studies from India, Brazil, and Iran. Moreover some more approaches such as Zhang et al. (2002) and Xie et al. (2016) are used in China and Yu et al. (2001) used in Japan.

Recent advances have seen the application of statistical and machine learning approaches, most notably Gaussian Process Regression, which allows probabilistic modelling of R-factor under multiple GCM projections and scenarios.

2.7 Empirical Equation for computing Rainfall Erosivity

As per RUSLE handbook, the computation of R factor needs very high temporal resolution pluviographic rainfall data for an extended period (Wischmeier and Smith, 1978). In most part of the world, such long term high-resolution rainfall data are very scarce (Cohen et al., 2005; Yu et al., 2001). Due to such unavailability of required data, researchers proposed some simplified methods to evaluate the R factor based on readily available data along with various hydrologic or geographical parameters. Many researchers used annual precipitation to predict Rainfall erosivity factor and found a significant correlation (Bergsma et al., 1996; Roose, 1975; Stocking and Elwell, 1976; Torri et al., 2006; Xin et al., 2011; Yang et al., 2003). The reason for choosing annual rainfall data may be due to its availability and reliability in many parts of the world. Among the researchers Roose (1975) was one of the first to relate annual precipitation with annual rainfall erosvity factor (R), he proposed that the long term rainfall erosivity factor is 0.5 times the mean annual rainfall for the west Africa region. He used this relation to prepare the isoerodent map for west Africa (Morgan,1986). Later, Stocking and Elwell (1976) in Rhodesia found that mean annual rainfall can be related well with long term rainfall erosivity factor. They gave a table of mean annual rainfall and respective Rainfall erosivity factor (R) values. They suggested a change of 400 MJ.mm.ha^{-1}.h^{-1}.year^{-1} of R factor per 100 mm increase in mean annual rainfall (K. G. Renard and Freimund, 1994). In recent times also many researchers have used annual precipitation to get rainfall erosivity factor. Among which Lee and Heo (2011), who used a linear equation to find rainfall erosivity for Korea and Bonilla & Vidal (2011), who used a power function to find rainfall erosivity factor for Central Chile are worth mentioning.

Although the method mentioned in RUSLE handbook (Renard et al., 1997) gives the accurate determination of Rainfall Erosivity Factor (R), but many studies suggest that monthly rainfall data can provide a reasonable estimate of R factor in various parts of the world (K. G. Renard and Freimund, 1994). But it is suggested to use those equations in a location with similar climatic conditions as the source location. The use of monthly or daily rainfall data can provide more information regarding rainfall erosivity of individual storm events more accurately than annual rainfall data (Xin et al., 2011). Monthly erosivity also helps in land management in the region of high temporal variation of rainfall throughout the years (Diodato, 2004; Panagos et al., 2014). Other than Annual and monthly precipitation, many researchers used various combinations of parameters to predict the Rainfall erosivity factor. One very popular among those is Modified Fournier Index (MFI) developed by Arnoldous (1977) in Morocco. The monthly rainfall of each month was combined with the annual rainfall to establish the index. The index showed a significant correlation with rainfall erosivity factor, and using this index he produced erosivity maps of the Middle East, Africa (part in the north of the equator) and 16 countries of European Union (Morgan R.P.C., 1986). Later many researchers used MFI to get rainfall erosivity factor in various parts of the world. Ferro *et al.* (1991) used the average value of MFI for N no. of years and successfully calculated R factor of southern Italy and south-eastern Australia. Renard and Freimund (1994) proposed two pairs of composite relationships to relate R Factor with average annual rainfall and MFI. The composite relationships are a combination of polynomial fit and power function fit.

Some more such relationships are as follows, Schulze and Smith (1982) in South Africa related the R factor, calculated from 13 key stations, with one of the four possible indices viz. total rainfall, effective rainfall, MFI and burst factor. Spanish Nature Conservation Institute used maximum monthly precipitation, precipitation from October to May, and the ratio of the square of maximum annual daily rainfall to the sum of maximum daily rainfall of all the months in that year (Hernando et al., 2015; ICONA, 1988). Loureiro and Coutinho (2001) developed some multiple linear regression models and found a significantly good result. They tried to relate monthly EI30 values with rain10 and days10 for Portugal. The rain10 is the monthly summation of daily rainfall having value greater than 10 mm, and days10 is the number of days of a month having the daily rainfall value greater than 10 mm. Shamshad *et al.* (2008) proposed three procedures by combining rain10, days10, storm rainfall, duration and Fournier index to compute rainfall erosivity factor for Malaysia. MedREM was proposed by Diodato and Bellocchi (2010) for the Mediterranean region. They developed a complicated model and incorporated annual maximum daily precipitation and a coefficient dependent on longitude to predict Rainfall erosivity factor. In India also some studies related to the derivation of an alternative method for calculating rainfall erosivity factor were performed. Singh *et al.* (1981) proposed an annual and seasonal rainfall erosivity equation for entire India. They used average yearly rainfall to get annual R factor, and seasonal average rainfall (June to September) to get seasonal R factor (Farhan and Alnawaiseh, 2018; Ghosh et al., 2013; Khare et al., 2017b; Kumar et al., 2014). Babu *et al.* (2004) prepared a refined Iso-erodent map of India by using rainfall data of 123 stations. They used annual rainfall to get the R factor value, and the relationship holds good when the yearly rainfall lies between 340 mm and 3500 mm (Benavidez et al., 2018; Kalambukattu and Kumar, 2017).

2.8 Methods of Disaggregation of Rainfall

Rainfall disaggregation models are basically employed to derive sub-daily rainfall time series from daily data. Onof et al.(2000) classified the different methodologies used for rainfall disaggregation into four distinct categories based on their underlying principles and approaches. These include complicated process-based meteorological models, multi-scale stochastic techniques such as multi-fractal cascades, statistical models that rely on observed rainfall characteristics, and point process stochastic models utilizing Poisson cluster mechanisms. The poisson clustered models are commonly favored due to their adaptability and the remarkable accuracy (Burton et al., 2010; Cowpertwait et al., 2013).

They are also advantageous when used in application such as climate change (Burton et al., 2010).

Many researches on rainfall modelling has utilized two distinct Poisson clustered approaches: Neyman Scott and Bartlett Lewis. Diez-Sierra and del Jesus (2019) used Neyman Scott process to generate synthetic hourly rainfall data in Spain. This work provided a robust machine learning methodology to generate realistic hourly rainfall from daily records in Spain, improving upon earlier regression methods.

Diez-sierra et al. (2023) developed a python library called NEOPRENE, which is the first open-source python library designed for stochastic rainfall simulation built upon the spatiotemporal Neyman Scott process. NEOPRENE is a powerful and robust tool that can be used for analysis of extreme rainfall events and the disaggregation of rainfall data for finer resolution.

2.8.1 Application of Disaggregation of Rainfall

The rainfall disaggregation method has been used extensively in many previous studies. Some of the major applications are as follows: disaggregation of daily rainfall for continuous watershed modelling (Socolofsky et al., 2001). They applied on Upper Charles River Watershed (UCRW), Massachusetts for this purpose. After using disaggregated hourly rainfall, the streamflow simulation improved compared to using hourly rainfall from outside the watershed and the total contaminant loads were simulated accurately. The hydrology simulation of Xiaolihe Watershed, Yellow river (He et al., 2010). The hourly rainfall series was applied to simulate hydrology and sediment transport in Xiaolihe Watershed using the Digital Watershed Model. The results showed that the method works well for disaggregating daily rainfall into hourly data and can support large-scale calculations for rainfall-runoff and soil erosion simulations. Mirhosseini et al. (2013) performed a study on impact of climate change on rainfall IDF curves in Alabama. This study applied a modified form of the stochastic downscaling approach introduced by Socolofsky et al. (2001). Tayşi and Özger (2022) temporally disaggregated future GCM projections to develop IDF curves, which were then used to evaluate urban flood risks in Northeastern Turkey. They used Bartlett - Lewis based HYETOSMinute R package for rainfall disaggregation. Alzahrani et al. (2023) examined the effectiveness of temporal disaggregation techniques in converting daily to sub-daily rainfall for Intensity-Duration-Frequency (IDF) curve estimation in a changing climate. In their study they proposed new simple stochastic model for rainfall disaggregation.

Studies have also highlighted the application of rainfall disaggregation techniques in assessing rainfall erosivity. One such study is by Jebari et al. (2012), where they used cascade disaggregation model to disaggregate daily rainfall to some finer time scale rainfall data to compute rainfall erosivity and soil erosion. They claimed that the outcomes were encouraging and could serve as a valuable resource for improving the management of soils prone to erosion. They used this method to calculate the soil erosion of Jannet catchment of Tunisia.

2.9 Conclusion from the literature review and research gap

As per ISRO (2021), approximately 36.20 million hectares, accounting for 11.01% of India's total geographical area, are affected by land degradation caused by water erosion. The detachment and loss of fertile topsoil is the primary consequence of water erosion, which in turn triggers various other environmental challenges. Therefore, it is necessary to study the various aspects of water induced soil erosion. Among the key factors that influence water erosion, the erosive power of rainfall plays a crucial role. With the starting of climate change, this issue has further intensified, as rainfall erosivity depends on both rainfall depth and intensity. The increasing frequency of high intensity rainfall events under changing climatic conditions has further aggravated the soil loss scenario.

The literature reveals that numerous studies have been conducted on rainfall erosivity across India at both national and regional scales. Most of these studies have relied on empirical equations to estimate the rainfall erosivity factor (R-factor), with only a few focusing on small catchments where the standard method outlined in the Revised Universal Soil Loss Equation (RUSLE) Handbook was applied. A notable exception is the isoerodent map of India developed by Babu et al. (2004, 1978), in which the R-factor was computed using the standard method; however, interpolation techniques were employed to generate the final map. Due to the application of interpolation methods, there is a strong probability that a significant level of uncertainty will be observed in the rainfall erosivity values of transition areas. Moreover, such stations are not uniformly distributed, which leads to erroneous results in areas with limited number of stations or no stations. However, in recent times, the availability of remotely measured precipitation data has changed the scenario, and it has become very useful in computing R factor in the data-scarce region. Precipitation data is now readily accessible with exceptional temporal and spatial resolution. Building upon this technological progress and addressing the identified research gaps, the present study aims to generate a national scale rainfall erosivity map for India using high-resolution satellite precipitation data. Additionally, this study undertakes an extensive spatiotemporal analysis of rainfall erosivity across the country, an area of research that remains largely unexplored in the Indian context.

The concept of return period has been widely applied across various scientific and engineering disciplines; however, its application in rainfall erosivity studies remains relatively limited. In particular, no such studies have been reported in the Indian context. Also, there is not any prior global research which utilized the high-resolution satellite precipitation products for this purpose. Thus, this study presents an approach that combines the standard procedure of frequency analysis with the R factor calculation method from the RUSLE handbook, to estimate and map the rainfall erosivity factor for various return periods using high spatiotemporal resolution precipitation product.

The satellite-based precipitation products, despite their remarkable spatial and temporal coverage, are not without limitations. Literature indicates that the IMERG precipitation product often exhibits reduced accuracy in regions characterized by complex topography and high-intensity rainfall. To address these discrepancies, several studies have attempted to calibrate IMERG data against various ground-based rainfall observations. Among the available ground-based datasets, the IMD 0.25° gridded rainfall product is one of the most widely used and reliable observational datasets in India. However, no study has employed this IMD gridded dataset for the calibration of IMERG data to date. Thus, the present study undertakes the calibration of IMERG precipitation estimates using the IMD dataset.

Intergovernmental Panel for Climate Change (IPCC) reported in 2019 that the climate change could exacerbate the current land degradation and soil erosion scenario due to extreme precipitation events. The intensification of rainfall will directly enhance its erosive potential and accordingly rainfall erosivity will be increased. As per RUSLE method the soil loss from an area is directly influenced by rainfall erosivity factor, provided that all other factors remain unchanged, thus it is evident that any alteration in rainfall patterns due to climate change will significantly impact soil erosion dynamics. The interaction between shifting climatic patterns and changing land use practices can substantially accelerate global water-induced soil erosion. A comprehensive understanding of how climate change influences the R-factor is crucial for devising improved land resource management strategies. Many regional as well as global studies have been undertaken to investigate how climate change alters the R factor in all over the world using CMIP6 or earlier CMIP datasets. The future precipitation data from GCMs are provided on a daily scale, whereas the standard RUSLE methodology necessitates sub-daily rainfall data for accurate computation of the R factor.

The literature revealed that in most of the past studies, future rainfall erosivity was predicted by generating equation or alternative models that derive erosivity from daily rainfall data, rather than applying the standard computation method. In hydrological research, rainfall disaggregation techniques have been widely employed in studies requiring fine temporal resolution data. However, the application of rainfall disaggregation approaches in the estimation of rainfall erosivity remains very limited. Notably, no study in India has yet employed rainfall disaggregation for erosivity estimation, nor has this approach been utilized in climate change impact assessments globally. In this research work an effort will be made to disaggregate the daily rainfall to hourly rainfall and rainfall erosivity is calculated by standard method.

Chapter 3

Preparation of Rainfall Erosivity factor map and analysis of spatiotemporal variation

3.1 Introduction

Rainfall erosivity represents the potential of rainfall to initiate soil erosion (Lal, 2001). The Rainfall Erosivity factor (R) or simply R Factor of the Universal Soil Loss Equation (USLE), as derived by Wischmeier and Smith (1978), was determined based on extensive study records from various research sources. While keeping other factor constant, the amount of soil loss happening in a cultivated field exhibits a direct proportionality to the parameter represented by the multiplication of the energy of a rainfall event (E) and the maximum 30-minute intensity (I_{30}) of that rainfall event. Rainfall energy alone does not effectively represent the erosive potential. As a long, gentle rain and a short, intense storm can yield the same energy value despite differing impacts. However, instead of that, raindrop erosion is more strongly driven by rainfall intensity. The I_{30} factor captures the high intensities crucial for detachment and runoff, while the EI_{30} term represents the interaction between total storm energy and peak intensity, reflecting the combined effects of particle detachment and transport capacity. The accumulation of EI_{30} values of the storm events within a specific timeframe serves as a quantitative assessment of the erosive capacity of rainfall in that duration. The annual average of cumulative EI_{30} values is known as Rainfall Erosivity Factor (R) (Renard et al., 1997). In the Revised Universal Soil Loss Equation (RUSLE), the fundamental concept of the R factor remains unchanged from the original USLE, with modifications applied only to the equation used for calculating the rainfall event energy (E). The R factor of RUSLE captures the erosive potential of rain drop impact and associated surface runoff. It reflects both the intensity and volume of precipitation along with their role in initiating soil detachment and erosion during storm events.

A spatially distributed R factor map is crucial for a country like India due to its diverse topography, wide climatic zones and varied rainfall patterns. Soil loss in India significantly affects agricultural productivity of the country. A spatially distributed soil loss map helps in identifying the erosion prone areas and supports sustainable land management practices. To compute the R factor high temporal resolution rainfall data is required, but this type of data is scarce in India. Scarcity of such data is more profound in remote and mountainous regions where the rain gauge network is sparse or absent. Moreover, rain gauge data represent point measurements and do not adequately capture the spatial variability of rainfall, specifically in complex terrains. Consequently, interpolating these sparse data to generate R factor maps introduces significant uncertainties. But satellite rainfall data provides an effective solution to this limitation due to its spatially continuous precipitation measurements with high temporal resolution. A widely used such satellite rainfall data is IMERG (Integrated Multi-satellitE Retrievals for GPM) developed by NASA, which has 0.1^{o} spatial resolution and 30-minute temporal resolution.

In this study, IMERG data are used to compute the R factor and generate a high resolution R factor map for India without using interpolation method. This approach utilises the advantages of satellite observations to improve the accuracy and spatial coverage of rainfall erosivity assessments across India. Furthermore, this chapter presents an extensive analysis of the spatiotemporal variation of the R factor over India, providing valuable insights into its annual, seasonal, monthly and regional patterns and trends.

3.2 Materials and methodologies

3.2.1 Study area

In terms of geographical extent, India falls in the seventh position among all the countries of the world, having an area of 32,87,263 sq. km. The country is situated entirely in the northern hemisphere. The latitudinal extent of the mainland of India is between 8° 4' N and 37° 6'N, and the longitudinal extent is between 68° 7' E and 97° 25' E. India's climate is predominantly characterized as Tropical monsoon. The climate is subdivided into four main seasons in India, the winter starts in January and ends in February, the Pre-monsoon starts in March and is available till May, the Southwest monsoon starts in June and lasts up to September, and the Post monsoon starts in October and ends in December as per Indian Meteorological Department (IMD). India consists of six major climate subtypes as per the Koppen Geiger climate classification system, namely tropical wet, tropical wet and dry, arid, semi-arid, humid sub-tropical and mountain. The amount of rainfall in India ranges from 300-500 mm in regions like Rajasthan in the west to 3,500-4,000 mm in regions like Meghalaya in the North-East (Jain, 2019). In July, a peak rainfall of about 300 to 350 mm is experienced by India, while January witnesses the lowest rainfall of around 16 to 18 mm (Poornima et al., 2023). The primary divisions of the Indian mainland include the great mountain range, the plains surrounding the Ganga and Indus rivers, the desert area, and the southern peninsula. The study will be focused on Mainland India, however the Ladakh Union Territory also excluded due to the presence of a lot of missing precipitation data in IMERG half hourly dataset. The study area is shown in Figure 3.1.

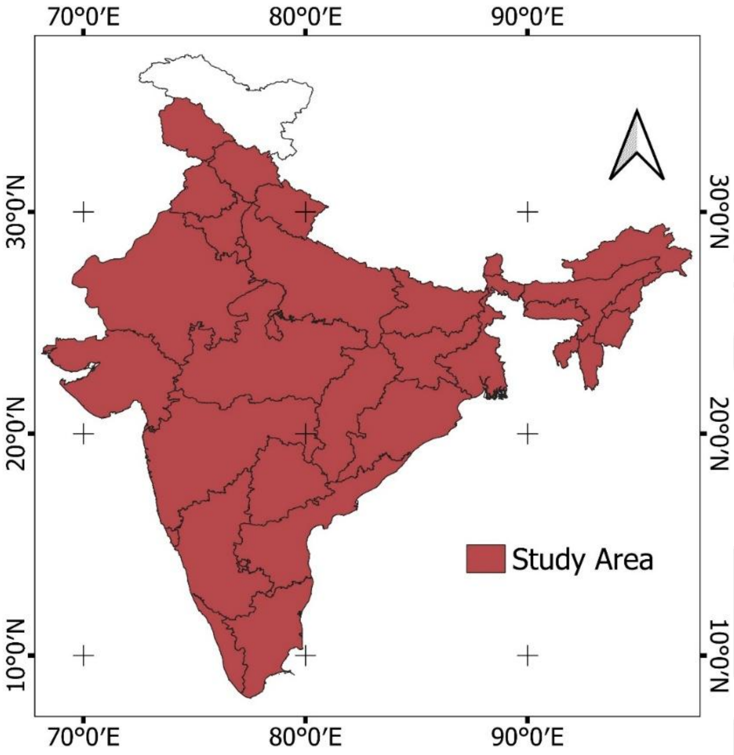

Figure 3.1 Study area

3.2.2 Global Precipitation Measurement Mission (GPM) Product

The IMERG is the multi-satellite precipitation algorithm produced by NASA (Huffman et al. 2019). IMERG is a collection of a suite of multi-satellite precipitation products that offer exceptionally high spatial (0.1° x 0.1°) and temporal resolution (half-hourly). The majority of satellite-based precipitation products rely on Passive Microwave Sensors, primarily obtained from low-Earth-orbit (leo) platforms. However, IMERG stands out by utilising a combination of Leo-satellites and Geosynchronous Earth Orbit (geo) infrared (IR) estimations to provide the precipitation data. In the research version product, bias adjustments are applied using monthly rainfall data from the Global Precipitation Climatology Center (GPCC). Three distinct products are available for IMERG, Early (available after four hours of detecting time), Late (available after Fourteen hours), and Final satellite gauge product (available after 3.5 months of observation month). The latest version is V06B and the product has been available from June, 2000 to till date and the spatial coverage is -180.0, -90.0, 180.0, 90.0. In our study, we have used the data from

01/01/2001 to 31/12/2020 (20 years) of the Final satellite-gauge product covering whole India, excluding the Island Union Territories. We have also excluded the Ladakh Union Territory due to the presence of a lot of missing precipitation data. Thus, the study will cover 27,338 grid points, and in each grid point the rainfall erosivity factor will be calculated.

3.2.3 Calculation of Rainfall Erosivity Factor or R factor

Brown and Foster (1987) proposed a relationship in the form of an equation to establish a connection between rainfall kinetic energy (e_r) and intensity of rainfall (i).

$$e_r = 0.29 \times [1 - 0.72 \times exp\,(-0.05.i)] \tag{3.1}$$

where e_r= energy in MJ.ha^{-1}.mm^{-1} and i = Intensity of rainfall in mm.h^{-1}

Then rainfall erosivity factor (R) can be calculated as

$$R = \frac{\sum_{i=1}^{j}(EI_{30})_i}{N} \tag{3.2}$$

where $(EI_{30})_i = (EI_{30})_i$ for storm i and j = number of storms in an N year period.

Now, $E = (\sum_{r=1}^{k} e_r v_r)$ in MJ.ha^{-1} and I_{30}= maximum 30 min intensity (mm/hr)

where v_r is the rainfall volume (mm) during the r^{th} time period of a rainfall event divided in k parts.

The Annual Rainfall Erosivity factor can be calculated as :

$$\text{Annual Rainfall Erosivity Factor} = \sum_{i=1}^{j}(EI_{30})_i \tag{3.3}$$

where $(EI_{30})_i$ denotes the EI_{30} for rainfall event i and j represents the number of rainfall events in a year.

In the calculation of R factor, all the rainfall events are not considered. The rainfall events having erosive capacity are only considered. In the RUSLE handbook (Renard et al., 1997), three conditions are given to identify an erosive rainfall event.

(1) If a rainfall event has a rainfall depth of less than 12.7 mm then it is not considered an erosive event and should be excluded from the R factor calculation.

(2) But if that rainfall event mentioned in point (1) has a record of rainfall depth of 6.35 mm or more fell in 15 min, then the rainfall event is considered as erosive and included in the calculation.

(3) A rainfall event of rainfall depth less than 1.27 mm over a period of 6 hour is used to divide a longer rainfall event into two events.

A visual representation of the above guidelines has been shown with the help an example in Figure 3.2.

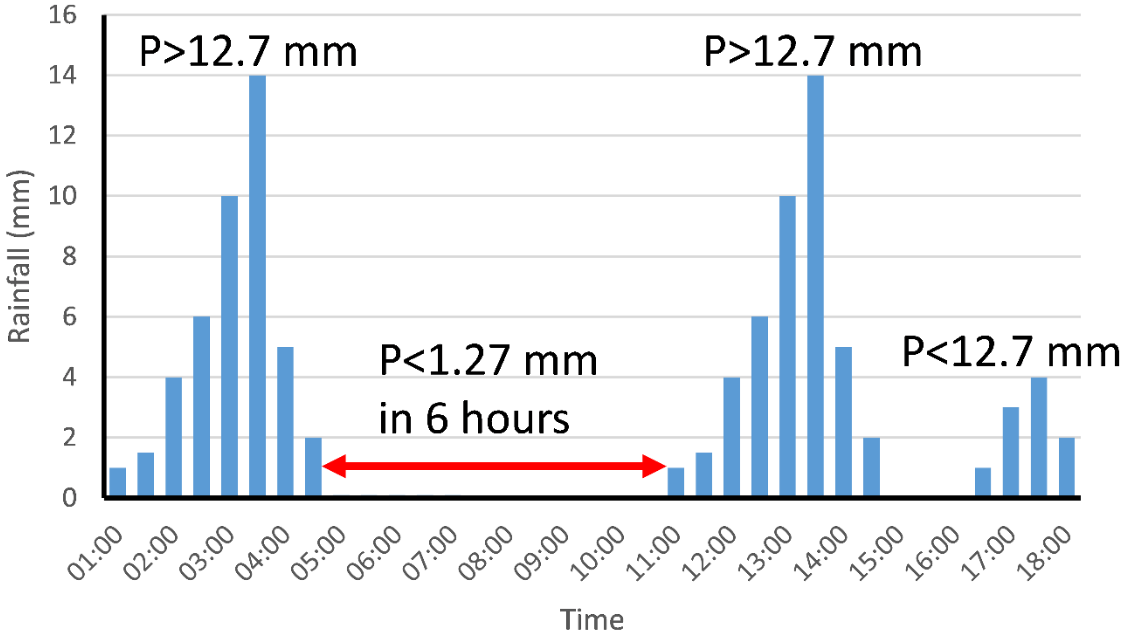

Figure 3.2 Visual representation of guidelines for erosive event as per RUSLE guidebook

3.2.4 Trend Analysis

The non-parametric Mann Kendall Trend Analysis (Kendall, 1975; Mann, 1945) is used to detect the presence of any trend in a dataset. The Mann Kendall test is among the widely applied trend detecting tests used in various environmental data (Bezak et al., 2022; Sadeghi and Hazbavi, 2015). The significance level considered is 0.05. The result of the trend analysis will give us the presence of positive trend, negative trend or absence of any trend. The Mann–Kendall test statistic is given by

$$S = \sum_{i=1}^{n-1} \sum_{j=i+1}^{n} Sgn(X_j - X_i) \tag{3.4}$$

where X_j and X_i are the sequential data values, n is the data set record length, and

$$Sgn(\theta) = \begin{Bmatrix} +1 & & \theta > 0 \\ 0 & if & \theta = 0 \\ -1 & & \theta < 0 \end{Bmatrix} \tag{3.5}$$

The mean and variance of S statistics are given as

$$E(S) = 0 \tag{3.6}$$

$$Var\ (S) = \frac{1}{18}[n(n-1)(2n+5) - \sum_{i=1}^{m} t_i(t_i - 1)(2\,t_i + 5)] \tag{3.7}$$

where n is the number of observations, m is the number of tied groups, and t_i is the number of values in the i^{th} tied group. The standardized Mann Kendall statistic Z is then calculated as:

$$Z = \begin{cases} \frac{S-1}{\sqrt{Var(S)}} & if\ S > 0 \\ 0 & if\ S = 0 \\ \frac{S+1}{\sqrt{Var(S)}} & if\ S < 0 \end{cases} \tag{3.8}$$

here, the sign of Z indicates the direction of the trend (positive for increasing, negative for decreasing), while the magnitude of Z reflects the strength of the trend. The statistical significance of the trend is determined by comparing Z with the critical value $Z_{1-\frac{\alpha}{2}}$ for a chosen significance level α (0.05 in this study). For $\alpha = 0.05$, $1 - \frac{\alpha}{2}$ will be 0.975 and from the standard normal distribution table, the Z value corresponding to 0.975 cumulative probability is 1.96. So, 1.96 is the critical Z value for Mann Kendall test at significance level, $\alpha = 0.05$ or 95% confidence. Thus, $|Z| > 1.96$ corresponds to a significant trend at 0.05 significance level. Despite its popularity, the Mann Kendall test assumes that the observations are independent. However, hydrological time series often exhibit autocorrelation, meaning that values at one time are influenced by previous values. If the time series exhibits positive autocorrelation, the standard Mann Kendall test underestimates the true variance, potentially leading to false detection of a trend. Conversely, in the presence of negative autocorrelation, the variance is overestimated, which can mask an existing trend (Hamed, 2008; Hamed and Rao, 1998).

To address the issues caused by autocorrelation, Hamed and Rao (1998) introduced the Modified Mann Kendall test, which adjusts the analysis to account for the presence of autocorrelation. The modified test gives a revised equation for variance of S statistics as follows

$$Var^* = Var\ (S).\left(\frac{n}{n_e^*}\right) \tag{3.9}$$

$$\frac{n}{n_e^*} = 1 + \left(\frac{2}{n(n-1)(n-2)}\right)\sum_{i=1}^{n-1}(n-i)(n-i-1)(n-i-2)\rho_e(i) \tag{3.10}$$

where n_e^* is the effective sample size. $\rho_e(i)$ represents the autocorrelation of the ranks of observations and calculated as inverse of the following equation

$$\rho(i) = 2\sin\left(\frac{\pi}{6}\rho_e(i)\right) \tag{3.11}$$

In this study the Modified Mann Kendall trend test has been performed over 20 years Annual R Factor data series of all the grid points at 0.05 significance level (95% confidence level).

While the Mann Kendall and Modified Mann Kendall tests detect the presence and direction of trends, they do not quantify the magnitude of change. For this purpose, the Sen's slope estimator (Sen, 1968) is widely employed. Sen's method calculates the slope between all pairs of data points:

$$S_i = \frac{x_j - x_k}{j-k} \qquad i = 1,2,3, \dots \dots \dots, N \tag{3.12}$$

Where x_j and x_k are the values at times $j > k$ and N is the total number of slope estimates. The median of all S_i values give the Sen's slope. A positive slope indicates an increasing trend, while a negative slope indicates a decreasing trend.

3.2.5 Sensitivity Analysis

A sample sensitivity analysis was conducted to examine the high dependency of the R factor on rainfall intensity. For this analysis, one point from each of the agro-climatic zones of India was randomly chosen. The Planning Commission of India (currently the NITI Aayog) divided the country into fifteen agro-climatic zones based on physiography, geological formation, soil types, climate, cropping patterns, and the availability of irrigation and mineral resources. The present study includes fourteen of these zones, excluding the island region. Figure 3.3 shows the geographic areas of these agro-climatic zones along with their names and the positions of the randomly selected points. The sensitivity analysis presented the impact of rainfall intensity errors at various percentages (-50%, -20%, -10%, -5%, 5%, 10%, 20%, 50%, and 100%) on the R factor.

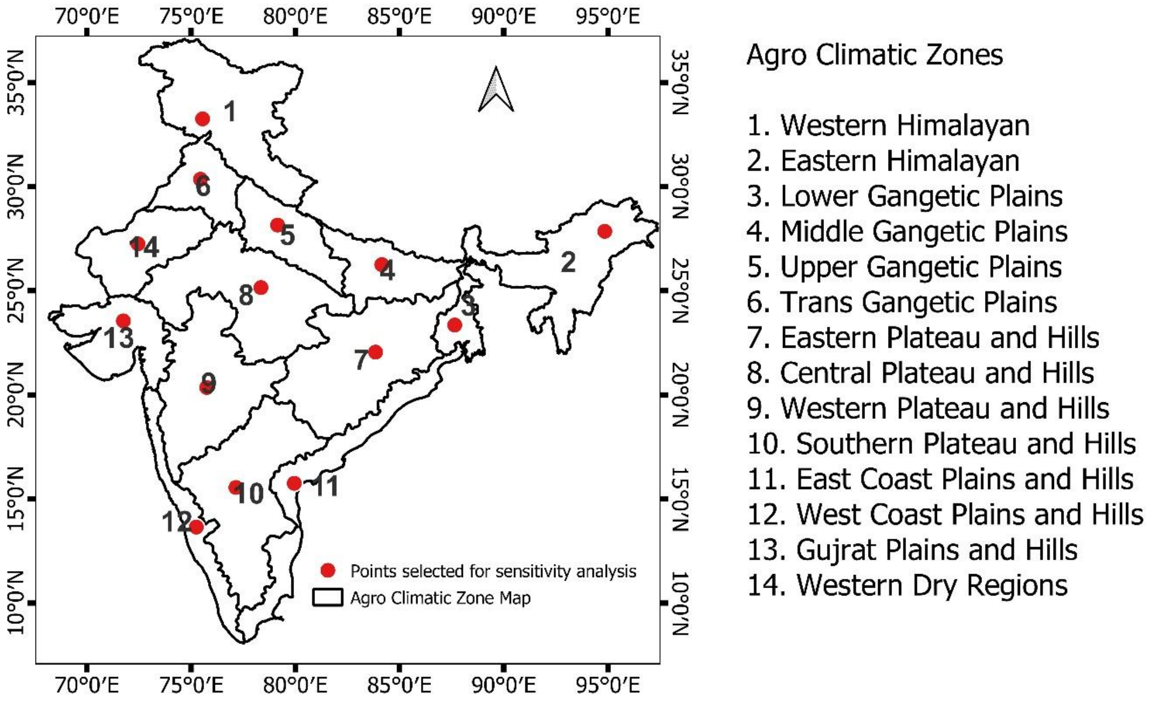

Figure 3.3 Agro Climatic Zone map of mainland India alongwith the points selected for sensitivity analysis

3.3 Results and Discussion

3.3.1 Rainfall Erosivity Factor

In this study, the methodology outlined in the RUSLE handbook (Equation 3.1 and 3.2) was followed to compute the rainfall erosivity factor (R factor). The R factor was calculated using IMERG 20 years half hourly rainfall data, spanning from 2001 to 2020. The resulting spatial distribution of the R factor across the study area is depicted in Figure 3.4 (a) For the entire study area, the spatial average of the R factor was found to be 2188.79 MJ.mm/ha.h.year. The R factor is the average value of the annual R factor and is also termed as the average annual R factor or mean annual R factor in many previous studies (Ferro et al. 1991; Aronica and Ferro 1997; Sadeghi and Hazbavi 2015; Sadeghi et al. 2017) .

The lowest R factor value recorded is 68.28 MJ.mm/ha.h.year, occurring in a location within the Lahul and Spiti district of Himachal Pradesh, characterized by a cold-arid climate with minimal precipitation. In contrast, the highest R factor value observed was 18,864.2 MJ.mm/ha.h.year, located in the Lakhimpur district of Assam. For enhanced clarity in spatial visualization, the R factor map shown in Figure 3.4 (a) is capped at the

99th percentile, corresponding to a maximum R factor value of 8655 MJ.mm/ha.h.year. The top one percentile of R factor values are predominantly concentrated in specific regions such as parts of North East India and the Western Ghats. These regions are characterized by steep terrain promoting orographic lifting which enhances rainfall intensity. Mid-range R factor values are distributed across states such as Gujarat, Odisha, West Bengal, and Madhya Pradesh, while the rest of India mostly exhibits lower R factor values, spread with clusters of mid-range values.

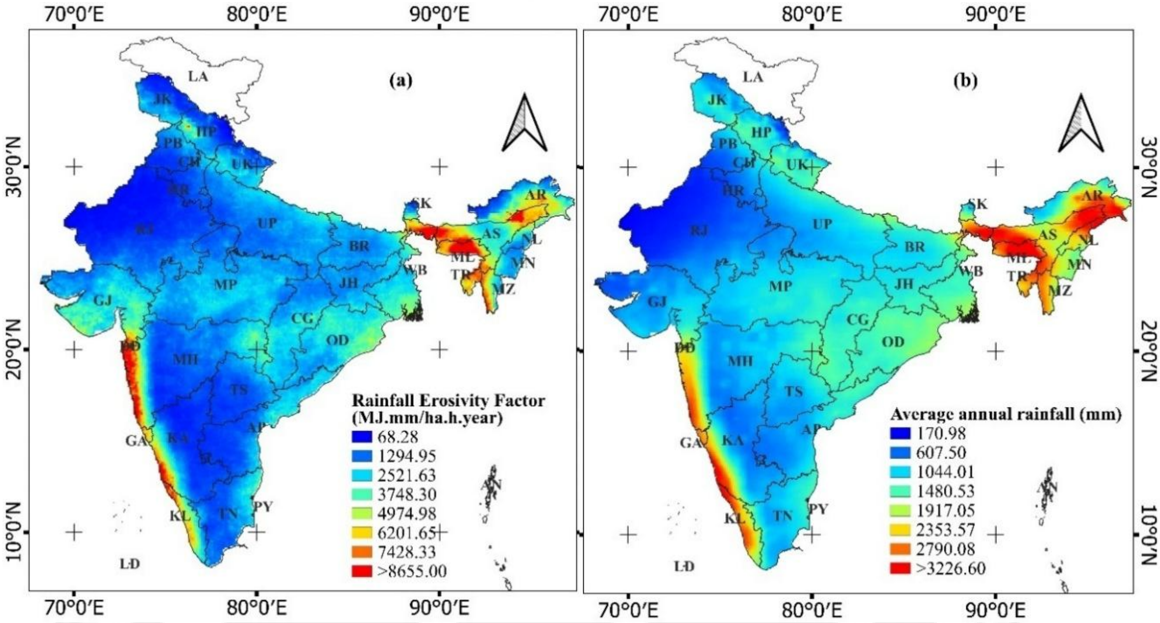

Figure 3.4 (a) Rainfall Erosivity Factor Map of the study area for the period 2001 to 2020 and (b) Average annual rainfall of the study area for the period 2001 to 2020

Additionally, the annual average rainfall map for the same period (2001–2020) is presented in Figure 3.4 (b). Similar to the R factor map, the 99th percentile value was selected as the maximum threshold to improve the clarity in visualisation of spatial representation. A comparative assessment of both the R factor and the average annual rainfall maps reveals a notable spatial similarity, which confirms a direct correlation between annual average rainfall and rainfall erosivity. This type of correlation has been documented in several prior studies. Notably, Roose (1975) was among the pioneers to establish a connection between annual precipitation and the R factor, proposing that in the West Africa region, the long-term rainfall erosivity factor is approximately half of the mean annual rainfall. More recently, researchers such as Lee and Heo (2011) applied a linear equation to estimate the R factor for Korea, while Bonilla and Vidal (2011) utilized a power function approach to derive the R factor for Central Chile.

To further validate the computed IMERG-based R factor map, a comparison was conducted with the global rainfall erosivity map developed by Panagos et al. (2017). They generated a high-resolution ground-based R factor map using rain gauge data collected from collected from 65 countries. For India, they used hourly data from 247 rain gauge stations over a nine-year period (2007–2015). Their approach employed Gaussian Process Regression (GPR) to interpolate point-based R factor measurements into a continuous map at a spatial resolution of 1 km × 1 km. We have cropped their global R factor map to our study area and presented at Figure 3.5 (b). In parallel, we computed the R factor using IMERG half-hourly satellite rainfall data for the identical nine-year period (2007-2015) and presented it in Figure 3.5 (a). The ground-based R factor map displayed a range from 0 to 12,437 MJ.mm/ha.h.year, with a mean of 3843.34 MJ.mm/ha.h.year. The corresponding IMERG based map ranged from 0 to 20,726 MJ.mm/ha.h.year, with a mean value of 2263.46 MJ.mm/ha.h.year, which is approximately 58% of the ground based mean.

A detailed spatial comparison revealed several discrepancies between the two maps. For example, within the state of Meghalaya, areas where the IMERG based R factor map indicated high erosivity values were found to exhibit considerably lower values in the ground-based map. Similarly, in the Western Ghats, the ground-based map failed to represent high R factor zones that appeared prominently in the IMERG based map. Overall, the IMERG based map predominantly exhibited lower R factor values across the study area, whereas the ground-based map showed most areas within the mid-range R factor value. Significantly, the IMERG based R factor map tends to show slightly higher maximum erosivity values in hotspot regions, suggesting that ground-based map may underestimate peak erosivity. These inconsistencies may be due to the limited density of rain gauge stations and interpolation errors present in the ground-based map. Given its reliance on continuous, gridded satellite data, the IMERG-based R factor map is considered more robust in capturing the spatial heterogeneity of rainfall across the region.

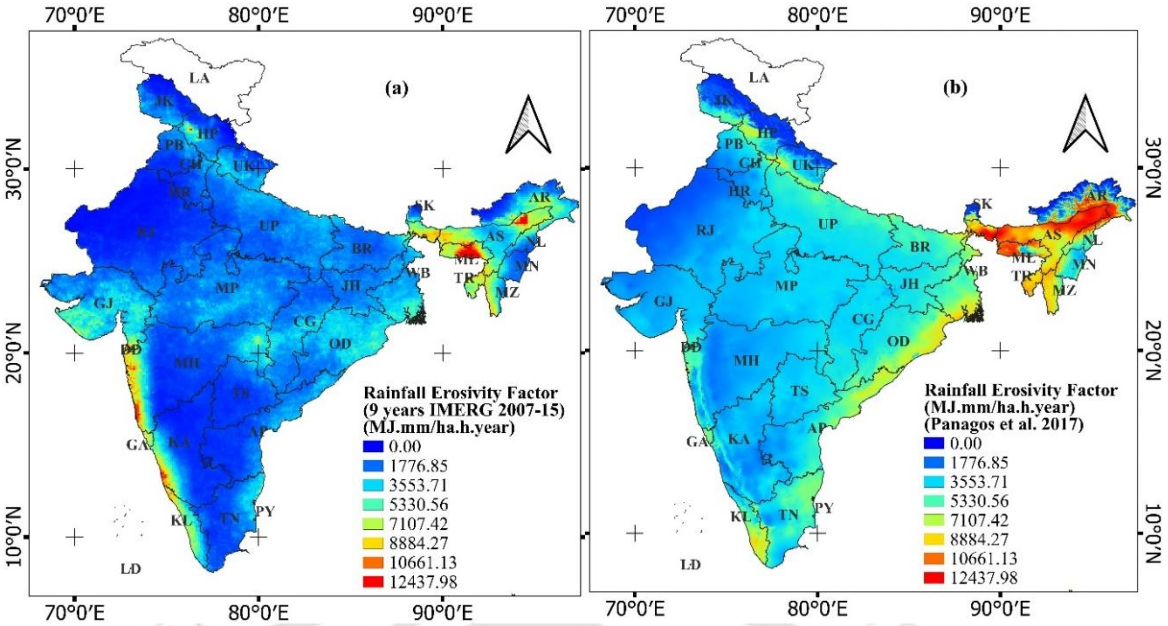

Figure 3.5 (a) Rainfall erosivity Factor map of the study area using IMERG half hourly rainfall data and (b) Rainfall erosivity Factor map using hourly rain gauge data (Panagos et al. 2017), for the period 2007 to 2015

Furthermore, the 20 year IMERG based R factor map was compared with the historical Isoerodent map of India developed by Babu et al. (1978), which was derived using data from 44 rain gauge stations. The Isoerodent map of India was created using rainfall data from 44 rain gauge stations. The spatial distribution observed in the IMERG based R factor map aligns closely with the Isoerodent map of India. However, notable variations in magnitude were identified between the two maps, the discrepancy may be due to the fact that the Isoerodent map was developed four decades ago, and the IMERG based map is using recent data. Supporting this observation, Emberson (2023) utilized IMERG data for global R factor mapping and found substantial similarity between IMERG-based and ground-based R factor maps in Europe and Asia, though notable differences were reported in other regions. Similarly, Chen et al. (2021) demonstrated a strong correlation between IMERG based R factors and those computed by rain gauge data in China. These findings underscore the applicability of satellite datasets like IMERG as reliable alternatives for calculating the R factor. This is particularly relevant in developing countries such as India, where high temporal resolution ground-based data are limited or unavailable.

A comparison was also carried out using data from an IMD rain gauge station located near Guwahati (geographical coordinates: 91.59°E, 26.11°N). The R factor was computed from 13 years of half hourly observed rainfall data at this station. Nine of these years overlap with the available IMERG dataset. For the purpose of comparison, R factor values were calculated for four surrounding IMERG grid points, as illustrated in Figure 3.6 for the same nine year period. The comparative results are presented in Figure 3.7. The analysis indicates a significant anomaly in the year 2007, where the observed R factor sharply decreased while all four grid points showed an increasing trend. If we exclude this outlier, then the mean R factor of the four grid points closely aligned with the observed station data in the remaining years. The observed R factor was found to be 7891.11 MJ.mm/ha.h.year, whereas the IMERG based average across the four grid points was 8708.42 MJ.mm/ha.h.year, approximately 10% higher than the observed value. This difference falls within an acceptable range, considering the inherent uncertainties in satellite measurements as compared to rain gauge observations.

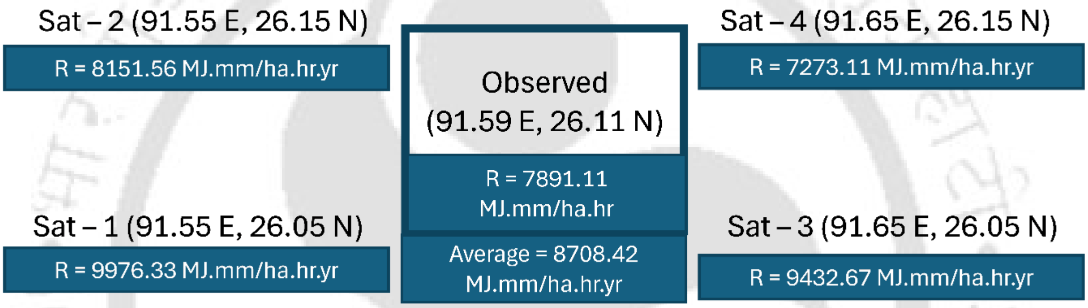

Figure 3.6 Location information of the IMERG grid points surrounding the rain gauge station of India Meteorological Department near Guwahati

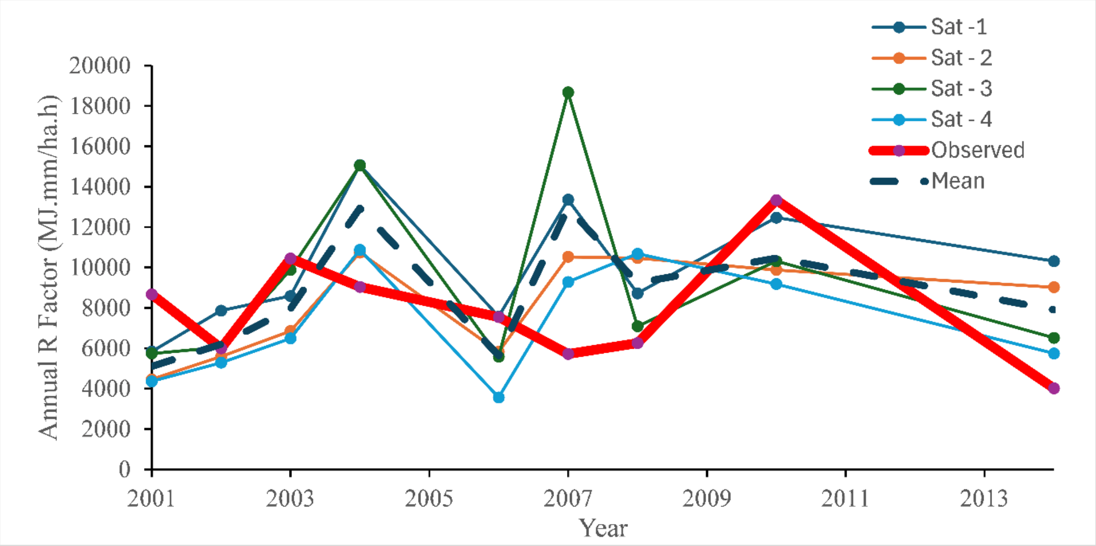

Figure 3.7 Temporal variation of annual rainfall erosivity factor of all the four IMERG grid points along with their mean value plotted against the observed annual rainfall erosivity factor

Collectively, these findings proved that high temporal resolution satellite products such as IMERG can serve as a reliable source for calculating rainfall erosivity factors, especially in regions where ground-based measurements are inadequate or unavailable.

3.3.2 Non dimensional Rainfall Erosivity Factor Map

In hydrological studies, a non-dimensional (or dimensionless) map is a valuable analytical tool that represents physical quantities in a unitless form. Such transformation is generally achieved through normalization or scaling of the parameter of interest relative to a characteristic value of the system, such as the mean, maximum or another representative statistic. This approach provides the advantage of allowing comparisons across diverse geographic regions or temporal scales, which is independent of their absolute magnitudes. By eliminating the influence of scale and units, non-dimensional maps facilitate a generalized interpretation variability.

In the present study, the rainfall erosivity factor for each pixel was made non dimensional by dividing it by the spatial mean of the R factor for the entire study area. This process produced the non-dimensional R factor map, which is presented in Figure 3.8. The results reveal considerable heterogeneity in rainfall erosivity across the study area. The minimum R factor is found to be 0.03 times the average value, while the maximum reaches as high as 8.63 times the average, indicating pronounced spatial differences.

The spatially distributed non dimensional map highlights the predominance of zones with relatively lower erosivity compared to the mean. Approximately 63.48% of the total area exhibits R factor values below the average, 28.34% of the area records values within the range of one to two times the average, while 4.56% and 2.68% of the area fall within two to three times and three to four times the average respectively. The proportion of land area exhibiting R factor values exceeding four times the average is comparatively negligible, with each class (i.e., four to five, five to six, six to seven, seven to eight, and greater than eight times the mean) contributing less than 1% of the total spatial extent. A simplified representation has been also provided in Figure 3.9, where the spatial extent of areas with R factor values below the average and those above the average are distinctly delineated. This classification offers a clear visual of R factor distribution by identification of regions that are more vulnerable to soil erosion relative to the broader spatial mean.

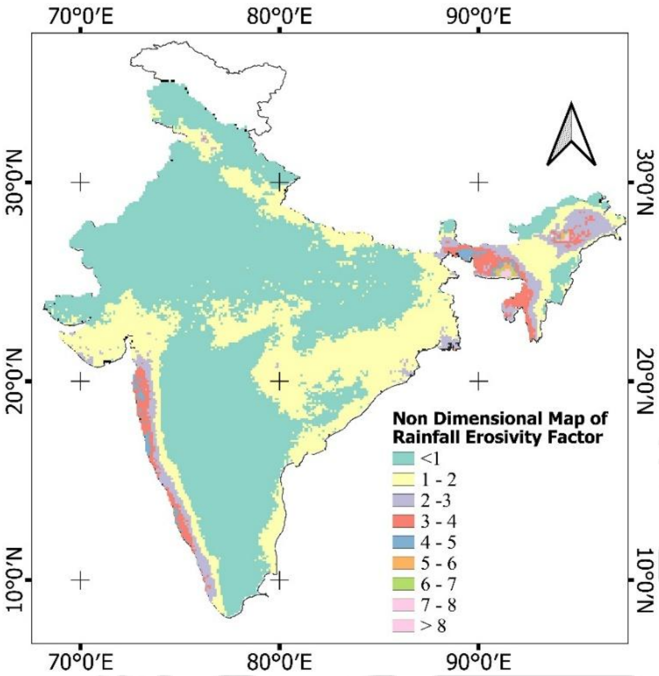

Figure 3.8 Non-Dimensional Map of Rainfall Erosivity Factor

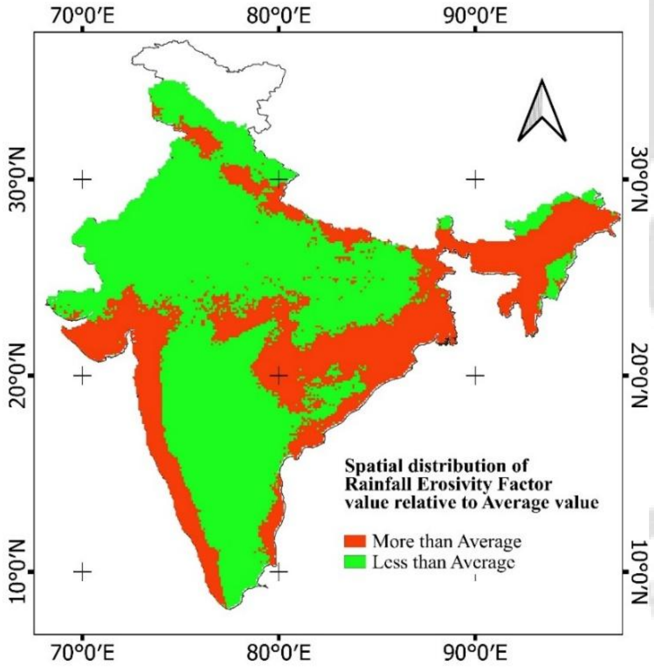

Figure 3.9 Spatial distribution of Rainfall Erosivity Factor value relative to Average value

3.3.3 Monthly variation of Rainfall Erosivity Factor

The monthly distribution of rainfall erosivity (R factor) across India reveals distinct spatiotemporal patterns that closely follow diverse climatic regimes of the country. During the months of January and February, rainfall erosivity is almost negligible throughout the study area, with only isolated detectable values observed over North East India and parts of Himachal Pradesh. In March, the spatial extent of erosivity increases slightly, though it remains largely confined to these two regions.

A substantial expansion of erosivity occurs in April and May, when higher values begin to appear not only in North East India but also over parts of the Western Ghats. With the onset of the Southwest Monsoon, erosivity reaches its peak both in intensity and areal extent. During June and September, which mark the beginning and the end of the monsoon season, erosivity is widely distributed across North East India, West Bengal, and the Western Ghats. The spatial averages for June and September are 335.99 and 327.71 MJ.mm/ha.h.month respectively. However, there is a striking difference in the maximum values recorded: 5569.36 MJ.mm/ha.h.month in June as compared to 2616.74 MJ.mm/ha.h.month in September.

Among all months, July exhibits the highest erosivity, with a mean of 655.17 MJ.mm/ha.h.month and a maximum of 5792.10 MJ.mm/ha.h.month, which can be seen from the Figure 3.10. July and August show broadly similar patterns, with most regions of India experiencing elevated values, although Tamil Nadu, Karnataka, Andhra Pradesh, and Rajasthan display comparatively low erosivity during this peak monsoon phase. In October, the influence of the retreating monsoon is distinct, with high values mostly concentrated over the Eastern Ghats, while erosivity over the Western Ghats and North East India diminishes.

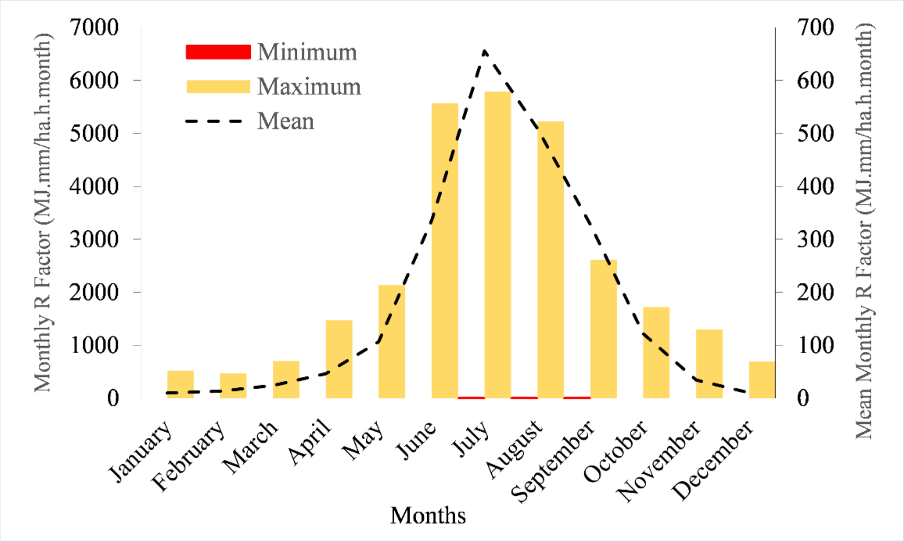

Figure 3.10 Maximum, minimum and mean of average monthly rainfall erosivity factor for the study area

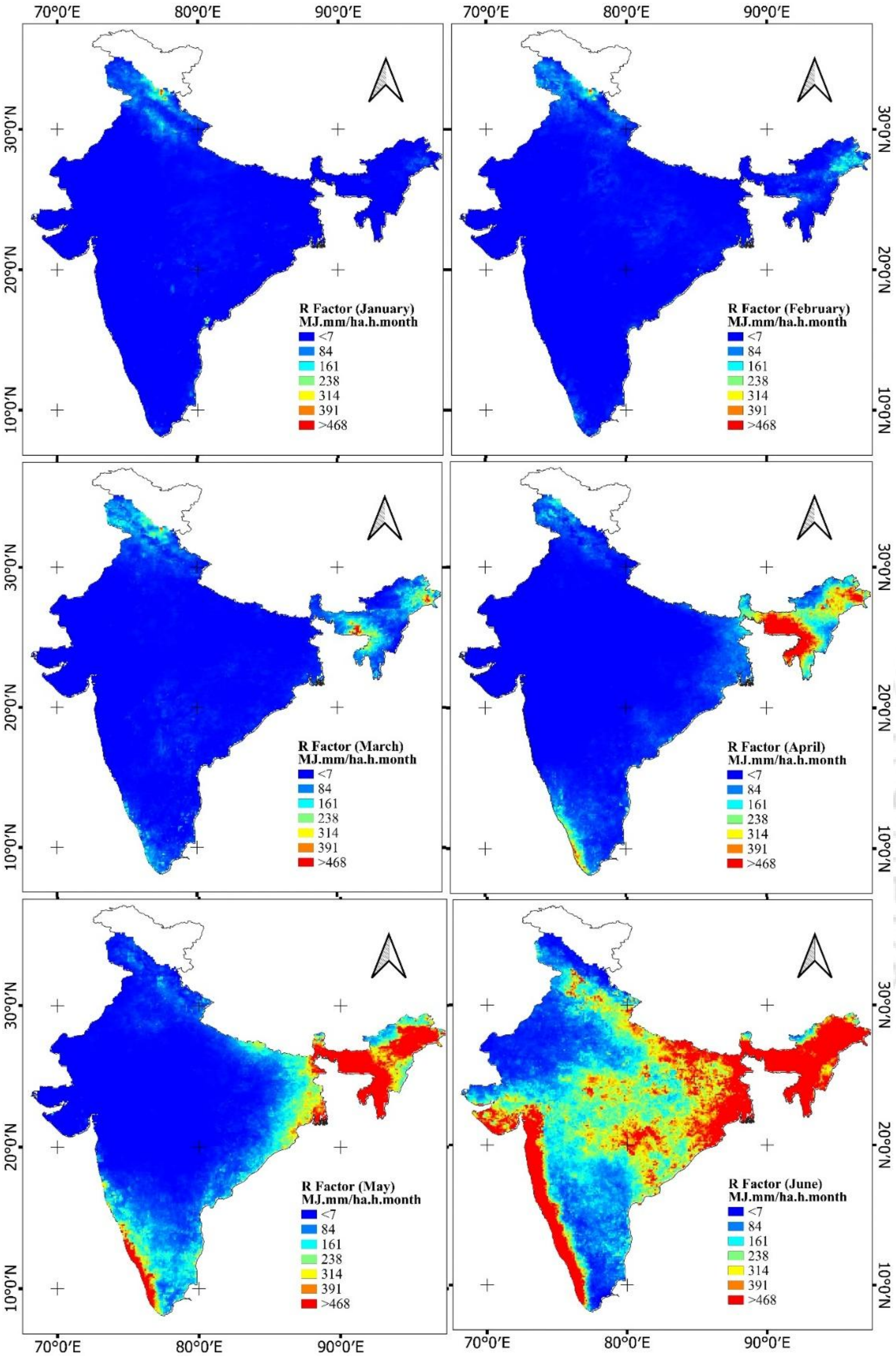

Figure 3.11 Spatial distribution of average monthly rainfall erosivity factor for the months January to June

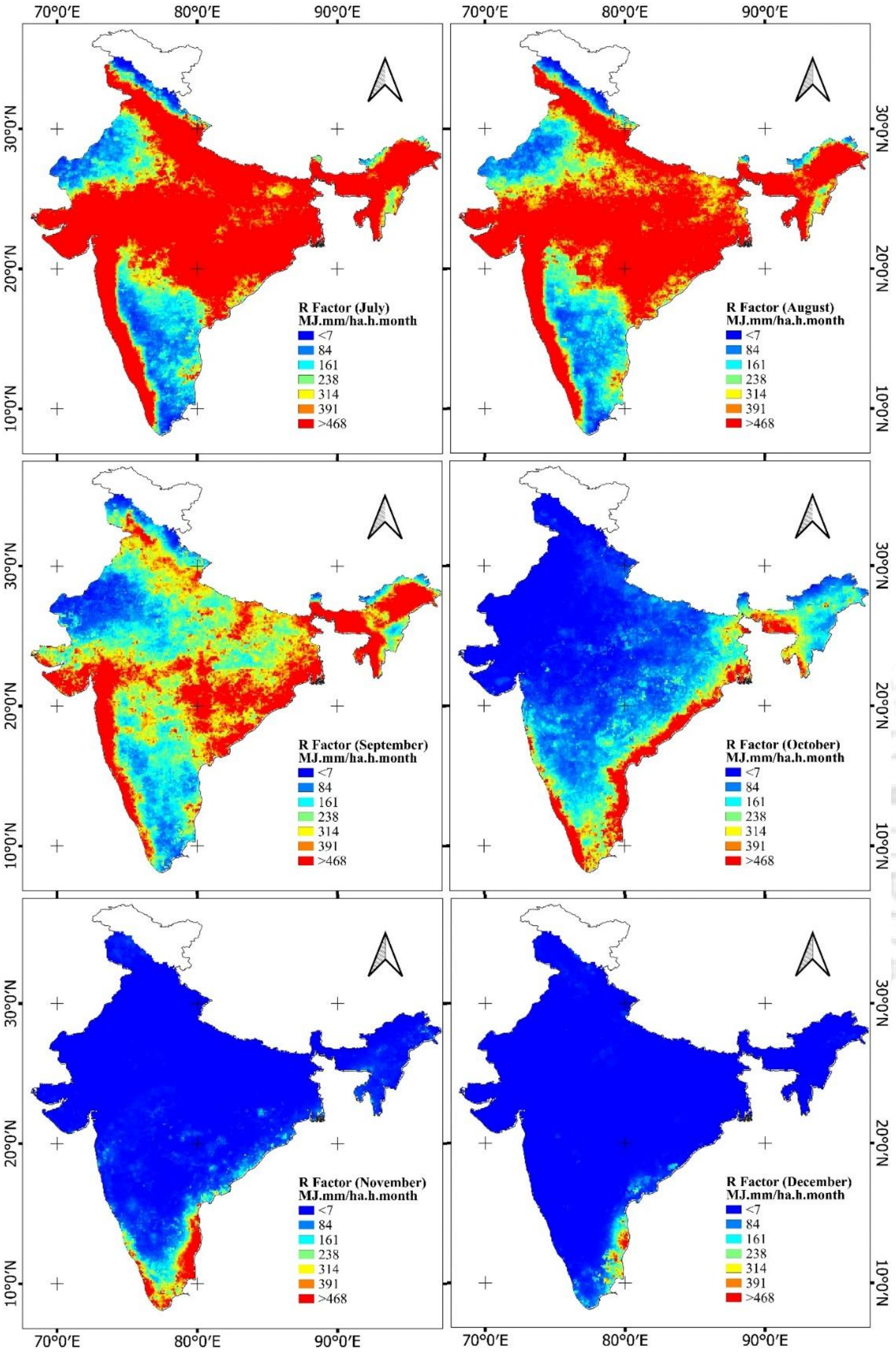

Figure 3.12 Spatial distribution of average monthly rainfall erosivity factor for the months July to December

The Northeast Monsoon, occurring in November and December, shifts erosivity hotspots toward the coastal regions of Tamil Nadu, Andhra Pradesh, and Kerala. During these months, erosivity is negligible across the rest of India due to the absence of rainfall. This monthly variation underscores the dynamic nature of rainfall erosivity in India. The erosivity hotspots shift spatially across the subcontinent depending on the prevailing monsoon system, highlighting the need to assess R factor at a monthly scale rather than relying solely on annual averages. The annual mean erosivity gives an average perspective, which masks the intra annual and seasonal variability. A monthly assessment offers deeper insights into the spatiotemporal transformations of erosivity. The spatial distribution of average monthly rainfall erosivity factor for the months January to June is presented in Figure 3.11 and July to December presented in Figure 3.12 respectively.

3.3.4 Seasonal variation of Rainfall Erosivity Factor

The seasonal assessment of rainfall erosivity (R factor) provides a broader understanding of its spatial dynamics across India by aligning with the classification of the India Meteorological Department (IMD), which subdivides the year into four distinct rainfall seasons: Winter (January–February), Pre-Monsoon (March–May), Southwest Monsoon (June–September), and Post-Monsoon/Northeast Monsoon (October–December). The spatial variation of erosivity across these four seasons is presented in Figure 3.13.

During the Winter season, rainfall activity is minimal across most parts of the country, resulting in uniformly low R factor values. Only some areas in North East India and Himachal Pradesh exhibit detectable erosivity. In contrast, the Pre-Monsoon season marks the initiation of high erosivity. Some elevated values can be seen in North East India as well as along the coastal fringes of Karnataka and Kerala within the Western Ghats.

The Southwest Monsoon season represents the peak phase of erosivity both in magnitude and spatial coverage. During this period, most areas of the country is characterized by high R factor values, underscoring the erosive potential of the intense monsoon rains. Nevertheless, certain regions such as Tamil Nadu, Karnataka, Andhra Pradesh, and Rajasthan exhibit comparatively low erosivity. It is observed that although North East India generally experiences consistently high values, the westernmost part of Arunachal Pradesh shows relatively lower erosivity.

In the Post-Monsoon/Northeast Monsoon season, erosivity hotspots shift towards the coastal regions of Tamil Nadu, Andhra Pradesh, and Kerala, driven by the influence of the Northeast Monsoon. The rest of the country records negligible values as rainfall subsides after the withdrawal of the Southwest Monsoon. This seasonal perspective demonstrates how the erosivity hotspots migrate across the country in response to the shifting monsoon systems of India.

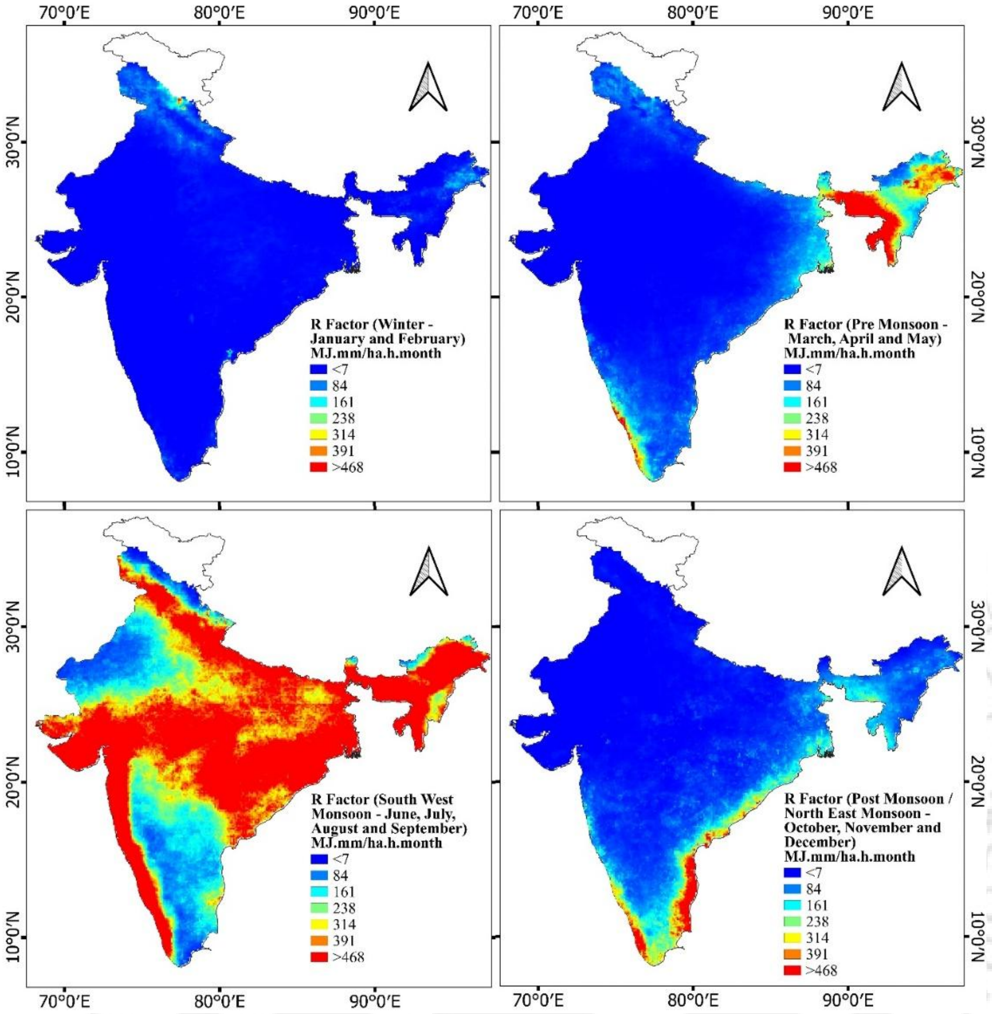

Figure 3.13 Seasonal variation of Rainfall Erosivity Factor

3.3.5 Annual variation of Rainfall Erosivity Factor

A consistent spatial pattern is observed throughout the study period (Figure 3.14), with the highest R factor values concentrated along the Western Ghats, Northeastern states, and parts of the Himalayan foothills. These regions are characterized by high-intensity monsoon rainfall, which contributes to elevated rainfall erosivity. The western ghat and the northeastern hilly terrains consistently exhibit high R factor values. In contrast, the central and western regions of India mostly display low R factor values. These regions experience arid to semi-arid climate conditions with relatively lower rainfall intensity. Thus, it contributes minimally to erosivity. The spatial distribution pattern remains broadly stable across the years with presence of some inter-annual variabilities. The temporal analysis reveals, the general spatial pattern remains stable but the magnitude of

R factor exhibits variability. There is no consistent long-term increasing or decreasing trend in R factor can be found across the study period.

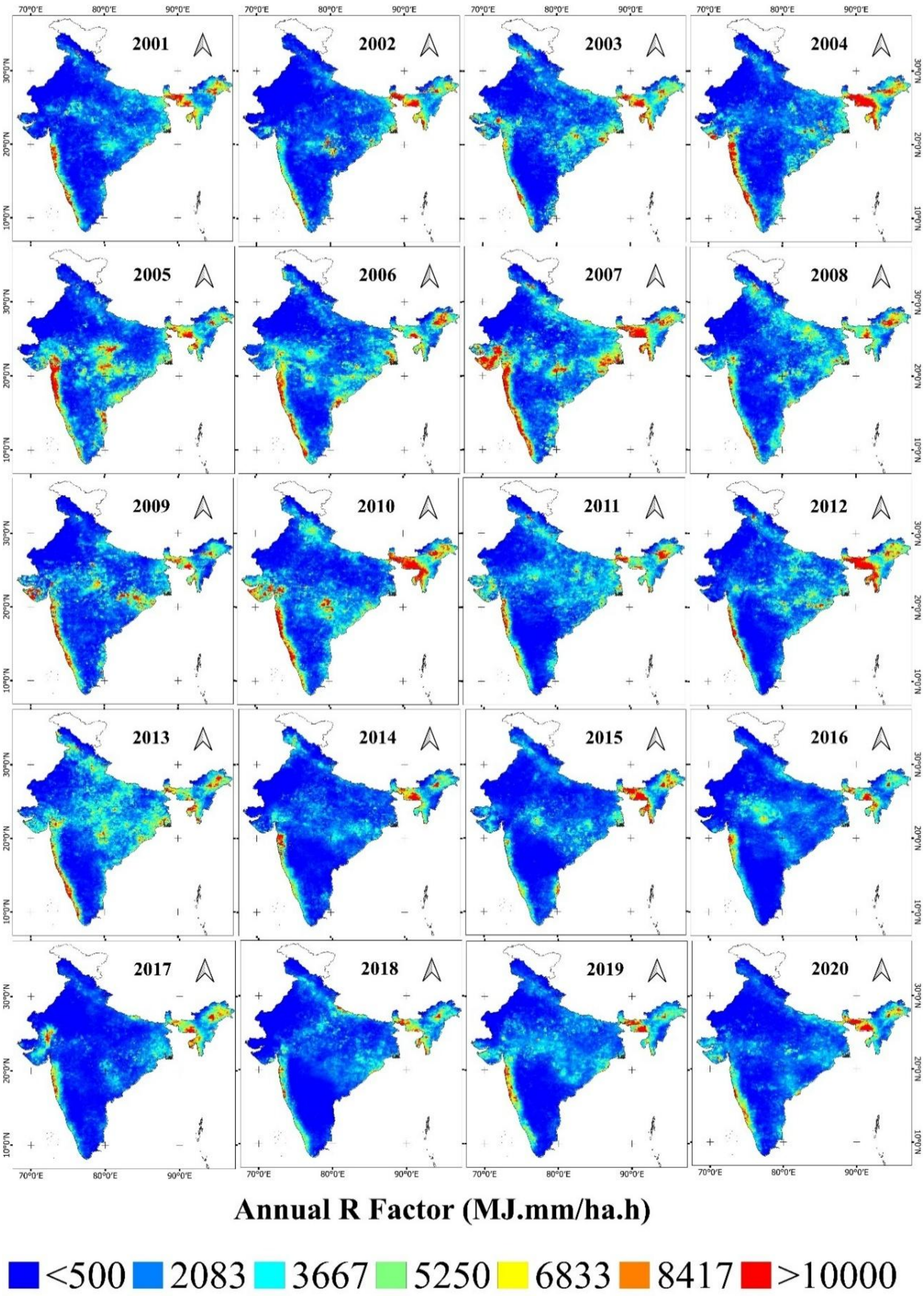

Figure 3.14 Spatial distribution of annual rainfall erosivity factor for 20 years over the study area

The temporal evolution of the average annual R factor over the study period (2001–2020) is presented in Figure 3.15. The graph depicts the inter annual variability of the R factor, along with the linear trend and the long-term average value. The average annual R factor exhibits substantial fluctuations throughout the study period. The highest peak is observed in 2007, where the R factor reached values close to 3100 MJ.mm/ha.h, significantly exceeding the long-term average. This peak corresponds to an exceptionally intense monsoon year associated with extreme rainfall events that contributed to higher erosivity values. A general declining trend is observed in the annual R factor after 2007 peak with some occasional increases in years 2011 and 2013. The overall temporal trend indicates a gradual decrease in the average annual R factor over the 20-year period. This decreasing trend suggests a minor reduction in erosivity, which could be attributed to several factors such as changes in large-scale climate patterns, variations in monsoon intensity etc.

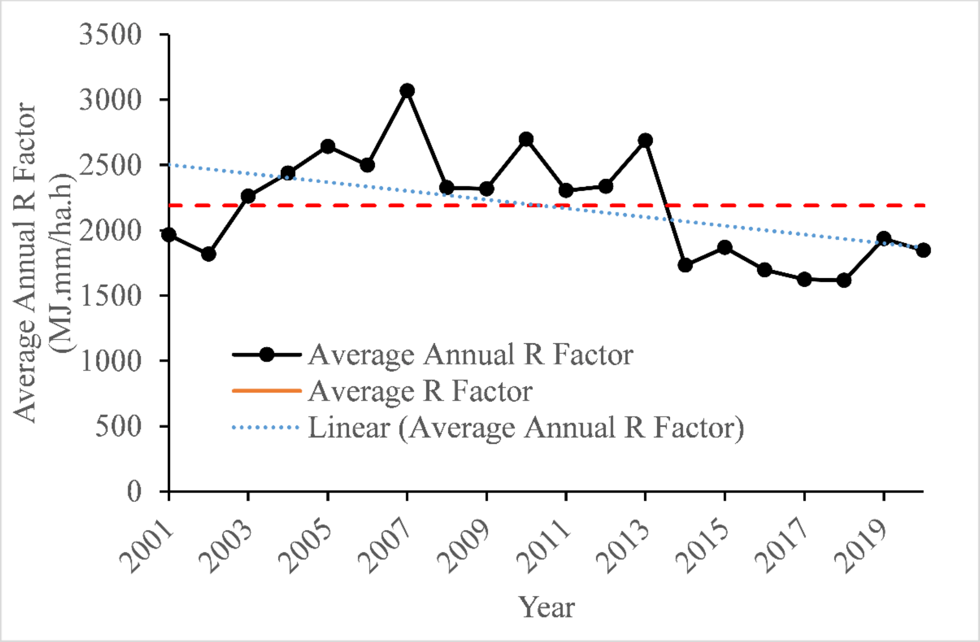

Figure 3.15 Temporal variation of average annual rainfall erosivity factor for 20 years

3.3.6 Trend Analysis of Annual Rainfall Erosivity Factor

The application of the Modified Mann Kendall test to assess temporal trends in the rainfall erosivity factor across India reveals diverse spatial patterns in both the direction and significance of changes. The analysis indicates that approximately 12.04% of the study area exhibits a significant decreasing trend, whereas only 1.82% shows a significant increasing trend. Thus, only 13.86% of the area collectively demonstrates a statistically significant trends. Around 55.84% of the country exhibits a non-significant decreasing trend and 30.29% shows a non-significant increasing trend.

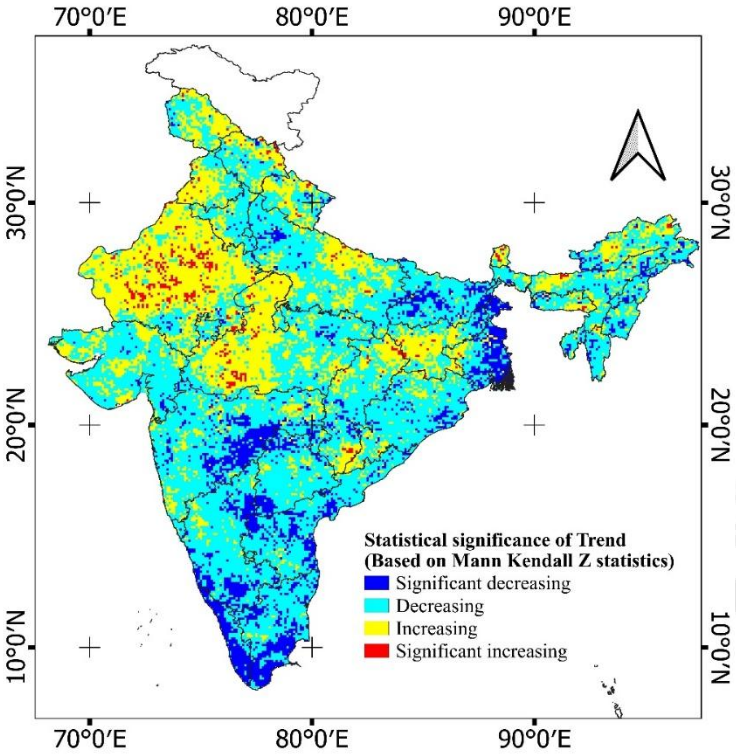

Figure 3.16 Statistically significant (0.05 significance level) Modified Mann-Kendall trend results using annual R factor values for all grid points covered by IMERG over the study area during the time period 2001 to 2020

The Figure 3.16 highlights that regions with significant increasing trends are primarily concentrated in Rajasthan, with minor occurrences in North East India, Madhya Pradesh, Himachal Pradesh and Uttarakhand. Interestingly, although the number of locations with increasing trends is greatest in Rajasthan, the magnitude of increase, as estimated by Sen's slope, is higher in the North East India, particularly in Assam, where the maximum slope reaches 397 MJ.mm/ha.h.year (Figure 3.17). This observation emphasizes the critical distinction between trend occurrence and trend intensity.

Non-significant increasing trends are predominantly observed in the northwestern part of India, whereas the remaining parts of the country largely show non-significant decreasing trends. The significant decreasing trends are primarily concentrated in the southern Indian states, West Bengal, and Maharashtra. It is important to note that trend direction alone does not fully capture the potential impact of rainfall erosivity. For instance, Rajasthan, despite exhibiting several increasing trends, maintains a consistently low R factor across all years and months (Figure 3.11,Figure 3.12 and Figure 3.14) , indicating that the erosivity magnitude can be remain limited even in the presence of an upward trend.

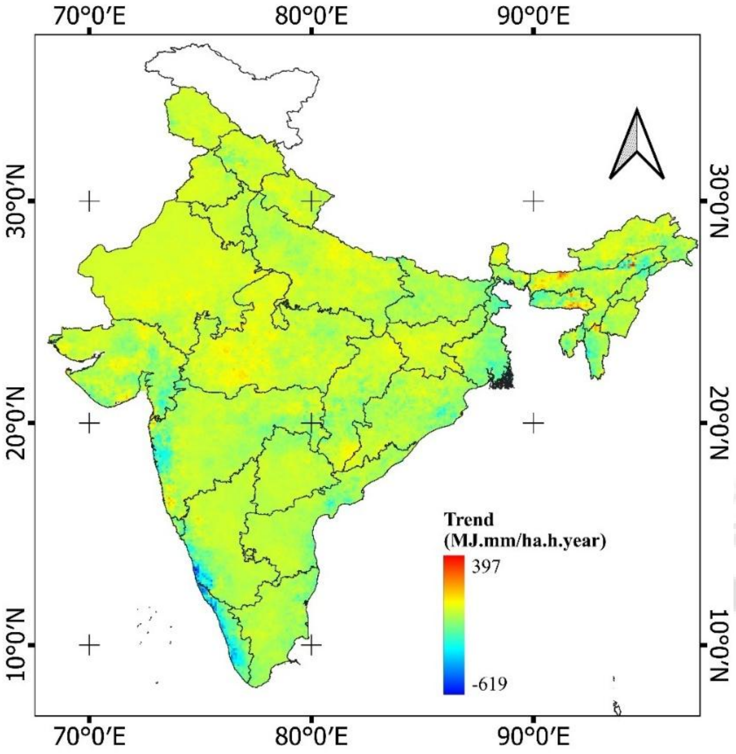

Figure 3.17 Spatial distribution of strength or magnitude of trend in terms of sens's slope (MJ.mm/ha.h.year)

In a global scale study, Bezak et al. (2022) applied the Mann Kendall test to annual R factor data derived from CMORPH satellite precipitation and reported that only 15% of global areas exhibited significant trends, while the majority, 85%, did not demonstrate any discernible trend. Similarly, for India, approximately 87% of the country's area shows no significant change in the annual R factor, confirming that the dominant pattern across most regions is statistical stability.

3.3.7 Sensitivity Analysis of Rainfall Erosivity Factor

The Table 3.1 illustrates the percentage variation of the R factor for all agro-climatic zones in response to these percentage errors in rainfall intensity. It can be observed that the percentage variation of the R factor is similar across all zones, except for the 50% and 100% changes. The variation ranges from 67.05% to 71.08% for a 50% change in rainfall intensity, and from 138.08% to 149.85% for a 100% change. The average percentage variations in the R factor for -50%, -20%, -10%, -5%, 5%, 10%, 20%, 50%, and 100% changes in rainfall intensity were found to be -59.56%, -25.34%, -12.89%, -6.49%, 6.59%, 13.27%, 27.87%, 69.42%, and 144.7%, respectively, as shown in Figure 3.18.

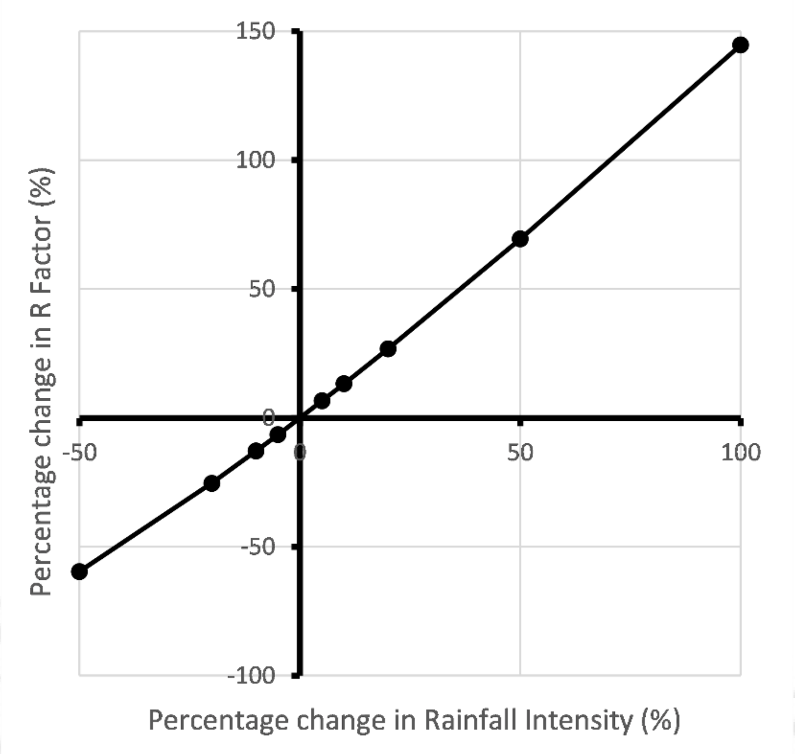

Figure 3.18 Average percentage change in R factor with respect to the change in percentage of rainfall intensity for the points considered in this study from all the agro-climatic zones

Table 3.1 The percentage variation of R factor for all the agro climatic zones with respect to the error percentages of rainfall intensity considered in the study

Error %	**ACZ_1**	**ACZ_2**	**ACZ_3**	**ACZ_4**	**ACZ_5**	**ACZ_6**	**ACZ_7**	**ACZ_8**	**ACZ_9**	**ACZ_10**	**ACZ_11**	**ACZ_12**	**ACZ_13**	**ACZ_14**
-50	-59.81	-59.84	-59.54	-59.3	-59.69	-59.85	-59.39	-59.57	-59.41	-59.43	-59.58	-59.37	-59.42	-59.65
-20	-25.62	-25.54	-25.15	-25.16	-25.29	-25.63	-25.07	-25.18	-25.47	-25.48	-25.5	-25.21	-25.03	-25.51
-10	-13.05	-12.99	-12.75	-12.78	-12.84	-13.06	-12.71	-12.77	-12.98	-12.99	-12.99	-12.81	-12.68	-12.99
-5	-6.58	-6.55	-6.42	-6.44	-6.46	-6.59	-6.4	-6.43	-6.55	-6.55	-6.55	-6.46	-6.38	-6.55
5	6.69	6.65	6.49	6.53	6.55	6.69	6.47	6.51	6.67	6.67	6.66	6.55	6.45	6.66
10	13.49	13.4	13.06	13.14	13.17	13.49	13.02	13.08	13.44	13.44	13.42	13.18	12.97	13.42
20	27.37	27.15	26.38	26.6	26.64	27.38	26.31	26.44	27.3	27.31	27.23	26.7	26.18	27.22
50	71.01	70.24	67.66	68.6	68.49	71.04	67.55	67.86	71.08	71.08	70.67	68.96	67.05	70.58
100	148.8	146.58	139.59	142.77	141.76	148.92	139.6	140.17	149.85	149.8	148.22	143.79	138.08	147.87

3.4 Conclusion

An approach was used to incorporate high temporal resolution satellite rainfall data for the computation and generation of R factor map of India. The study also presents an extensive analysis of the spatiotemporal variation of the R factor across India with detailed insights into its dynamic behaviour over different regions and time periods. This approach eliminated the reliance on interpolation methods, enabling the generation of a continuous and high-resolution R factor map.

The overall spatial average of the R factor across India was estimated to be 2188.79 MJ.mm/ha.h.year, with values ranging from a minimum of 68.28 MJ.mm/ha.h.year to a maximum of 18,864.2 MJ.mm/ha.h.year. The major rainfall erosivity hotspots in the country were identified as the North-Eastern region of India and the Western Ghats. The comparison with the Panagos et al. (2017) global ground-based R factor map revealed that the IMERG based mean R factor was approximately 58% of the ground-based mean during the common period (2007–2015). The study was further validated against the historical Isoerodent map of India developed by Babu et al. (1978). Although significant discrepancies were observed in the magnitude of the R factor, the spatial distribution patterns showed a reasonable degree of alignment with the IMERG based R factor map. A station-level comparison with an IMD rain gauge station demonstrated that the IMERG based average R factor was approximately 10% higher than the observed IMD gauge value.

A non-dimensional R factor map was developed by normalizing the computed R factor values relative to the spatial mean to give a generalized perspective. The results indicated that 63.48% of the area exhibited values below the mean. The monthly analysis of the R factor revealed clear spatiotemporal variations. The values were lowest in January and February, gradually increasing during the Pre-Monsoon period (March–May). The Southwest Monsoon (June–September) represented the peak erosive phase with the majority of annual rainfall erosivity values. In contrast, erosivity hotspots shifted towards the South Indian coast under the influence of the Northeast Monsoon during the post-monsoon months (October–December). While the spatial pattern of R factor remained broadly stable, a significant inter-annual variability was observed in the long term (2001-2020). A slight overall decreasing trend in the average annual R factor was also observed. The application of the Modified Mann-Kendall test for trend analysis revealed that only

13.86% of the study area showed statistically significant trends, out of which 12.04% significant decrease and 1.82% significant increase.

The spatially distributed R factor map helps the preliminary identification of vulnerable areas to rainfall induced soil erosion and facilitates the analysis of its spatiotemporal variability. These results provide a solid basis for regional erosion risk assessment and improving the accuracy of soil loss modelling.

Chapter 4

Incorporating return period in the assessment of rainfall erosivity factor over India

4.1 Introduction

The concept of return period is a fundamental tool in hydrology, climatology and risk management. It is widely used in assessing the likelihood of extreme events such as floods, droughts, storms or intense rainfall. Return period provides a probabilistic measure of how often an event of a given magnitude can be expected to occur. The return period is defined as the average time interval between the occurrences of an event of equal or greater magnitude. For example, a 100 year flood refers to a flood event that has a 1% probability of occurring in any given year. Return period is a critical concept that links probability theory with real-world risk assessment. Return period provides flexibility to policymakers, planners and engineers in choosing appropriate safety margins based on the criticality of infrastructure.

The analysis of return periods in rainfall erosivity studies is of great importance. The rainfall erosivity factor (R factor) plays a key role in estimating soil loss, which is a crucial input for the design of soil conservation structures. Traditionally, the R factor represents the mean annual value and the soil loss computed is also become an average annual estimate. However, relying only on the average annual soil loss has certain limitations. The use of average values can be misleading in regions with high variability in annual rainfall. It often results in an overestimation of soil loss during dry years and an underestimation during wet years (Mannaerts and Gabriels, 2000; Pampalone and Ferro, 2020).

This chapter focuses on incorporating the concept of return period into the computation of the Rainfall Erosivity Factor. To achieve this, the standard procedure of frequency analysis will be combined with the R factor calculation method from the RUSLE handbook, to estimate and map the rainfall erosivity factor for various return periods using high spatiotemporal resolution precipitation products. The 0.1 degree half hourly IMERG precipitation data will utilized to generate the rainfall erosivity map of India for different return periods. A spatially distributed map of best-fitted distribution will also be prepared, and this knowledge will be instrumental in computing the rainfall erosivity factor for a return period in a location.

4.2 Materials and methodology

4.2.1 Study Area and data used

The study area and data used are same as the Chapter 3.

4.2.2 Annual Rainfall erosivity factor

The return period analysis will be performed with the help of twenty years (2001 to 2020) annual rainfall erosivity factor of each grid point of IMERG 0.1 degree satellite precipitation data all over the India except Ladakh and the Island union territory. The expression for Annual Rainfall Erosivity Factor will be,

$$\text{Annual Rainfall Erosivity Factor} = \sum_{i=1}^{j}(\mathrm{EI}_{30})_i \tag{4.1}$$

where $(\mathrm{EI}_{30})_i$ denotes the EI_{30} for rainfall event i and j represents the number of rainfall events in a year.

$$\text{Annual Average R factor or R Factor} = \frac{\sum_{i=1}^{N}(\text{Annual Rainfall erosivity factor})}{Number\ of\ years\ (N)} \tag{4.2}$$

In the calculation of R factor, all the rainfall events are not considered. The rainfall events having erosive capacity are only considered as per RUSLE guidebook (Renard et al., 1997).

4.2.3 Fitting Probability Distribution

In this study, twelve theoretical probability distributions are considered, which are widely used in various hydrological frequency analysis (Aronica and Ferro 1997; Bagarello et al. 2010; Taguas et al. 2011; Nazzareno and Bellocchi 2014; Hamidreza and Mohsen 2017). The maximum likelihood estimation was employed to determine the parameters for various distributions. The maximum likelihood estimation method is usually consistent, unbiased, normally distributed and efficient even if the number of sample data increases to infinity. This is why the maximum likelihood estimation is very popular and widely used (Heumann and Shalabh, 2016). The distributions used in this study are Generalized Extreme Value, Weibull min, Normal, Gamma, Lognormal, Gumbel Right Skewed, Gumbel left skewed, Beta, Pareto, Double gamma, Pearson type 3 and Exponential.

4.2.3.1 Generalized Extreme Value

The parameters of Generalized Extreme Value distribution are k= shape, σ= scale (σ>0) and μ= location. The domain of the distribution is $1 + k\frac{(x-\mu)}{\sigma} > 0\ for\ k \neq 0\ and\ -\infty < x < +\infty\ for\ k = 0$.

The Probability Density Function $f(x)$ and the cumulative distribution functions $F(x)$ are

$$f(x) = \frac{1}{\sigma}\exp\left(-(1+kz)^{\frac{-1}{k}}\right)(1+kz)^{-1-\frac{1}{k}} \quad for\ k \neq 0$$

$$f(x) = \frac{1}{\sigma}\exp(-z - exp(-z))\ for\ \ k = 0$$

$$F(x) = \exp\left(-(1+kz)^{-\frac{1}{k}}\right) \quad for\ k \neq 0$$

$$F(x) = \exp(-\,exp(-z)) \quad for\ k = 0$$

where, $z = \frac{x-\mu}{\sigma}$

4.2.3.2 Weibull_min

The parameters of Weibull_min distribution are α = shape ($\alpha > 0$), β = scale ($\beta = 1$) and γ = location ($\gamma = 0$).

The Probability Density Function $f(x)$ and the cumulative distribution functions $F(x)$ are

$$f(x) = \frac{\alpha}{\beta}\left(\frac{x-\gamma}{\beta}\right)^{\alpha-1}\exp\left(-\left(\frac{x-\gamma}{\beta}\right)^{\alpha}\right)$$

$$F(x) = 1 - \exp\left(-\left(\frac{x-\gamma}{\beta}\right)^{\alpha}\right)$$

4.2.3.3 Normal

The parameters of Normal distribution are σ= scale (σ>0) and μ= location. The domain of the distribution is $-\infty < x < +\infty$.

The Probability Density Function $f(x)$ and the cumulative distribution functions $F(x)$ are

$$f(x) = \frac{\exp\left(-\frac{1}{2}\left(\frac{x-\mu}{\sigma}\right)^2\right)}{\sigma\sqrt{2\pi}}$$

$$F(x) = \Phi\left(\frac{x-\mu}{\sigma}\right)$$

where, Φ is the Laplace Integral, $\Phi(x) = \frac{1}{2\pi}\int_0^x e^{-\frac{t^2}{2}}dt$

4.2.3.4 Gamma

The parameters of Gamma distribution are α= shape (α>0), β= scale (β>0) and γ= location. The domain of the distribution is $\gamma \leq x < +\infty$.

The Probability Density Function $f(x)$ and the cumulative distribution functions $F(x)$ are

$$f(x) = \frac{x^{\alpha-1}}{\beta^{\alpha}\Gamma(\alpha)}\exp\left(-\frac{x}{\beta}\right)$$

$$F(x) = \frac{\Gamma_{\frac{x}{\beta}}(\alpha)}{\Gamma(\alpha)}$$

Γ is the Gamma Function and Γ_z is the Incomplete Gamma Function

$$\Gamma(\alpha) = \int_0^{\infty} t^{\alpha-1}e^{-t}dt \qquad (\alpha > 0)$$

$$\Gamma_z(\alpha) = \int_0^{z} t^{\alpha-1}e^{-t}dt \qquad (\alpha > 0)$$

Γ is the Gamma Function and Γ_z is the Incomplete Gamma Function

4.2.3.5 Log Normal

The parameters of Log Normal distribution are σ= scale (σ>0), μ= shape and γ= location. The domain of the distribution is $\gamma < x < +\infty$.

The Probability Density Function $f(x)$ and the cumulative distribution functions $F(x)$ are

$$f(x) = \frac{\exp\left(-\frac{1}{2}\left(\frac{\ln(x-\gamma)-\mu}{\sigma}\right)^2\right)}{(x-\gamma)\sigma\sqrt{2\pi}}$$

$$F(x) = \Phi\left(\frac{\ln(x-\gamma)-\mu}{\sigma}\right)$$

where, Φ is the Laplace Integral, $\Phi(x) = \frac{1}{2\pi}\int_0^x e^{-\frac{t^2}{2}}dt$

4.2.3.6 Gumbel right skewed

The parameters of Gumbel Max distribution are σ= scale (σ>0) and μ= location. The domain of the distribution is $-\infty < x < +\infty$.

The Probability Density Function $f(x)$ and the cumulative distribution functions $F(x)$ are

$$f(x) = \frac{1}{\sigma}\exp\left(-z-\exp(-z)\right)$$

$$F(x) = \exp\left(-\exp(-z)\right)$$

where, $z = \frac{x-\mu}{\sigma}$

4.2.3.7 Gumbel left skewed

The parameters of Gumbel Min distribution are σ= scale (σ>0) and μ= location. The domain of the distribution is $-\infty < x < +\infty$.

The Probability Density Function $f(x)$ and the cumulative distribution functions $F(x)$ are

$$f(x) = \frac{1}{\sigma} \exp\,(z - \exp(z))$$

$$F(x) = 1 - \exp\,(-\exp(z))$$

where, $z = \frac{x-\mu}{\sigma}$

4.2.3.8 Beta

The Probability Density Function $f(x)$ and the cumulative distribution functions $F(x)$ are

$$f(x, a, b) = \frac{\Gamma(a+b)x^{a-1}(1-x)^{b-1}}{\Gamma(a)\Gamma(b)} = \frac{1}{B(a,b)}\ x^{a-1}(1-x)^{b-1}$$

here $a\ and\ b$ are shape parameter, $a, b > 0$, $\Gamma\ (z)$ is the gamma function and $B(a, b)$ is the Beta function.

$$F(x; a, b) = \frac{B\ (x;a,b)}{B\ (a,b)} = I_x(a, b)$$

here $B\ (x; a, b)$ is the incomplete beta function and $I_x(a, b)$ is the regularized incomplete beta function.

4.2.3.9 Pareto

The parameters of Pareto distribution are α = shape parameter (α >0) and β = scale parameter ($\beta >$ 0). The domain is $\beta \leq x < +\infty$.

The Probability Density Function $f(x)$ and the cumulative distribution functions $F(x)$ are

$$f(x) = \frac{\alpha\beta^{\alpha}}{x^{\alpha+1}}$$

$$F(x) = 1 - \left(\frac{\beta}{x}\right)^{\alpha}$$

4.2.3.10 Double Gamma

The parameters of Double Gamma distribution is α = shape parameter ($\alpha > 0$) and it applies for all real x.

The Probability Density Function $f(x)$ and the cumulative distribution functions $F(x)$ are

$$f(x) = \frac{1}{2\Gamma(\alpha)}|x|^{\alpha-1}e^{-|x|}$$

$$F(x) = \begin{cases} \frac{1}{2} - \frac{1}{2\Gamma(\alpha)}\gamma(\alpha, |x|) & x \leq 0 \\ \frac{1}{2} + \frac{1}{2\Gamma(\alpha)}\gamma(\alpha, |x|) & x > 0 \end{cases}$$

here $\gamma(\alpha, z)$ is the lower incomplete gamma function.

4.2.3.11 Pearson type 3

The Probability Density Function $f(x)$ and the cumulative distribution functions $F(x)$ are

$$f(x) = \frac{x-\gamma^{\alpha-1}}{\beta^{\alpha}.\Gamma\alpha}.e^{-\frac{x-\gamma}{\beta}}$$

$$F(x) = 1 - \frac{1}{\beta.\Gamma(\alpha)}.\int_{\gamma}^{x}\frac{x-\gamma^{\alpha-1}}{\beta}.e^{-\frac{x-\gamma}{\beta}}dx = \frac{\Gamma(\alpha),\frac{x-\gamma}{\beta}}{\Gamma(\alpha)}$$

where, α, β, γ are the shape, scale and location parameters and $\gamma < x < \infty$ if $\beta > 0$ or $-\infty < x < \gamma$ if $\beta < 0$ and $\alpha > 0$

4.2.3.12 Exponential

The probability density function $f(x;\ \lambda)$ and cumulative distribution function $F(x;\ \lambda)$ of an exponential distribution are

$$f(x;\ \lambda) = \begin{cases} \lambda e^{-\lambda x} & x \geq 0 \\ 0 & x < 0 \end{cases}$$

$$F(x;\ \lambda) = \begin{cases} 1 - e^{-\lambda x} & x \geq 0 \\ 0 & x < 0 \end{cases}$$

here $\lambda > 0$ is the parameter of the distribution, called as rate parameter and scale $= \frac{1}{\lambda}$. The distribution is supported on the interval [0, ∞).

4.2.4 Goodness of fit test

The goodness of fit of a distribution refers to the extent to which it accurately matches the frequency distribution curve of observations of the sample dataset. Here, the goodness of fit of distributions was evaluated with one commonly used empirical distribution function (EDF) test namely Kolmogorov-Smirnov Test (Rahman et al. 2013; Alam et al. 2018). The Kolmogorov-Smirnov test measures the degree of difference between the empirical distribution function observed in a specific sample and the CDF associated with that distribution under examination.

The Kolmogorov-Smirnov test statistics can be given by

$$D = \max_{1\le i\le N}\left(F(Y_i) - \frac{i-1}{N}, \frac{i}{N} - F(Y_i)\right) \tag{4.3}$$

F represents the theoretical cumulative distribution of the distribution under examination, which is required to be a continuous distribution.

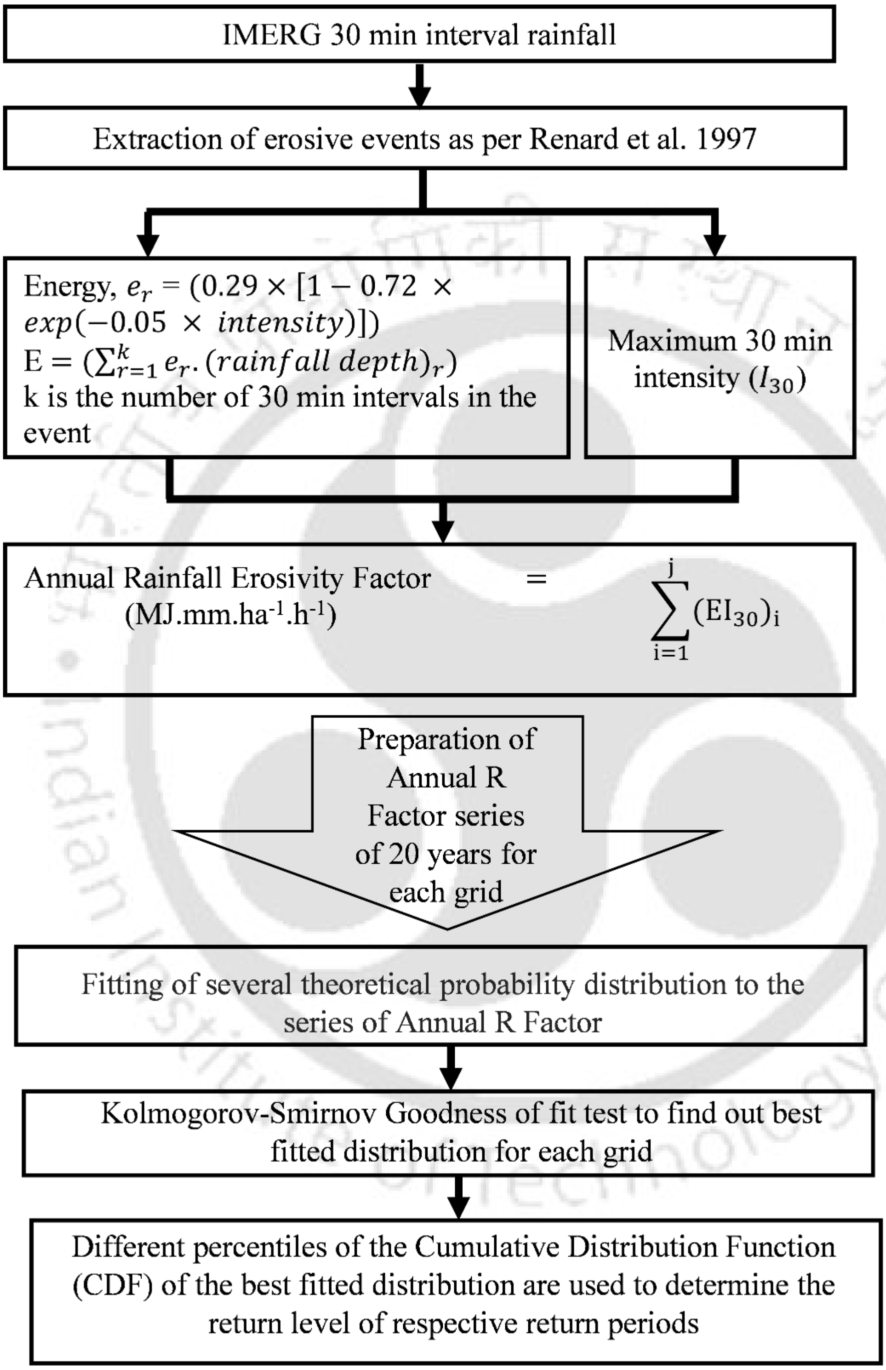

Figure 4.1 Flow chart of return period analysis of R factor

In this study, a significance level (α) of 0.05 has been used. In a Kolmogorov-Smirnov (KS) test, a significance level of 0.05 indicates that the null hypothesis is rejected when the chance of witnessing the test statistic, assuming the null hypothesis to be true, is equal to or less than 0.05. The two distributions (a sample distribution and a theoretical distribution) under comparison must be identical, according to the KS test's null hypothesis.

4.2.5 Return Period

When the Annual R factor (x) value equals or exceeds a X_T magnitude event, which is happened only one time in T number of years, then the probability of occurrence P $(x \geq X_T)$ is given by

$$P(x \geq X_T) = \frac{1}{T} \qquad => T = \frac{1}{P(x \geq X_T)} \qquad =>T = \frac{1}{1-P(x \leq X_T)} \tag{4.4}$$

The hydrological parameter related with a return period of a larger number of years cannot be directly estimated from a dataset of a smaller number of sample data. So, the value corresponding to those return periods can be extracted from the various percentiles of CDF of a fitted distribution. For example, if we need a return level of the hydrological parameter for 50 years return period, then we use the 98 percentile value as $1/(1-0.98^{-year})$=50 years, similarly for 100 years return period, we use the 99 percentile value as $1/(1-0.99^{-year})$=100 years and so on (Alam et al., 2018; Wilks, 1993). The whole process of incorporation of return period analysis in rainfall erosivity factor is presented in the flow chart as shown in Figure 4.1.

4.3 Result and discussion

4.3.1 Best fitted Theoretical Probability Distribution of Annual R Factor

Twelve numbers of theoretical probability distributions were fitted in the annual R factor data series, and best-fitted distribution was evaluated by using the Kolmogorov-Smirnov goodness of fit test at each grid point of the data series. Figure 4.2 presents the spatial distribution of the best-fitted distribution. The spatially distributed map of the best-fitted distribution of the Annual R factor can be a tool to determine the R factor corresponding to various return periods in a location. The map will provide the best-fitted distribution at $0.1^{o} \times 0.1^{o}$ spatial resolution for the study area. It can be observed from Figure 4.3 that the Lognormal probability distribution is the best-fitted distribution in the highest number of grid points, and Pearson type 3 is the best-fitted distribution in the second-highest number of grid points, and Exponential is the best-fitted distribution in the least number of grid points. Ferro et al. (1999) used Lognormal and Gumbel probability distribution to fit Annual R factor data in Italy and found adequate fitting for their data. Sadeghi et al.

(2017) also found Lognormal distribution as the best-fitted distribution in most of the stations of Iran on an annual scale.

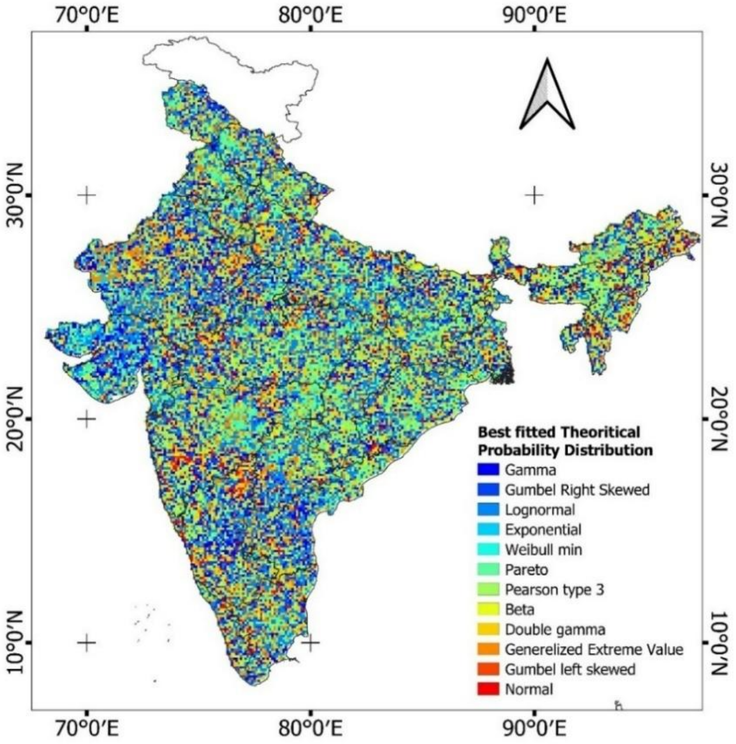

Figure 4.2 Spatial distribution of best fitted distribution of Annual R factor of the study area

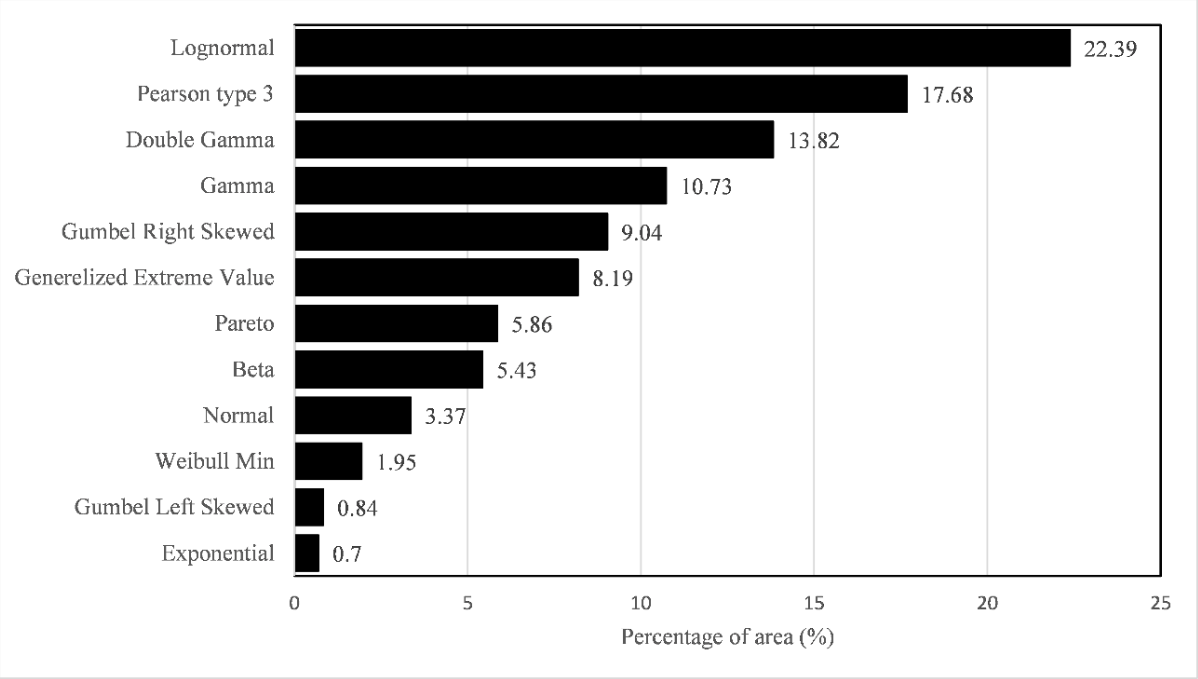

Figure 4.3 Percentage of area under each best fitted probability distribution

4.3.2 Annual variability of R factor corresponding to different return period

This study was performed to enhance the analysis of the R factor in India by incorporating return period analysis. To achieve this objective, we conducted a return period analysis using the Annual R factor values obtained from all grid points. Subsequently, we generated return level maps for the 2, 5, 10, 25, 50, and 100 year return periods.

Figure 4.4 displays the return period maps, revealing a consistent spatial pattern across all return periods that closely resembles the spatial distribution pattern of the average annual R factor. As observed in the average annual R factor map, higher values are predominantly concentrated in certain regions of North East India and the Western Ghats. Notably, the Kangra District of Himachal Pradesh exhibits significantly higher values for higher return periods, coinciding with elevated values of the average annual R factor in the same area. A similar observation can be made in the Lower Subansiri District of Arunachal Pradesh, where higher values are also evident for higher return periods.

Overall, the average R factor values for India across the 2, 5, 10, 25, 50, and 100-year return periods are 1918.94, 2963.84, 3795.55, 4916.79, 5487.89, and 5806.90 MJ.mm.ha^{-1}h^{-1} respectively. Additionally, the maximum values of the Annual R factor for India are 18,556.12, 25,598.15, 35,815.77, 46,113.28, 49,545.78, and 51,262.03 MJ.mm.ha^{-1}h^{-1} for the 2, 5, 10, 25, 50, and 100-year return periods, respectively. It is worth noting that the maximum Annual R Factor corresponding to all return periods, except the 5-year return period, are concentrated in a specific location within the West Khasi Hill district of Meghalaya. However, the maximum Annual R Factor corresponding to the 5-year return period is found in a different location within the Lakhimpur District of Assam.

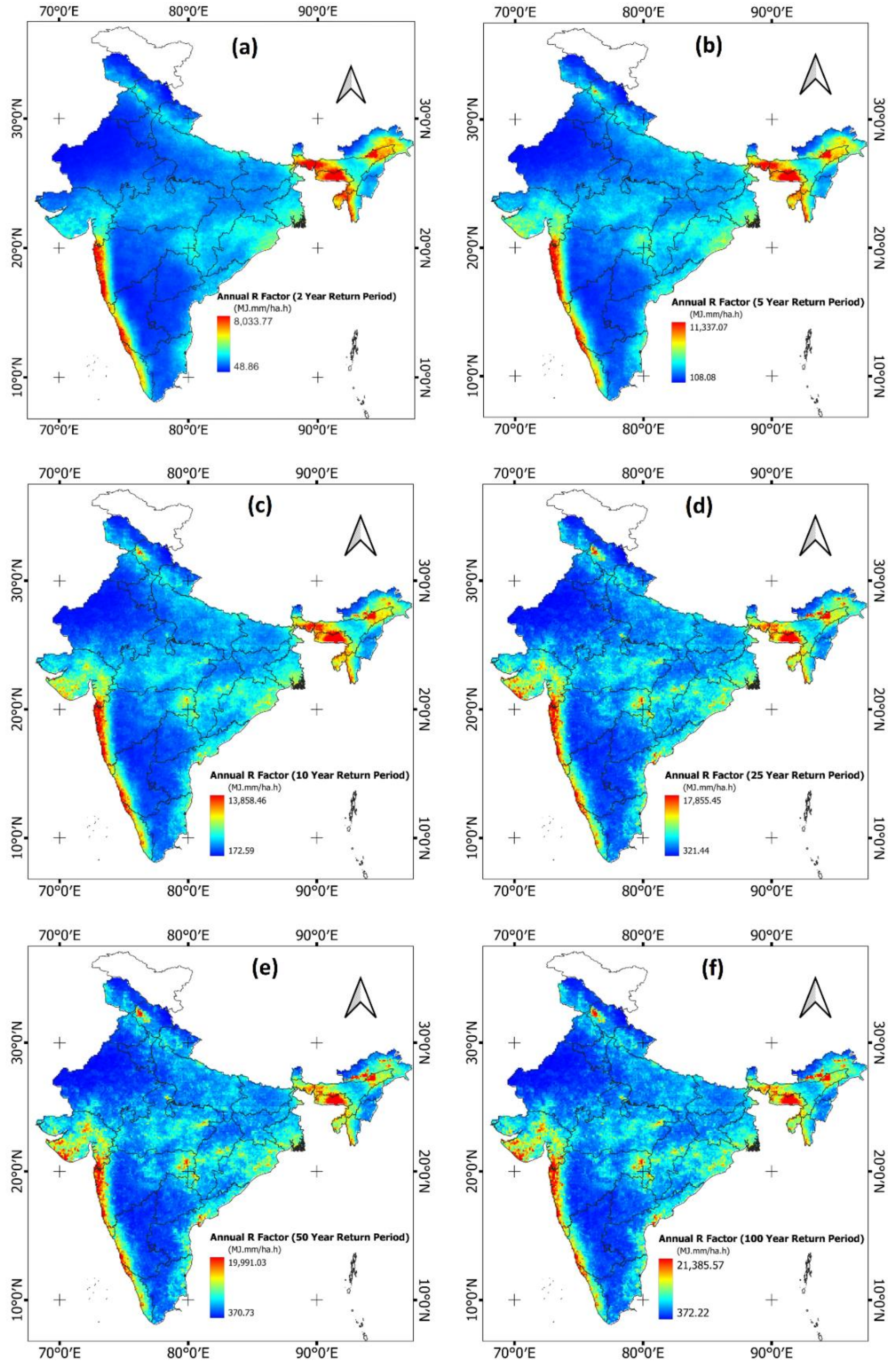

Figure 4.4 Return level map of Annual R Factor corresponding to (a) 2 year, (b) 5 year, (c) 10 year, (d) 25 year, (e) 50 year and (f) 100 year return period

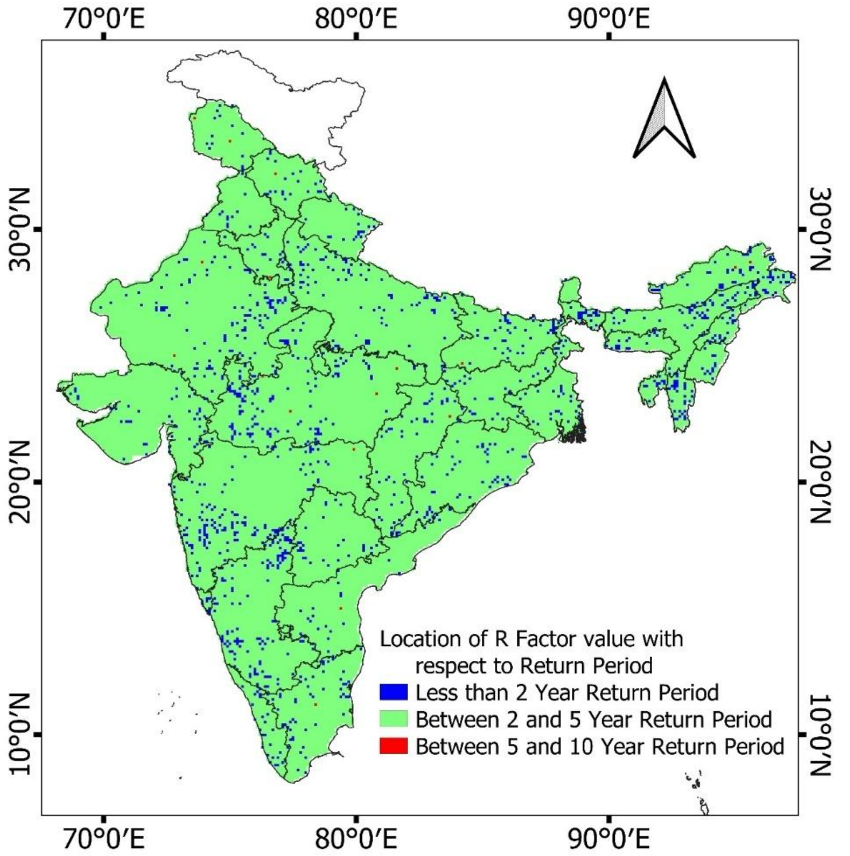

Figure 4.5 Spatial distribution of location of R factor value with respect to return period

Spatial distribution of location of R factor value with respect to return period

Table 4.1 Percentage of grid cells corresponding to R factor falling in the different range of Return Period

Return period range	Percentage of area
Less than 2 Year Return Period	4.98
Between 2 and 5 year Return Period	94.95
Between 5 and 10 year Return Period	0.07
Between 10 and 25 year Return Period	Nil
Between 25 and 50 year Return Period	Nil
Between 50 and 100 year Return Period	Nil
More than 100 years Return Period	Nil

The comparison between the annual average R factor at each grid and the corresponding return level values for various return periods, as investigated in our study, is visually represented in Figure 4.5 and summarized in Table 4.1. The findings of this study reveal that in 94.96% of cases, the annual average R factor falls within the range of return levels for the 2 and 5 year return periods. In 4.98% of cases, the R factor value is lower than the return level for the 2 year return period and in 0.06% of cases, the R factor value falls between the return levels for the 5 and 10 year return periods. Interestingly, no R factor values were observed to exceed the return level for the 25 year return period. The average R factor value for the entire country also falls within the range of return levels for the 2 and 5 year return periods. Taguas et al. (2011), in their study conducted in southern Spain, similarly reported that the annual average rainfall erosivity typically falls within the range of return levels for the 2 and 5 year return periods. This study also indicates that the majority of areas in the research display R factor values within this range, as depicted in Figure 4.5. Notably, this observation is not limited to specific locations but rather observed throughout the country.

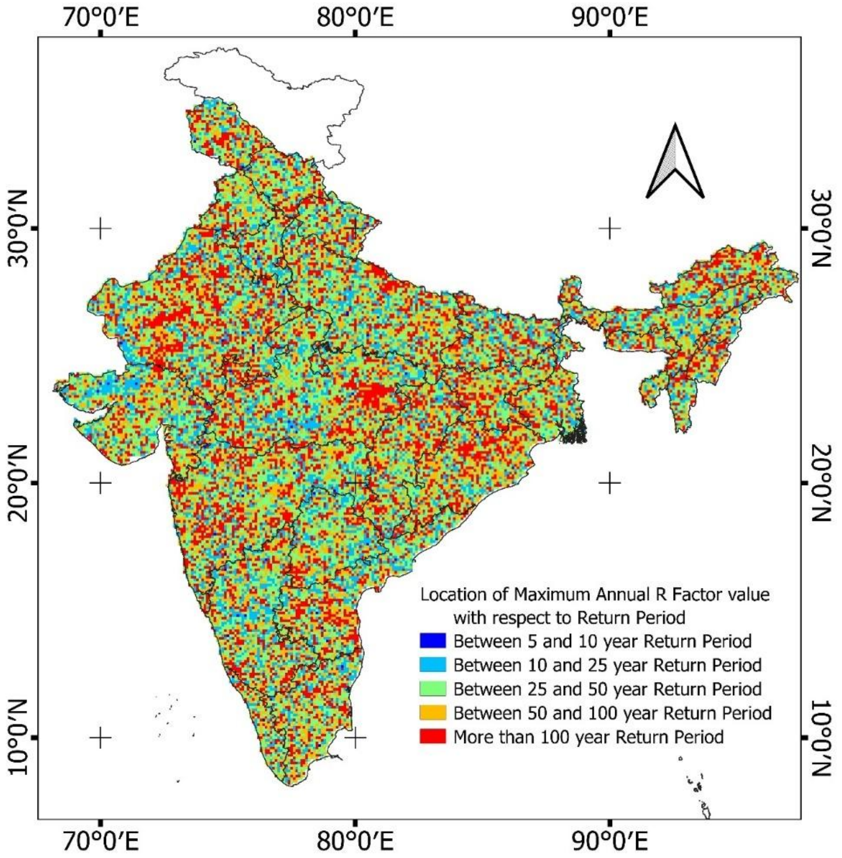

Figure 4.6 Spatial distribution of location of maximum annual R factor value with respect to return period

Table 4.2 Percentage of grid cells corresponding to maximum annual R factor falling in the different range of Return Period

Return period range	**Percentage of area**
Less than 2 Year Return Period	Nil
Between 2 and 5 year Return Period	Nil
Between 5 and 10 year Return Period	0.29
Between 10 and 25 year Return Period	18.86
Between 25 and 50 year Return Period	31.24
Between 50 and 100 year Return Period	24.30
More than 100 year Return Period	25.31

Furthermore, we compared the maximum value of the annual R factor at each grid point with the corresponding return levels for the various return periods examined in our study. The spatial distribution of these comparisons is presented in Figure 4.6 and summarized in Table 4.2. Our results indicate that in 0.28% of cases, the maximum annual R factor falls within the range of return levels for the 5 and 10-year return periods, while in 18.86% of cases, it falls within the range of return levels for the 10 and 25-year return periods. Moreover, in 31.24% of cases, the maximum annual R factor falls within the range of return levels for the 25 and 50-year return periods, and in 24.30% of cases, it falls within the range of return levels for the 50 and 100-year return periods. Intriguingly, in 25.31% of cases, the value exceeds the return level for the 100-year return period, and no values were found to be lower than the return level for the 5-year return period. The country average of the maximum annual R factor value falls within the range of return levels for the 25 and 50-year return periods, with a closer proximity to the return level for the 50-year return period. Similar to the analysis of the average R factor values, the spatial distribution of these comparisons, as illustrated in Figure 4.6, indicates a scattered distribution throughout the country. Notably, almost all average R factor values are lower than the return level for the 5-year return period, while the maximum annual R factor values exceed the return level for the 5-year return period.

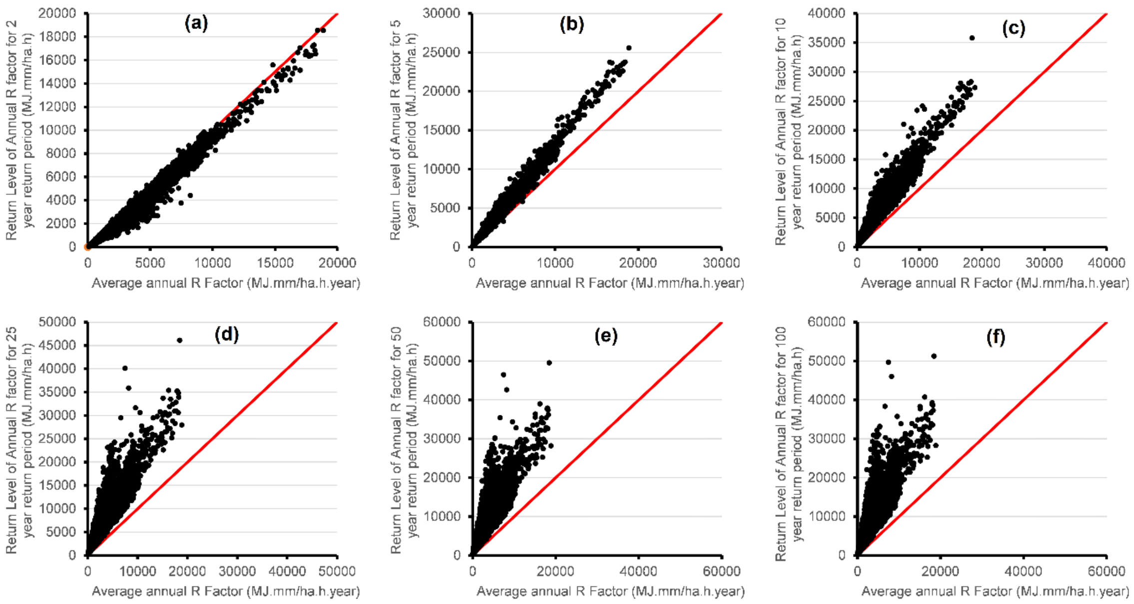

Figure 4.7 Scatter plot between return level of Annual R factor corresponding to (a) 2 year, (b) 5 year, (c) 10 year, (d)25 year, (e) 50 year and (f) 100 year return period and Average annual R factor

Figure 4.7 presents scatter plots depicting the return level of the annual R factor across different return periods in comparison to the annual average R factor. Analysing Figure 4.7, it becomes evident that the average annual R factor value aligns closely with the return level value for the 2 year return period, as demonstrated by the clustering of points near the 1:1 line. However, as the return period value increases, the points gradually deviate from the 1:1 line, signifying substantial differences between the average R factor value and the return level value corresponding to that particular return period.

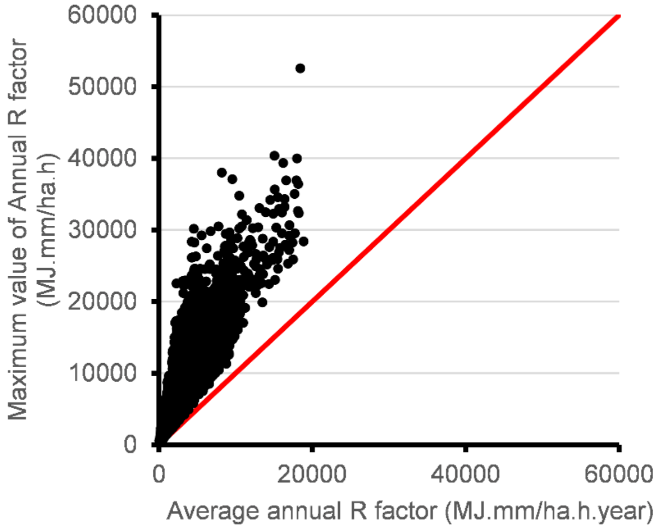

Figure 4.8 Scatter plot between maximum Annual R factor and Average annual R factor

An additional noteworthy observation that can be derived from the scatter plots is that locations characterized by identical average R factor values can exhibit varying return level values, with considerable differences observed. For instance, for a 100 year return period, the disparity in return levels between two locations can be as substantial as 40,000 MJ.mm.ha^{-}1.h^{-1}. The difference in return levels among locations with the same average R factor value diminishes as the return period value decreases. Furthermore, substantial disparities in the maximum value of the annual R factor have been observed among locations sharing the same average R factor value, as depicted in Figure 4.8. Ferro et al. (1991) conducted a study wherein they constructed a map illustrating the ratio between the return level value for a 50 year return period and the average annual R factor. This map was then compared to the map depicting the average annual R factor. The researchers observed notable disparities between the two maps, indicating significant differences in their respective representations. Sadeghi et al. (2017) conducted a study in Iran and found similar results.

During the computation of soil loss using the RUSLE, the mean annual value of the R factor is typically utilized. However, it has been observed that locations with the same average R factor can exhibit different return level values and maximum annual R factor values. Thus, it can be inferred that a soil conservation structure design deemed suitable for one location may not be adequate for another location with the same average R factor.

4.4 Conclusion

The present study provides valuable insights into the analysis of the R factor across India for different return periods. Analysis of return periods revealed that mean R factor values of the India increase with increase in return period, ranging from 1918.94 for a 2 year return period to 5806.90 MJ.mm.ha^{-1}.h^{-1} for a 100 year return period. In 94.96% of the study area the mean annual R factor values fall within the range of return level of 2 to 5 year return periods. Again, the maximum annual R factors are mostly fall within the range of return level of return periods 25 to 50 year return period. It was also found from the study that areas with similar average R factors can exhibit substantial differences in return levels values for different return period. This highlights that relying solely on the mean annual R factor may underestimate the soil loss potential of a region. The findings underscore the importance of incorporating return period analysis to achieve a more comprehensive understanding of soil erosion risk. These results hold significant implications for the application of RUSLE in the planning and design of soil conservation measures. Policymakers and stakeholders can benefit from this approach by selecting return periods appropriate for specific conservation objectives.

Chapter 5

Calibration of IMERG dataset using IMD daily gridded dataset for computing Rainfall Erosivity Factor

5.1 Introduction

A high spatiotemporal resolution precipitation dataset is essential for a wide range of hydrological and environmental studies such as soil erosion assessment, flood forecasting etc. However, the availability of such high-resolution precipitation data is limited in many regions across the globe. Satellite precipitation products have emerged as an effective solution to mitigate this limitation. They offer extensive spatial coverage and provide data in regions where conventional rain gauge networks are poor or absent. One of the most important advantages of satellite precipitation estimates is their ability to uniformly capture the spatial variability in rainfall.

The rapid advancements in satellite precipitation estimation techniques have significantly enhanced the ability to continuously monitor precipitation at global scales with finer spatial and temporal resolutions over the past few decades. Among the available datasets, the Integrated Multi-satellite Retrievals for GPM (IMERG) product developed by NASA was used in the previous two chapters of this study. The IMERG dataset provides half-hourly precipitation estimates at a spatial resolution of 0.1° (Huffman et al., 2019) making it highly suitable for high-resolution hydrological applications. Despite its advantages IMERG also involves significant uncertainties that differ in magnitude and nature across various geographic regions and climatic conditions. Many past studies have reported that IMERG often overestimates daily and hourly rainfall amounts in high altitude regions (Xu et al., 2019).

The fundamental reason behind such uncertainties lies in the indirect approach of estimating satellite precipitation and due to which systematic and random errors are introduced into the dataset. Consequently, calibration of satellite precipitation products with rain gauge data is essential to improve their accuracy and reliability (Huffman et al., 2019). The IMERG is calibrated at the monthly scale using the Global Precipitation Climatology Centre (GPCC) gauge analysis dataset having a spatial resolution of 1.0° and monthly temporal resolution. Although monthly calibration allows IMERG to perform reasonably well at broader temporal scales its accuracy decreases when used at finer resolutions like daily or sub-daily levels (Ma et al., 2020). This limitation makes it necessary to calibrate IMERG data using observed datasets with higher temporal resolution.

The daily rain gauge datasets can play a pivotal role in this context. The India Meteorological Department (IMD) provides a high-quality, daily gridded precipitation dataset at a spatial resolution of 0.25°, which has been widely used in numerous hydrological and climatological studies across India (Prakash et al., 2018; Thakur et al., 2020b). The wide usage of IMD daily data in various research highlights its acceptance as a reliable and robust precipitation product for India. However, the IMD daily dataset has not yet been systematically used to calibrate satellite precipitation products like IMERG.

The present study aims to bridge this critical gap by calibrating the IMERG (Late) dataset against the IMD daily gridded precipitation data. A new precipitation dataset will be generated through this calibration, which will have a spatial resolution of 0.25° and a temporal resolution of 30 minutes. This refined dataset is expected to retain the temporal richness of the IMERG half-hourly estimates while benefiting from the ground-truth accuracy of the IMD daily gauge observations. The calibrated dataset will be subsequently employed to compute the Rainfall Erosivity Factor of the study area using the methodology prescribed in the Revised Universal Soil Loss Equation (RUSLE) handbook.

5.2 Materials and methodology

5.2.1 Study area

Same as Chapter 3 and 4

5.2.2 Data used

5.2.2.1 Global Precipitation Measurement Mission (GPM) Product (IMERG)

As already discussed in Chapter 3, three distinct products are available for IMERG, Early (available after four hours of detecting time), Late (available after Fourteen hours), and Final satellite gauge product (available after 3.5 months of observation month). In this chapter the IMERG (Late) product is used for the calibration and IMERG Final satellite gauge product is used for the comparison with resulted calibrated product of this study.

5.2.2.2 IMD Daily gridded data

The IMD gauge based daily gridded data has a spatial resolution of 0.25 degree. The daily rainfall records of almost 7000 gauge stations spread all over the India are used to develop this data set (Pai et al., 2014). The inverse distance weighted (IDW) interpolation method was used to develop the gridded data from the rain gauge data. The unit of rainfall is in millimetre. The spatial extent of the dataset is 6.5N to 38.5N latitude and 66.5E to 100.0E longitude. The data is available from 1901 to present and in our study the dataset from 2001 to 2020 has been used.

5.2.3 Methodology

5.2.3.1 Calibration of IMERG dataset

The Integrated Multi-satellite Retrievals for GPM (IMERG) data was calibrated against the India Meteorological Department (IMD) daily gridded rainfall product. The IMERG Final satellite gauge product was calibrated with GPCC (1°/ monthly) dataset. The objective of this chapter is to obtain a calibrated IMERG dataset at 0.25° spatial resolution and half-hourly temporal resolution, where the daily total rainfall matches the IMD (0.25°/ daily) observation and the sub-daily distribution pattern is derived from the IMERG. The Daily Spatio-Temporal Disaggregation Calibration Algorithm (DSTDCA) proposed by Ma et al. (2020) was employed for this purpose with certain modifications.

The calibration procedure was carried out through the following sequential steps:

a. The IMERG rainfall product is available at a spatial resolution of 0.1° × 0.1°. In contrast, the IMD daily gridded rainfall dataset is available at a coarser spatial resolution of 0.25° × 0.25°. The IMERG data was first regridded to 0.25° using bilinear interpolation so that both datasets are comparable on a grid-by-grid basis.

The bilinear interpolation method estimates values at a new location by applying linear interpolation sequentially in both the latitude and longitude directions. It takes into account the four closest grid cells from the source dataset and combining their contributions to assign a smooth and continuous value to the target point. This step ensures that every IMD grid cell has a matching IMERG grid cell covering the same area in order to properly align the two datasets spatially.

b. IMD records daily rainfall, based on a 24-hour accumulation from 08:30 IST to 08:30 IST the next day. On the other hand, IMERG records rainfall in standard UTC time and provides half-hourly data throughout the day. To bring both datasets onto the same time frame, the IMERG time series was adjusted to start from 03:00 UTC (which corresponds to 08:30 IST) each day and extend to 02:30 UTC of the following day. This step ensures temporal consistency between the satellite-derived and ground-observed datasets by representing the same 24-hour period.

c. For each day, the IMERG daily rainfall total was computed by summing the 48 half-hourly precipitation values within the adjusted 24-hour window (from 03:00 UTC of the current day to 02:30 UTC of the next day). This daily IMERG value serves as the reference for calculating sub-daily temporal weights, which describe how the rainfall is distributed across the different half-hour intervals within the day.

d. In this step, the fraction of rainfall occurring in each half-hour was calculated relative to the daily IMERG total. These fractions are called temporal disaggregation weights and are calculated as:

$$W_i = \frac{R_i}{\sum_{i=1}^{48} R_i} \tag{5.1}$$

where W_i is the temporal weight for the i^{th} half-hour interval, and R_i is the IMERG rainfall in that interval. These weights represent the proportional contribution of each half-hour to the total daily rainfall and capture the timing and pattern of rainfall that IMERG detects.

e. The temporal disaggregation weights derived from IMERG were then multiplied by the IMD daily rainfall at each grid point to produce the final calibrated half-hourly rainfall dataset at 0.25° resolution as

$$IMERG_{calibrited} = W_i \times IMD_{daily} \tag{5.2}$$

This ensures that the daily rainfall total matches the IMD data and the sub-daily distribution pattern is retained from the IMERG.

f. If IMERG daily rainfall was zero but IMD reported non-zero rainfall, the IMD daily total was evenly distributed across all 48 half-hour intervals, assigning equal rainfall to each time step. If the IMD daily rainfall was zero the calibrated half-hourly rainfall values were also set to zero regardless of any non-zero IMERG estimates. This ensures strict adherence to the ground truth in terms of rainfall occurrence.

g. In situations where the IMERG signal is sparse, particularly when only one or two half-hourly time steps record non-zero rainfall, a direct application of temporal weights may result in unrealistically high sub-daily intensities when the IMD daily is higher. To address this, a 5-point symmetric triangular kernel was employed to redistribute the IMD daily rainfall more realistically across time. Mathematically, the kernel is defined over 5 half-hourly intervals such that the centre receives the highest weight, and adjacent steps receive proportionally less, while the entire kernel sums to unity.

This approach ensures a product that combines the temporal richness of satellite data with the accuracy of gauge observations, making it suitable for hydrological modelling, climate studies, and extreme event analysis. The resulting dataset will be available for a period of 20 years (2001 to 2020) and it has been named as IMDMERG for ease of use. The methodological flow chart is shown in Figure 5.1.

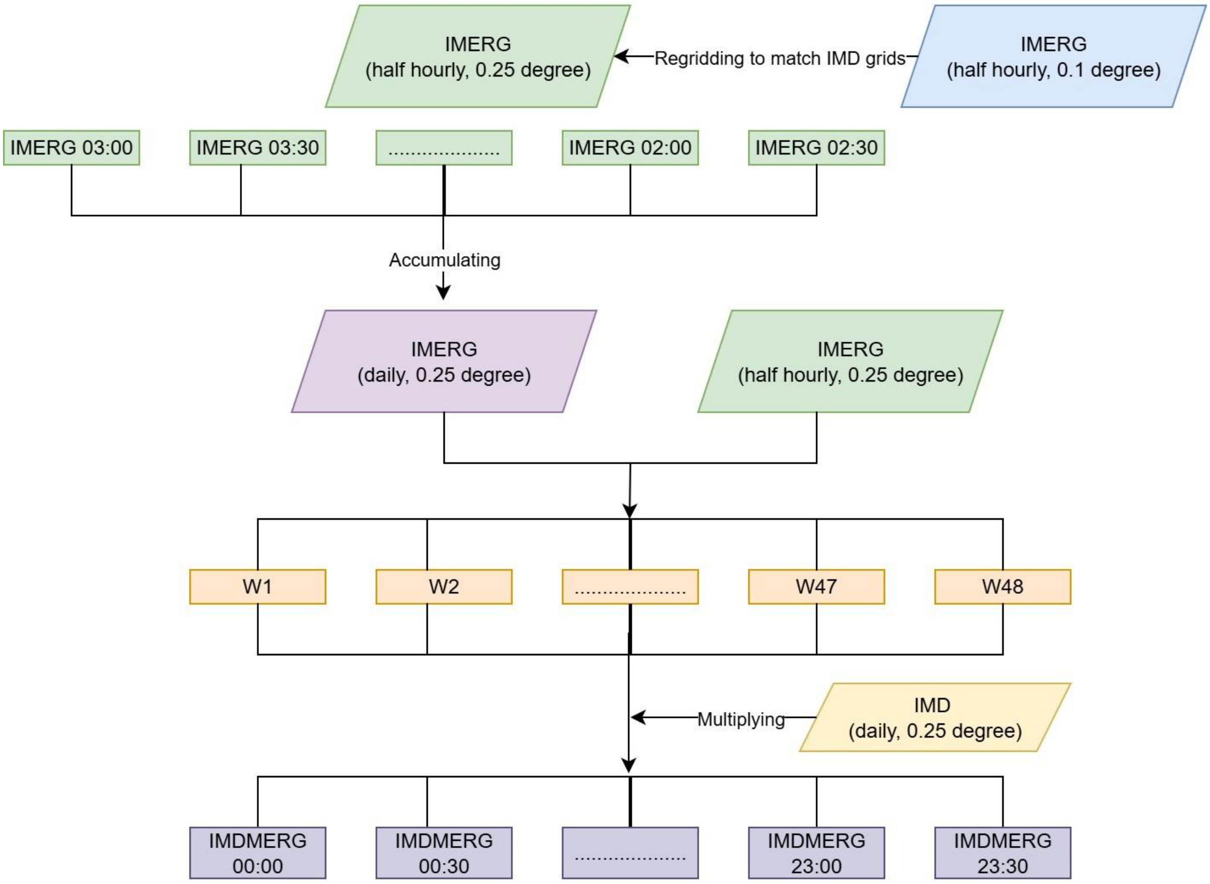

Figure 5.1 Methodological flowchart of calibration process

5.2.3.2 Computation of Rainfall Erosivity Factor

Already discussed in Chapter 3

5.3 Results and Discussion

5.3.1 Calibration of satellite only IMERG rainfall dataset by IMD daily gridded dataset

Figure 5.2(a–c) presents the spatial distribution of mean annual rainfall over India for the period 2001–2020, derived from three different datasets viz. IMERG Final satellite gauge product of half-hourly resolution (Huffman et al., 2019), IMD daily gridded data (Pai et al., 2014), and the calibrated IMERG or IMDMERG half-hourly rainfall dataset. The comparison among these products provides insight into the performance of satellite-based precipitation, the gauge-based products, and the efficacy of the calibration procedure applied in this study.

The spatial mean of the mean annual rainfall is estimated as 1200 mm from IMERG, 1123.34 mm from IMD, and 1123.31 mm from IMDMERG. The IMERG dataset thus reports a higher average rainfall, overestimating IMD by approximately 7%. In terms of maximum rainfall, the highest mean annual values are 4641.19 mm for IMERG, 5923.91 mm for IMD, and 5923.91 mm for IMDMERG. The identical values of mean and maximum between IMD and IMDMERG reflect the design of the calibration procedure. The IMERG data were adjusted to match IMD at each grid point, thereby preserving daily rainfall total of IMD in the construction of IMDMERG. This ensures that IMDMERG retains the strengths of IMD while maintaining the finer temporal resolution of IMERG.

However, the spatial patterns reveal more intricate differences. IMDMERG is able to preserve the spatial distribution of IMD rainfall. In contrast, IMERG displays spatial anomalies that are especially evident in regions of complex terrain and high rainfall. For example, both IMERG and IMD datasets depict the Western Ghats as a zone of high rainfall. However, the IMD dataset shows that these high values are not only more intense but also extend over a larger spatial area compared to IMERG.

In North East India, both IMERG and IMD detect significant rainfall, but their spatial distribution is different. IMERG shows higher values concentrated mainly over Meghalaya, Assam, portions of Arunachal Pradesh, Tripura, and Mizoram. In contrast, IMD depicts the highest rainfall values over Arunachal Pradesh, Meghalaya, Sikkim, and smaller portions of Assam, Tripura, and Mizoram. Such differences highlight the challenge of accurately detecting the location and intensity of heavy rainfall in regions with complex topography. Other than these critical zones i.e. the Western Ghats and

Northeast India, the rainfall distribution patterns among IMERG, IMD, and IMDMERG show relatively close agreement, suggesting that IMERG final satellite gauge product perform better in less complex terrains.

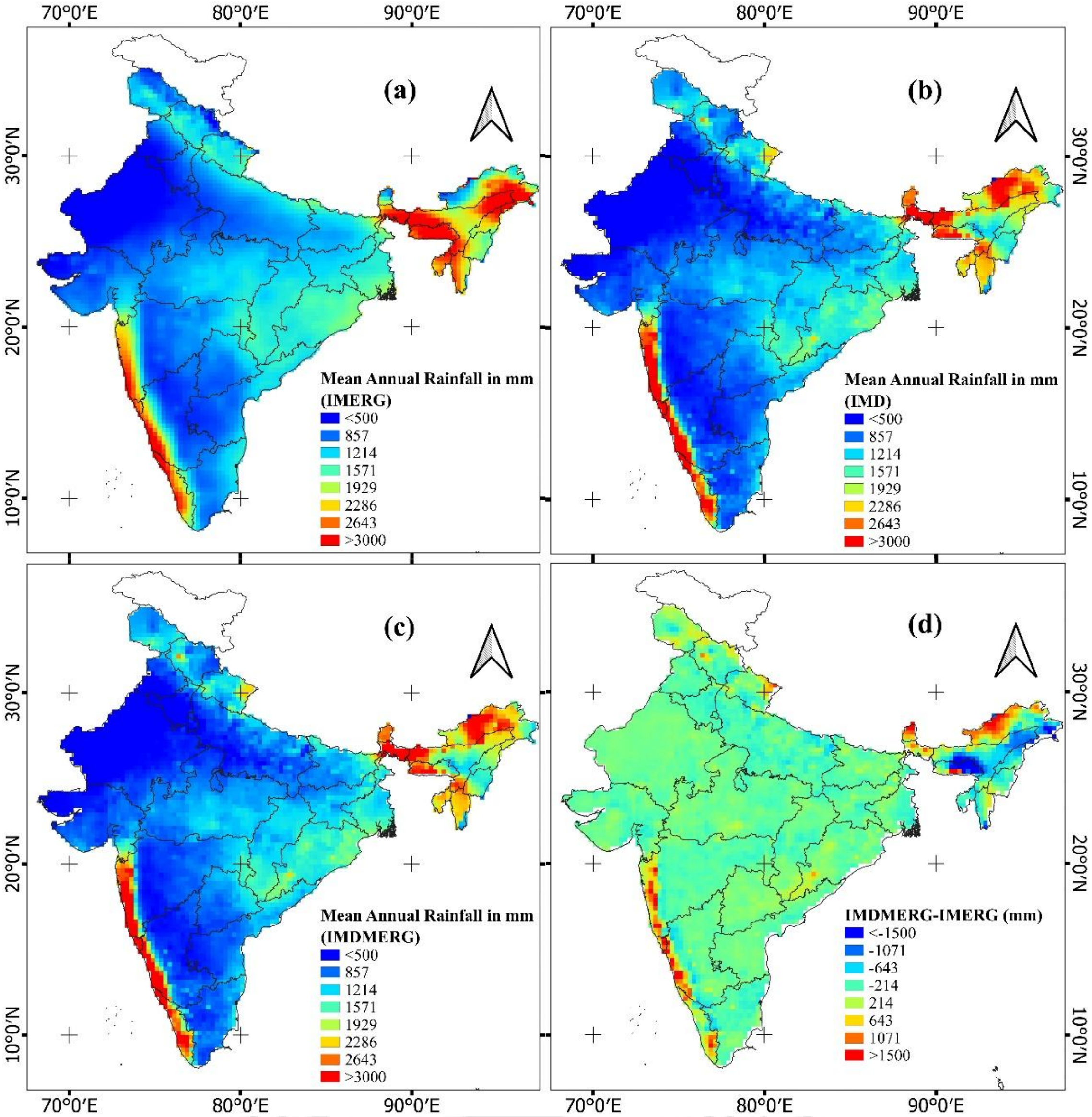

Figure 5.2 Mean Annual Rainfall (2001 to 2020) computed by (a) IMERG, (b) IMD and (c) IMDMERG and (d) the difference in Mean Annual Rainfall between IMDMERG and IMERG (2001 to 2020)

The difference map presented in Figure 5.2(d), showing IMDMERG minus IMERG mean annual rainfall, further clarifies the spatial anomalies. The regions where IMDMERG exceeds IMERG include the Western Ghats (covering Maharashtra, Karnataka, and Kerala), Arunachal Pradesh, Sikkim, Meghalaya, and smaller regions in Himachal Pradesh and Uttarakhand. Conversely, IMERG shows higher rainfall than IMDMERG in selected areas of Meghalaya, Assam, and parts of Arunachal Pradesh. These differences underscore the importance of calibration in regions where satellite algorithms may face difficulties due to orographic effects.

A scatter plot of daily mean rainfall values of IMD and IMERG dataset across all the grid points was generated to quantify the agreement between the two datasets and shown in Figure 5.3. The resulting coefficient of determination (R^2) is 0.612, indicating a moderate agreement between the two datasets. This degree of correlation indicates that although IMERG reflects overall rainfall variability significant discrepancies still exist.

The above results indicate a consistent pattern that the largest anomalies between IMERG and IMD/IMDMERG occur in the hilly complex terrains specifically in the Western Ghats and North East India. These are also the areas where extreme rainfall is most frequently observed. This outcome aligns with the findings from previous studies. Prakash et al. (2018) and Thakur et al. (2020) have demonstrated that IMERG underestimates extreme rainfall events, while Kumar et al. (2022) further reported its limitations in high-elevation regions. Such deficiencies are attributable to the inherent challenges faced by the IMERG precipitation in capturing extreme precipitation intensities and orographic enhancements.

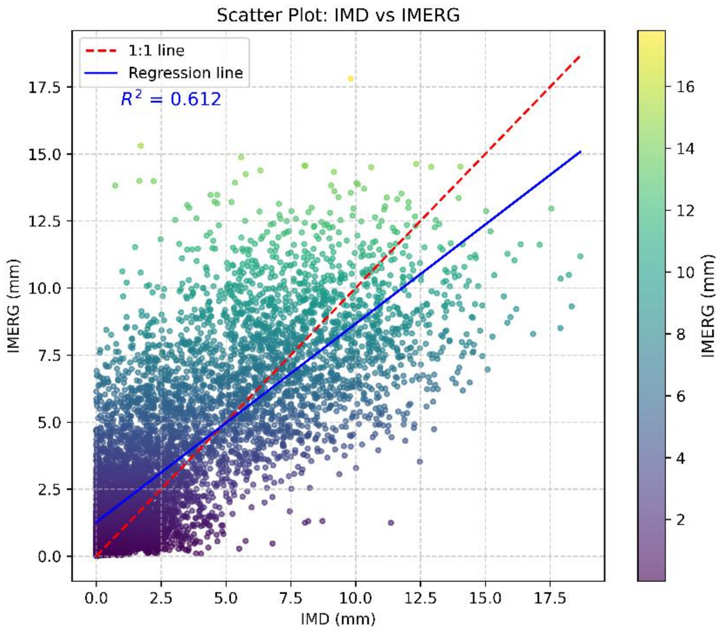

Figure 5.3 Scatter plot of daily mean rainfall values across all grid points comparing IMD and IMERG

The IMDMERG provides a significant improvement by calibrating IMERG Late product against high-resolution gauge-based IMD data, the new dataset preserves the observed rainfall magnitudes and spatial distribution while offering the high temporal resolution.

5.3.2 Rainfall Erosivity Factor Computation

The primary objective of this chapter is to develop a Rainfall Erosivity Factor (R) map using the calibrated IMERG dataset i.e IMDMERG. A continuous 20-year dataset (2001–2020) of IMDMERG was employed to compute the R factor for the study area, following the standard procedure outlined in the RUSLE handbook. The IMDMERG dataset provides rainfall estimates at a spatial resolution of 0.25° and a temporal resolution of 30 minutes. The final analysis, therefore, results in an R factor map with 0.25° grid resolution, as no interpolation was applied during the process and each grid cell represents a fixed value corresponding to its 0.25° × 0.25° area.

During the computation of R factor values from IMDMERG, it was observed that certain locations in Meghalaya exhibited exceptionally high erosivity values. These extreme values are distinctly visible in the latitude vs. R factor scatter plot Figure 5.4. To avoid the overestimation, the R factor values at these locations were restricted to a maximum threshold value prior to the generation of the final R factor map. The threshold value is fixed as 49,935 MJ.mm/ha.h.yr, which is the maximum historical R Factor of India stated by Das and Jain (2023). This correction affected eight grid points in Meghalaya, which also corresponded to the locations recording the highest mean annual rainfall across the dataset.

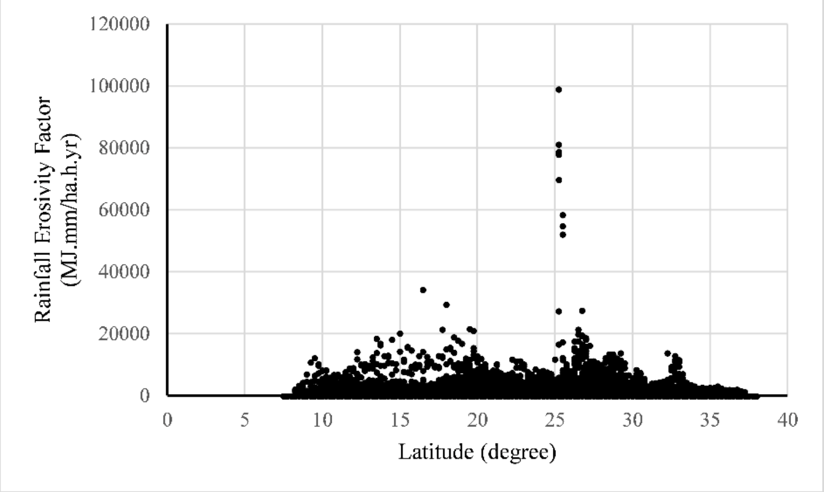

Figure 5.4 Rainfall Erosivity Factor vs. Latitude scatter plot for visualising the extreme values

Further investigation into the root cause of these anomalies revealed that, in some locations, the IMERG Final satellite gauge product represented daily rainfall totals in only three or four half-hourly intervals. While the IMD daily dataset reported large rainfall amounts, IMERG distributed this rainfall into fewer time steps, leading to unrealistically high rainfall intensities within short intervals. To address this issue, an additional step (point g of 5.2.3.1) was introduced in the methodological framework. This step employed a five-point symmetric triangular kernel to distribute high rainfall spikes across five consecutive half-hourly intervals, thereby reducing the problem of extreme sub-daily intensities. However, this adjustment was applied only when such anomalies were detected in up to two time steps per day. If more than two such anomalies occurred, no correction was applied and the original IMERG distribution was retained. The intervention was deliberately restricted to two consecutive time steps to prevent excessive modification of the IMERG dataset. Extending the adjustment beyond this limit could distort its inherent structure and compromise the originality of the dataset.

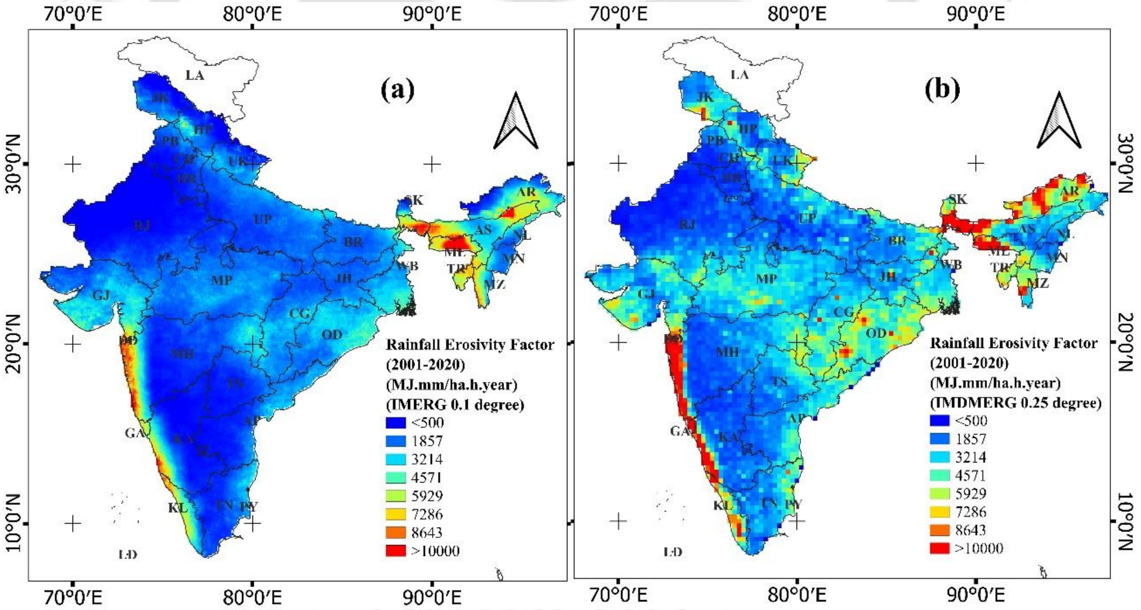

Figure 5.5 Rainfall Erosivity Factor of India (2001 to 2020) using (a) IMERG (0.1^{o}, half hourly) and (b) IMDMERG (0.25^{o}, half hourly) rainfall dataset

It is important to note that such anomalies are not unexpected, given the limitations of satellite-based precipitation products. Previous studies, including Ma et al. (2020), have reported that IMERG often underperforms in mountainous regions and under extreme rainfall conditions. Furthermore, IMERG may sometimes interpret a series of consecutive storms as a single prolonged rainfall event, which in turn can lead to an overestimation of erosivity. The final R factor map derived from IMDMERG is presented in Figure

5.5(b). The values range between 0 and 49,935 MJ.mm/ha.h.yr, with a spatial mean of 3063 MJ.mm/ha.h.yr. This mean is approximately 40% higher than the mean R factor computed using IMERG Final satellite gauge product.

Although the IMERG dataset slightly overestimates the spatially averaged rainfall compared to IMD (by about 7%), the rainfall erosivity factor (R factor) does not depend solely on total rainfall amount. Instead, it is primarily governed by rainfall intensity and the temporal distribution of precipitation events. While IMDMERG rainfall values are adjusted to be closer to IMD in terms of total rainfall volume, this correction process can modify the intra-day rainfall structure, particularly the frequency, duration and intensity of rainfall events. A higher average rainfall indicates greater rainfall volume, but greater volume does not necessarily imply higher intensity. The R factor increases mainly due to the presence of more intense and long-duration rainfall events, which contribute disproportionately to erosivity through higher kinetic energy. Therefore, the observed 40% increase in the R factor derived from IMDMERG compared to IMERG highlights the fact that rainfall erosivity is more sensitive to rainfall intensity characteristics than to mean rainfall totals. Consequently, even small variations in rainfall volume can lead to a pronounced amplification of R factor values when intense rainfall events are more frequent.

A comparison between the spatial distributions of the IMERG-based and IMDMERG-based R factors is provided in Figure 5.5 (a-b). Both maps reveal that higher erosivity values are concentrated in the Western Ghats and North East India. However, the extent and spatial distribution of these high values differ between the two datasets. In the IMDMERG map, the Western Ghats display a broader spatial coverage of high R factor values compared to the IMERG map. In North East India, the IMDMERG map highlights concentrated high values across parts of Meghalaya, Assam, Arunachal Pradesh, and the adjoining region of West Bengal bordering Sikkim and Assam. In contrast, the IMERG map shows higher values mainly over Meghalaya and certain other parts of Assam that differ from the IMDMERG hotspots. The IMDMERG derived map also identifies additional zones of high erosivity over the Eastern Ghats that are not as prominently represented in the IMERG based map. Low R factor values are consistently observed in both maps across southern and northern India. However, IMDMERG also shows moderate erosivity values in central India which are not present in the map derived from IMERG. These differences underscore the value of calibration with daily observed rainfall dataset in enhancing the satellite rainfall products. The ability of IMDMERG to capture additional erosivity hotspots demonstrates the potential of this dataset to provide more robust and spatially representative erosivity estimates.

5.4 Conclusion

The present chapter has undertaken a comprehensive exercise to calibrate the satellite precipitation product IMERG (Late) (0.1°, half hourly) with the ground-based IMD gridded dataset (0.25°, daily), with the objective of producing a high-resolution gauge adjusted rainfall dataset for the study area. The calibrated dataset has been termed IMDMERG (0.25°, half hourly). The calibration was carried out using the Daily Spatio-Temporal Disaggregation Calibration Algorithm (DSTDCA) proposed by Ma et al. (2020) with certain modifications. The results indicate that IMERG Final Satellite gauge product slightly overestimates rainfall with a spatial mean of 1200 mm as compared to 1123 mm from IMD. Spatial analysis further revealed some discrepancies in complex terrains such as over the Western Ghats and Northeast India. In contrast, IMDMERG successfully reproduced both the spatial distribution and magnitudes of IMD rainfall while retaining the finer temporal resolution of IMERG. The R factor map was generated using the IMDMERG dataset following the standard method outlined in RUSLE handbook. This map identified additional high erosivity zones over the Eastern Ghats and parts of Arunachal Pradesh, which were absent in the R-factor map derived from IMERG Final satellite gauge product.

Overall, the findings demonstrate that IMDMERG offers a distinct improvement over IMERG by combining the spatial accuracy of IMD with the temporal richness of IMERG. The enhanced dataset strengthens the reliability of erosivity estimates and provides significant utility for soil erosion and related hydrological studies.

Chapter 6

Climate change impact on Rainfall Erosivity Factor under CMIP6 shared socio-economic pathways

6.1 Introduction

In this chapter an effort has been made to examine the impact of the climate change on the Rainfall Erosivity factor over the major contributing watershed of "*Deepor beel*" (beel is the synonym for wetland in Assamese language) of Guwahati, Assam for two shared socio-economic pathways of CMIP6. Guwahati, once abundant with water bodies and ponds, relied on these natural reservoirs to balance rainfall during the monsoon season. However, the unplanned urbanization of the city has led to the rampant shrinkage of these water bodies due to illegal encroachments. Among all the water bodies in the region, "*Deepor beel*" stands out as the largest and holds the prestigious designation of being a Ramsar site, highlighting its ecological and environmental significance. The urban flood of Guwahati is heavily dependent on the carrying capacity of "*Deepor beel*". The shrinking of the total area of the waterbody is visible cause for declining the carrying capacity of "*Deepor beel*" (Bordoloi, 2015). However, there is an unseen or often ignored cause present, which is affecting the carrying capacity in the vertical direction in terms of deposition of sediments (Baishya and Sarma, 2024). One of the main reasons for this increased sedimentation is expansion of the city in the hills, where people are cutting forest to construct their houses which is making the soil vulnerable to erosion. During heavy rainfall, erosion occurs in these areas and the eroded soil flows with the runoff water and gets deposited, which plays a major role in declining the water capacity of urban drains along with various natural reservoirs, further aggravating Guwahati's urban flooding issues. This study holds particular importance for the Pamohi watershed in Guwahati City. The climate change-driven intensified rainfall and soil erosion contribute significantly to urban flooding and the sedimentation of nearby natural reservoirs. These conditions generate serious risks to sustainable urban water management. The current study will be very much instrumental in designing the future flood mitigation plan of Guwahati city.

As outlined in Chapter 1, this study adopts two distinct approaches to investigate the potential impacts of climate change on Rainfall erosivity factor. In the first approach, a Multiple Linear Regression (MLR) based empirical equation will be developed to estimate the rainfall erosivity factor (R Factor). This equation will then be applied to project future R Factor values under varying climate scenarios. In the second approach, the projected daily rainfall data from Global Climate Models (GCMs) will be disaggregated into hourly rainfall series. The standard procedure given in the RUSLE handbook will be applied to compute the future R Factor using the disaggregated high-resolution rainfall data. Both approaches will be applied to the same study area for a comprehensive comparative assessment of their results. A detailed comparison and discussion of the outcomes from these two methodologies will also be presented.

6.2 Study Area

The Ministry of Environment, Forest and Climate Change has designated "*Deepor Beel*" as an Eco-sensitive zone. This area is notable for being Assam's sole Ramsar site, situated to the southwest of Guwahati city. It offers a distinctive environment for both aquatic plants and bird species and holding significant biological and ecological value. Additionally, "*Deepor Beel*" serves as a primary storm water reservoir for Guwahati city. In the winter months, the water surface area of the lake reduces by approximately fifty percent leading to the exposure of the shoreline extending up to one kilometer. This exposed land becomes suitable for cultivating rice paddy, thanks to the cooler and drier climatic conditions. The tropical monsoon season extends from May to September, characterized by high humidity, while pre-monsoon showers occur from March to May. Between May and September, the lake primarily receives water from several sources, including the Pamohi, Kalmani, and Khanajan rivers, as well as local runoff from the monsoon rains. However, Pamohi river contributes maximum amount of water to "*Deepor Beel*" and the Pamohi watershed covers almost half of Guwahati City. In this study, the Pamohi watershed has been considered to compute the present and future rainfall erosivity factor considering climate change scenario. The location of the study area is presented in Figure 6.1. The area of the watershed is approximately 156 km^2. The watershed is significant from the context of urban floods occurring every year in Guwahati city. Rapid urbanization, driven by increased housing and construction activities in the city, has resulted in a rise in buildings, streets, and other impervious surfaces. This development has significantly reduced the number of inland wetland pockets and clogged drainage systems, contributing to uncontrolled flooding. Additionally, the unplanned expansion of the city to accommodate the growing population has caused extensive encroachment into wetlands, low-lying areas, and hills, along with a reduction in forest cover. The resulting deforestation of hills and loss of wetlands have exacerbated issues like artificial flooding and waterlogging.

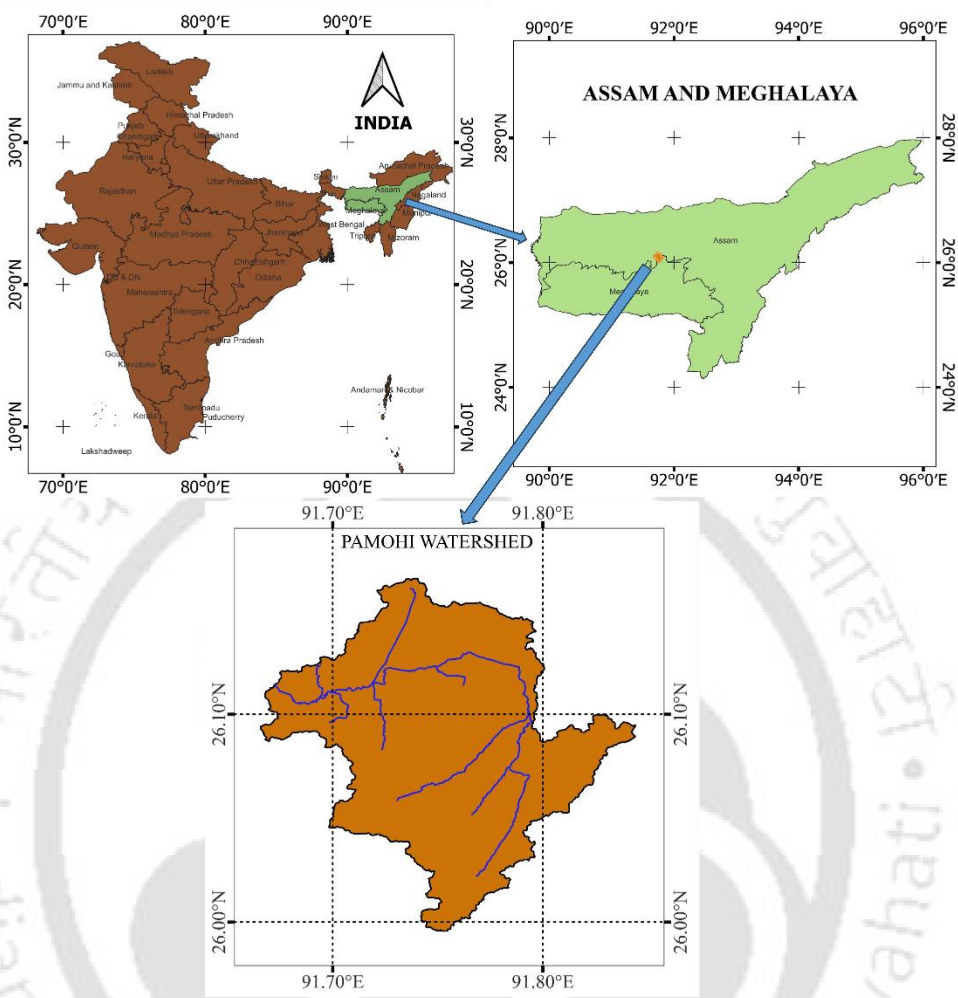

Figure 6.1 Location of the study area

6.3 Data Used

6.3.1 IMD Daily gridded data

The IMD gauge based daily gridded data has a spatial resolution of 0.25 degree. The daily rainfall records of almost 7000 gauge stations spread all over the India are used to develop this data set (Pai et al., 2014). The unit of rainfall is in millimetre. The spatial extent of the dataset is 6.5N & 66.5E to 38.5N & 100.0E. The data is available from 1901 to present and in our study the dataset from 1986 to 2014 has been used.

6.3.2 Rain Gauge data

The half hourly rainfall data were obtained from a raingauge station located at the India Meteorological Department (IMD) office in Guwahati, Assam, India (26.1077° N, 91.5938° E). The required half-hourly data for developing the Multiple Regression Model were not available in digital format and were manually extracted from pluviograph. The dataset covers the period from 1996 to 2010 and from 2013 to 2016. Data for the years 2011 and 2012 were not available due to instrument malfunction during that time.

6.3.3 CMIP6 precipitation data

CMIP6 uses shared socio-economic pathways (SSPs) instead of Representative Concentration Pathways (RCPs) used in CMIP5. While RCPs focused solely on emissions and radiative forcing, SSPs integrate socioeconomic narratives, providing a broader context for climate and policy analysis. The bias-corrected daily precipitation dataset developed by Mishra et al. (2020) for Southeast Asia has been utilized for rainfall erosivity estimation. This study used two combined scenarios of the Shared Socioeconomic Pathways: SSP2 with RCP4.5 and SSP5 with RCP8.5. This dataset used in this study covers both the historical period (1986–2014) and three future timeframes: near future (2015–2040), mid future (2041–2070), and far future (2071–2100).

Mishra et al. (2020) utilized the high-resolution 0.25-degree gridded precipitation dataset from the India Meteorological Department (IMD) for bias correction of CMIP6 precipitation projections over the Indian region. The bias-corrected projections maintained spatial consistency with the patterns observed in the original CMIP6 GCM outputs (Das and Jain, 2023). Mishra et al. (2020) provided bias-corrected precipitation data derived from 13 different Global Climate Models (GCMs).

6.4 Statistical Parameters for performance evaluation

In this study, different combinations of the following statistical parameters are used for assessing performance of MLR model based empirical equations and various Global Climate Models (GCMs).

$$\text{Coefficient of determination, } R^2 = \left[\frac{\sum_{i=1}^{n}\left(Y_i^{obs}-\overline{Y_{obs}}\right)\left(Y_i^{com}-\overline{Y_{com}}\right)}{\sqrt{\sum_{i=1}^{n}\left(Y_i^{obs}-\overline{Y_{obs}}\right)^2}\sqrt{\sum_{i=1}^{n}\left(Y_i^{com}-\overline{Y_{com}}\right)^2}}\right]^2 \qquad (6.1)$$

$$\text{Nash-Suttcliffe efficiency, NSE} = 1-\left[\frac{\sum_{i=1}^{n}\left(Y_i^{obs}-Y_i^{com}\right)^2}{\sum_{i=1}^{n}\left(Y_i^{obs}-\overline{Y_{obs}}\right)^2}\right] \qquad (6.2)$$

$$\text{Root Mean Square Error, RMSE} = \sqrt{\frac{1}{n}\sum_{i=1}^{n}\left(Y_i^{com}-Y_i^{obs}\right)^2} \qquad (6.3)$$

$$\text{Percentage Error, P.E} = \frac{|\text{Computed Value} - \text{Actual Value}|}{|\text{Actual Value}|} \times 100\% \tag{6.4}$$

$$\text{Mean Absolute Error, MAE} = \frac{1}{n}\sum_{i=1}^{n}\left|Y_i^{obs} - Y_i^{com}\right| \tag{6.5}$$

$$\text{Percent BIAS, PBIAS} = \frac{1}{n}\sum_{i=1}^{n}\frac{Y_i^{com} - Y_i^{obs}}{Y_i^{obs}} \times 100 \tag{6.6}$$

where Y_i^{com} is the ith computed value of a parameter; Y_i^{obs} is the ith observed value of the parameter and $\overline{Y_{obs}}$ is the mean value of the observed data series, and $\overline{Y_{com}}$ is the mean value of the computed data series of the parameter.

The R^2 indicates how much of the variability in the observed data is explained by the model. Its value ranges between 0 and 1, with values closer to 1 representing a better fit and values near 0 showing poor explanatory power. NSE evaluates the predictive skill of a model by comparing simulated values to observed data, where values closer to 1 indicate better performance. RMSE indicates the standard deviation of prediction errors, emphasizing larger errors due to squaring. The P.E expresses the relative difference between computed and actual values as a percentage. It is always non-negative, and lower percentages signify better prediction accuracy, while higher percentages denote poor performance. MAE represents the average magnitude of errors between observed and simulated values, without considering direction. PBIAS measures the average tendency of simulated values to be overestimated or underestimated compared to observed data.

6.5 Effect of Climate Change on Rainfall Erosivity Factor through developing Multiple Linear Regression based empirical equation

6.5.1 Methodology

6.5.1.1 Rainfall Erosivity Factor

Equation (6.7) represents the unit energy relationship between energy and rainfall intensity proposed by Brown and Foster in the year 1987 (Renard et al., 1997).

$$e_r = 0.29 \times [1 - 0.72 \times \exp(-0.05 . i)] \tag{6.7}$$

where,

e_r = Rainfall energy, unit: $MJ.ha^{-1}.mm^{-1}$ and

i = Rainfall Intensity, unit: $mm.h^{-1}$

The rainfall erosivity factor (R) is given as

$$R = \frac{\sum_{i=1}^{j}(EI_{30})_i}{N} \quad (6.8)$$

where $(EI_{30})_i$= EI_{30} for storm i and j = number of rainfall event in a period of N year

Now, $E = (\sum_{r=1}^{k} e_r v_r)$ and I_{30} = maximum intensity among all the 30 minutes in a storm event, where v_r is the depth of rainfall expressed in mm during the r^{th} interval of a storm event subdivided into k parts.

6.5.1.2 Multiple Linear Regression

In a multiple linear regression model, two or more variables are combined by a linear equation to predict the outcome. The outcome is generally called dependent or study variable, and the variables which are combined to give this outcome are called an independent or explanatory variable. The general form of Multiple linear regression model is as follows

$$y = \alpha_0 + \alpha_1 x_1 + \alpha_2 x_2 + \alpha_3 x_3 \ldots\ldots\ldots\ldots\ldots\ldots \alpha_n x_n + \varepsilon \quad (6.9)$$

where, α_0, α_1, α_2, α_3 ……… α_n are called the coefficient of regression linked with x_1, x_2, x_3………x_n and ε is the model’s random error term, which is to be added to the fitted linear equation to get the exact outcome (Salleh et al., 2017). Multiple linear regression analysis involves three fundamental steps: Specification, Calibration, and Validation. During the Specification step, models and predictors are chosen. In the Calibration step, the relationship between dependent and independent variables is established, and the model's accuracy is assessed during the Validation stage.

6.5.1.3 Model Development

Parameter Selection

The present study establishes the multiple linear regression model, employing $EI30_{month}$, defined as the cumulative monthly sum of EI_{30} values attributed to all storm events within that period, as the dependent variable to develop various empirical equations. Concurrently, several parameters representing precipitation characteristics are incorporated as independent variables. These parameters are systematically integrated into the model. The parameters are sourced from diverse literature. The investigation rigorously assesses the correlation with the help of Pearson Correlation Coefficient between these parameters and $EI30_{month}$ values.

The selected parameters are, the monthly summation of daily rainfall having a value greater than 10 mm, denoted as Rain10 (Loureiro and Coutinho, 2001), the number of days of a month having the daily rainfall value greater than 10 mm, denoted as Days10 (Loureiro and Coutinho, 2001), Modified Fournier Index (MFI) (Arnoldous, 1977)

The expression for MFI is given as

$$\mathrm{MFI} = \sum_{i=1}^{12} \frac{P_i^2}{P} \tag{6.10}$$

where denoting P_i as the monthly rainfall of i^{th} month and P as the annual rainfall of the respective year. A novel parameter, designated as $\mathrm{MFI_{month}}$, is introduced in this study and used in the models. It is computed as the ratio of the P_i^2 and P for each month. The fourth and final parameter is the monthly rainfall considering all the rainfall events and denoted as $\mathrm{Rain_{month}}$ (Loureiro and Coutinho, 2001).

Table 6.1 represents the Pearson Correlation Coefficient for each parameter with $\mathrm{EI30_{month}}$ value. In a general context, the Pearson correlation coefficient serves as a quantitative indicator delineating the extent of linear correlation between two variables or data series.

$$\text{Pearson correlation coefficient, } P_c = \frac{n\sum x_i y_i - \sum x_i \sum y_i}{\sqrt{n\sum x_i^2 - (\sum x_i)^2}\sqrt{n\sum y_i^2 - (\sum y_i)^2}} \tag{6.11}$$

where x_i and y_i are the values of two data series, and n is no. of such pairs.

Table 6.1 Pearson correlation coefficient for various parameters

Parameter	Pearson Correlation Coefficient
Rain10	0.79491
Days10	0.64661
$\mathrm{MFI_{month}}$	0.77919
$\mathrm{Rain_{month}}$	0.78539

Table 6.1 presents an overview wherein all parameters exhibit positive correlations, with Rain10 demonstrating the highest correlation coefficient. The temporal dynamics of $\mathrm{EI30_{month}}$, alongside the selected parameters, are visually depicted in Figure 6.2.

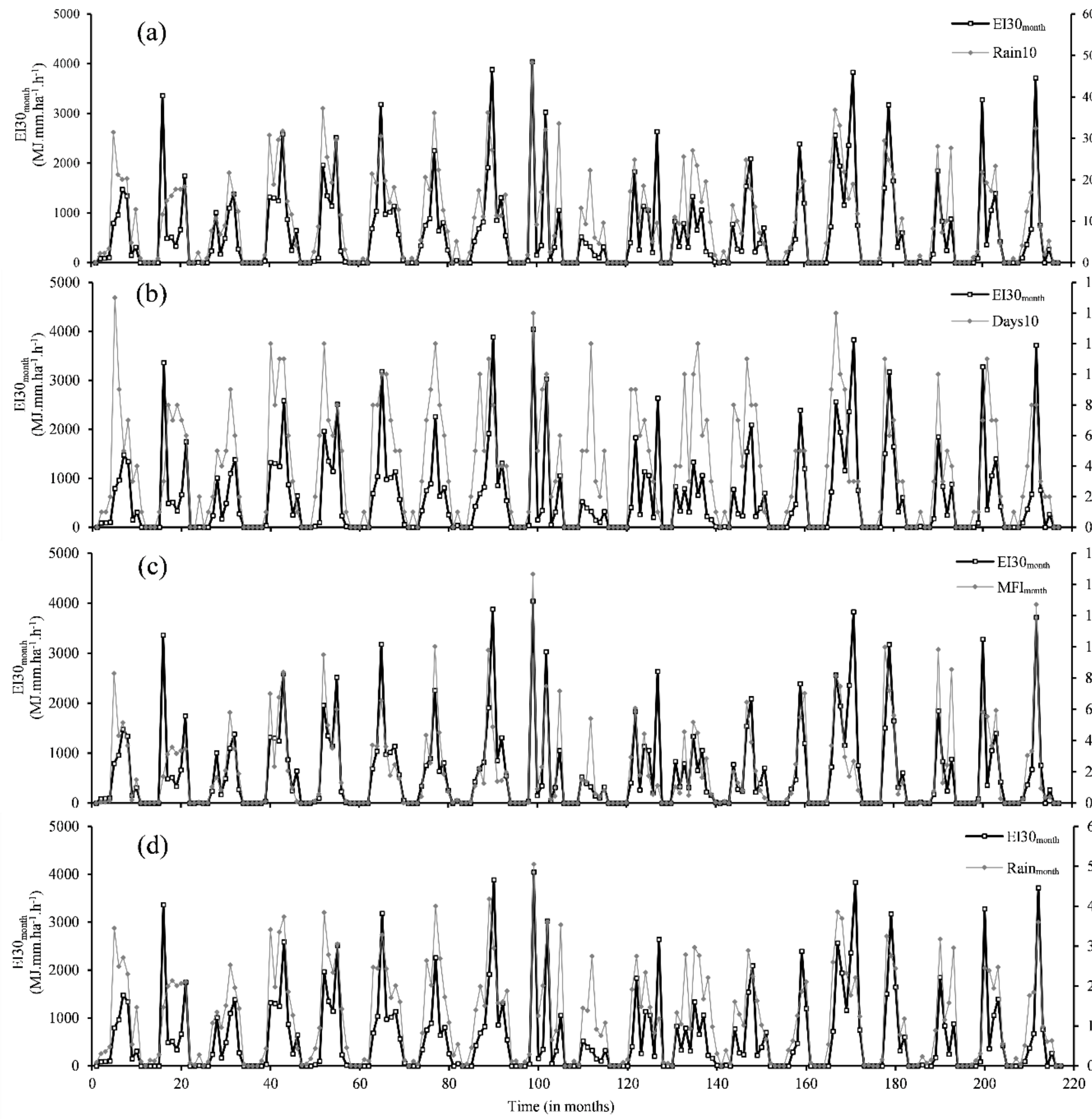

Figure 6.2 Temporal variation of $EI30_{month}$ and a) Rain10, b) Days10, c) MFI_{month} and d) $Rain_{month}$

The dataset for independent variables was prepared by utilizing 19 years of data spanning 1996 to 2010 and 2013 to 2016. MATLAB computer programming facilitated the calculation of parameter values from this extensive dataset. During model development, 11 months' worth of data were excluded due to the presence of sufficiently large number of missing values, preventing the calculation of $EI30_{month}$ values for those specific months. Subsequently, calibration was performed using data from 162 months (1996 to 2009), while the models were validated with approximately 25%, equivalent to 55 months' worth of data (2010 and 2013 to 2016).

During the calibration process, the Multiple linear regression based empirical equations are developed by using the rainfall data of 162 months (1996 to 2009) and changing the combination of independent variables. During the validation phase, the newly developed empirical equations are used to calculate the $EI30_{month}$ by using the selected monthly parameters of those 55 months (2010 and 2013 to 2016), those months which are not included in the calibration process.

Performance evaluation of MLR based empirical equations

To assess the performance of the Multiple Linear Regression (MLR) based empirical equations, the Coefficient of Determination (R^2), Nash–Sutcliffe Efficiency (NSE), Root Mean Square Error (RMSE), and Percentage Error (P.E.) (Equation 6.1, 6.2, 6.3 and 6.4) have been chosen. In this study, the $EI30_{month}$ value calculated as per standard method (Renard et al., 1997) is considered as observed or actual value, and the $EI30_{month}$ value calculated by various newly developed empirical equation is considered as computed value to evaluate the R^2, NSE and RMSE but for the evaluation of P.E the actual value is the R factor calculated as per standard method and the computed value is the R factor calculated by newly developed empirical equation.

The R^2, NSE, and RMSE are individually presented for both calibration and validation across all models. In calibration part, these parameters are calculated by using the actual $EI30_{month}$ and computed $EI30_{month}$ value of 1996 to 2009 (utilizing 162 months' data for calibration). Subsequently, during the validation phase, the parameters are determined by comparing the actual $EI30_{month}$ values with the computed $EI30_{month}$ values from 2010 and 2013 to 2016 (employing 55 months' data for validation). For the evaluation of Percentage Error (P.E), the R factor is computed by all the empirical equation by using the computed $EI30_{month}$ data of all the years except the six years where data insufficiency was found.

To detect multicollinearity among the independent variables in the multiple linear regression (MLR) models, the Variance Inflation Factor (VIF) was used. VIF measures how much the variance of a regression coefficient is inflated due to multicollinearity. A high VIF indicates that a predictor may be redundant, as it carries similar information to other predictors (Akinwande et al., 2015).

Mathematically it can be expressed as

Variance Inflation Factor, $VIF_i = \frac{1}{1-R_i^2}$ (6.12) where R_i^2 is the coefficient of determination when predictor X_i is regressed on all other predictors. If R_i^2 is high then VIF_i will also be high, which means that predictor is highly correlated with others.

A VIF value of 1 indicates that a predictor has no correlation with other predictors, which is the ideal situation in multiple regression. When VIF values fall between 1 and 5, it suggests moderate correlation, which is generally acceptable and not a major concern. However, if the VIF exceeds 5, it points to a potential multicollinearity problem, and the predictors should be carefully examined. A VIF greater than 10 signals a serious multicollinearity issue, where immediate action is needed, such as removing or reducing variables to stabilize the regression model.

The best empirical equation will be selected by comparing the result of all the statistical parameters. After that, the best equation will be compared with some available empirical methods, widely used in many recent studies. P.E is considered as the tool for comparing the models, where the actual value will be the R factor calculated as per standard method from RUSLE guidebook and the computed value will be the R factor calculated by these methods using the same rainfall dataset. The methodology for development of empirical equation has been shown in Figure 6.3.

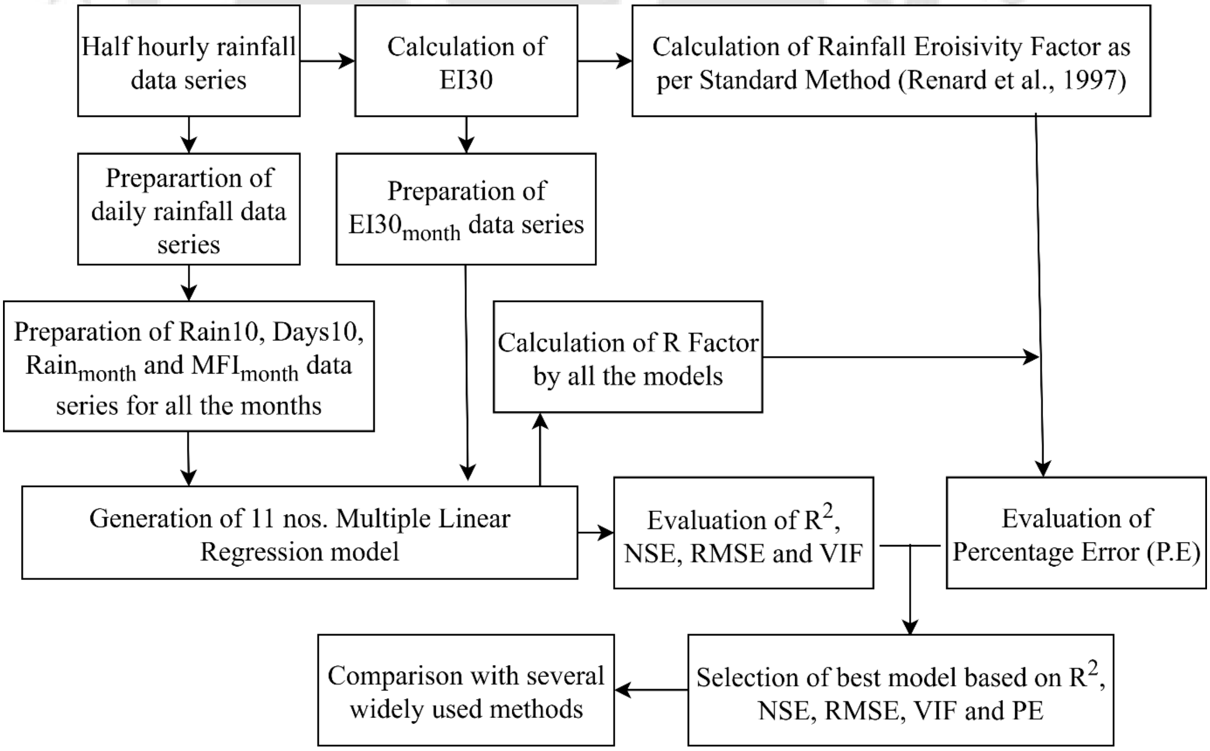

Figure 6.3 Methodological flowchart for development of Multiple Linear Regression Model based empirical equations

The statistical significance and reliability of the coefficients of the best model will also be evaluated using several standard parameters viz. Standard Error (S.E), t value, p value and confidence interval.

The standard error of a regression coefficient provides a measure of the variability of the estimated coefficient across repeated samples. Mathematically, it is expressed as

$$SE\,(\beta_j) = \sqrt{Var\,(\beta_j)} = \sqrt{s^2 (X^T X)^{-1}_{jj}} \tag{6.13}$$

where, s^2 represents the residual variance represents the square of Root Mean Square Error (RMSE), X is the design matrix of predictors, and $(X^T X)^{-1}_{jj}$ is the jth diagonal element of the inverse matrix. A smaller SE indicates greater precision in the estimation of the coefficient, whereas a larger SE implies more uncertainty. The interpretation of whether an SE is considered small or large depends on the scale of the coefficient relative to the predictor variable and the overall variability in the data.

The *t* value assesses the statistical significance of a regression coefficient by comparing the estimated coefficient to its standard error. It is mathematically expressed as

$$t_j = \frac{\beta_j}{SE\,(\beta_j)} \tag{6.14}$$

A higher absolute *t* value indicates stronger evidence that the coefficient is significantly different from zero, while a lower absolute value suggests weaker evidence. The threshold for high or low *t* value depends on the critical value of the *t* distribution at the chosen confidence level and the sample size.

The *p* value quantifies the probability of obtaining a test statistic at least as extreme as the observed *t* value under the null hypothesis that the true coefficient is zero. It is mathematically expressed as

$$p_j = 2P(T_{n-k} > |t_j|) \tag{6.15}$$

where, T_{n-k} follows a t-distribution with $n - k$ degrees of freedom. Smaller p-values indicate strong evidence against the null hypothesis, signifying statistical significance. Conversely, larger p values suggest insufficient evidence to reject the null. Thus, the interpretation of low or high p-values depends on the significance threshold (α) set.

The confidence interval provides a probable range within which the true population coefficient is expected to lie with a specified probability. It is computed as

$$CI_j = \beta_j \pm t_{\frac{\alpha}{2},n-k} . SE(\beta_j) \tag{6.16}$$

where, $t_{\frac{\alpha}{2},n-k}$ is the critical value of the t-distribution at the chosen significance level. Narrower confidence intervals indicate more precise coefficient estimates, while wider intervals imply greater uncertainty. Importantly, if the CI does not include zero, the coefficient is considered statistically significant at the chosen confidence level.

6.5.1.4 Performance evaluation of GCMs

By using the best equation, the R Factor will be computed from bias-corrected daily precipitation outputs derived from 13 Global Climate Models (GCMs) of Coupled Model Intercomparison Project Phase 6 (CMIP6) for the historical period (1986–2014). These model-based estimates were compared against the R Factor values derived from gridded daily rainfall data provided by the India Meteorological Department (IMD) using the same equation, which will be served as observational reference.

To assess the performance and reliability of each GCM in replicating observed rainfall erosivity the statistical parameters Nash-Sutcliffe Efficiency (NSE), Root Mean Square Error (RMSE) and Mean Absolute Error (MAE) (Equation 6.2, 6.3 and 6.5) will be used. In their recent review on the relationship between climate change and soil erosion, Eekhout and de Vente (2022) highlighted the necessity of utilizing multiple bias-corrected climate model datasets to reduce uncertainties in estimating rainfall erosivity and associated soil erosion risks. They recommended to use an ensemble of at least five models to enhance the reliability of projections. In alignment with this approach, the present study incorporates an ensemble of five carefully selected GCMs to assess the potential impacts of climate change on rainfall erosivity.

Each GCM will be individually ranked based on its performance under each metric. Subsequently, a cumulative rank will be calculated by summing the individual ranks across all three metrics. The GCM with the lowest total rank will be designated as the best-performing model, followed by the one with the second-lowest rank as the second-best, and so on.

Building upon the insights gained from the historical evaluation, projections of the R Factor were extended to three future time horizons, Near Future(2015–2040), Mid Future (2041–2070), and Far Future (2071–2100), considering two Shared Socioeconomic

Pathways viz. SSP245 and SSP585. These future R Factors were estimated using the same empirical equation used for computing the historical R factors, employing the bias-corrected daily precipitation data from the set of five best performing CMIP6 models. The methodological flow chart for climate change study is shown in Figure 6.4.

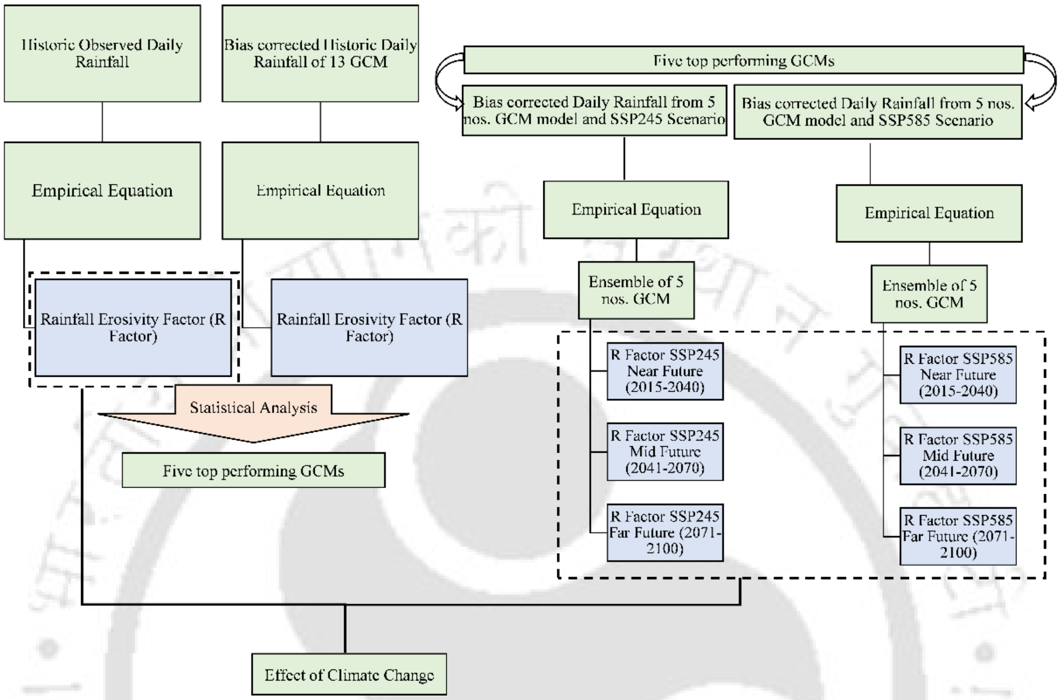

Figure 6.4 Methodological flow chart for climate change study

6.5.2 Results and Discussion

6.5.2.1 Calculation of Rainfall Erosivity Factor (R) of Guwahati

The long term Rainfall Erosivity Factor (R) for Guwahati is calculated as per the standard method given in RUSLE guidebook (Renard et al., 1997). In this study, we have gone through 19 years of half-hourly rainfall data of Guwahati, where 549 erosive events are present. The erosive events are identified by the criteria present in RUSLE guidebook. Among the 19 years data, some data are missing in 11 nos. of months, and these months are distributed among six years in the data series (1998, 2005,2009,2013,2015 and 2016). The years with missing data are not considered in the computation of R factor and annual R factor. However, in the development of Multiple linear regression (R) model based empirical equations, only the months with missing data are excluded, as in this study the MLR models are generated in monthly scale. After eliminating the 6 years data the total erosive events are reduced to 425. The annual R factor within the specified timeframe exhibits a range from 4011 MJmm/ha.h.year (minimum) to 13338 MJmm/ha.h.year (maximum). The Long-Term Rainfall Erosivity Factor (R) for Guwahati is calculated as 7623 MJmm/ha.h.year, determined by the summation of the Annual R Factor over 13 years. As per the literature, before this study, only one attempt was made to calculate the rainfall erosivity factor (R) of Guwahati city by using hourly data of 1 year in the year 2004 (Sarma et al. 2005). The calculated R factor value was 9259 MJmm/ha.h.year. This value of R factor was used in various studies related to hilly areas of Guwahati city such as estimation of soil loss by incorporating hill cut factor (Patowary et al., 2019; Patowary and Sarma, 2018), application of optimal ecological management practices (Sarma et al. 2013; Sarma & Sarma 2016; Sarma et al. 2015), assessing the sustainable carrying capacity of urban areas situated in hilly regions prone to flooding. (Sarma et al. 2016) etc. The long-term R factor of Guwahati will be used for calculating the Percentage Error (P.E) of all the models.

6.5.2.2 Development of MLR based empirical equation and their performance analysis

As shown in Table 6.2, eleven Multiple linear regression (MLR) model based empirical equations are developed by using $EI30_{month}$ and various combinations of Rain10, Days10, MFI_{month}, and $Rain_{month}$. The equations are developed without an intercept to maintain physical consistency, as $EI30_{month}$ should be zero when rainfall or rainfall-based parameters are zero. Including an intercept could lead to unrealistic non-zero $EI30_{month}$ values in the absence of rainfall. Thus, forcing the regression through the origin makes the coefficients more interpretable and physically meaningful. In all the models Rain10 and MFI_{month} are positively related to the $EI30_{month}$. However, Days10 is negatively related to $EI30_{month}$ in all the models except Model 4, where it is combined with MFI_{month} alone, and $Rain_{month}$ is positively related with $EI30_{month}$ in all the models except Model 3 and 9. Hence, Days10 is negatively related to $EI30_{month}$ when either Rain10 or $Rain_{month}$ or both are combined with Days10. Upon scrutiny of the aforementioned pattern, it is evident that, for a given month, a higher volume of rainfall concentrated over fewer days corresponds to an elevated $EI30_{month}$ value.

Table 6.2 The list of newly developed MLR model based empirical equation and their performance analysis

Model No.	Equation	Calibration			Validation			R Factor (MJmm/ha.h.year)	Percentage Error (%)
		R^2	NSE	RMSE	R^2	NSE	RMSE		
Model 1	$EI30_{month} = 10.995 \times Rain10 - 137.601 \times Days10$	0.689	0.688	451.793	0.735	0.730	532.120	7405	2.86
Model 2	$EI30_{month} = 3.908 \times Rain10 + 9.633 \times MFI$	0.643	0.643	649.732	0.615	0.609	640.562	7312	4.08
Model 3	$EI30_{month} = 9.657 \times Rain10 - 3.235 \times Rain_{month}$	0.637	0.637	487.927	0.643	0.632	621.262	7462	2.11
Model 4	$EI30_{month} = 11.447 \times Days10 + 24.926 \times MFI$	0.618	0.609	506.193	0.582	0.565	676.150	6514	14.55
Model 5	$EI30_{month} = -159.459 \times Days10 + 0.235 \times Rain_{month}$	0.676	0.673	463.010	0.735	0.726	536.390	7805	2.39
Model 6	$EI30_{month} = 13.205 \times MFI + 2.720 \times Rain_{month}$	0.638	0.638	487.066	0.608	0.602	646.860	7290	4.36
Model 7	$EI30_{month} = 10.248 \times Rain10 - 132.265 \times Days10 + 2.602 \times MFI$	0.690	0.689	451.298	0.710	0.707	554.256	7329	3.86
Model 8	$EI30_{month} = 8.266 \times Rain\ 10 - 151.045 \times Days10 + 2.811 \times Rain_{month}$	0.691	0.691	450.167	0.738	0.734	528.565	7526	1.28
Model 9	$EI30_{month} = 5.955 \times Rain10 + 8.702 \times MFI - 1.615 \times Rain_{month}$	0.644	0.644	482.768	0.618	0.612	638.009	7259	4.78
Model 10	$EI30_{month} = -142.869 \times Days10 + 8.945 \times MFI + 8.075 \times Rain_{month}$	0.684	0.684	454.985	0.697	0.695	566.391	7466	2.06
Model 11	$EI30_{month} = 6.702 \times Rain10 - 145.597 \times Days10 + 3.796 \times MFI + 3.300 \times Rain_{month}$	0.692	0.692	449.159	0.711	0.709	552.831	7436	2.45

The efficacy of each model is assessed through key metrics, including R^2, NSE, RMSE and P.E with the comprehensive results presented in Table 6.2. For the calculation of P.E values the actual value is the R factor of Guwahati calculated by using half-hourly rainfall data i.e., 7623 MJmm/ha.h.year. The multicollinearity among predictors was evaluated using Variance Inflation Factor (VIF) and presented at Table 6.3.

Table 6.3 Variance Inflation Factor (VIF) of predictors of Eleven Multiple Linear Regression Models.

Model	Variable	VIF
Model - 1	Rain10	3.518
	Days10	3.518
Model - 2	Rain10	8.746
	MFI_Month	8.746
Model - 3	Rain10	81.769
	Rain_Month	81.769
Model - 4	Days10	7.664
	MFI_Month	7.664
Model - 5	Days10	8.681
	Rain_Month	8.681
Model - 6	MFI_Month	7.579
	Rain_Month	7.579
Model - 7	Rain10	20.413
	Days10	8.211
	MFI_Month	9.370
Model - 8	Rain10	82.101
	Days10	8.716
	Rain_Month	92.991
Model - 9	Rain10	95.264
	MFI_Month	8.830
	Rain_Month	82.548
Model - 10	Days10	9.241
	MFI_Month	8.068
	Rain_Month	19.906
Model - 11	Rain10	95.364
	Days10	9.250
	MFI_Month	9.371
	Rain_Month	92.997

Among all the models, Model 1, with predictors Rain10 and Days10, was found to be the most reliable. The model has low VIF values (3.519 for both predictors), which are below the threshold of 5, indicating minimal multicollinearity and stable coefficients. Its predictive performance (validation $R^2 = 0.735$, NSE = 0.730, RMSE = 532.12, P.E = 2.86%) was only slightly lower than the best-performing model, Model 8. Although Model 8 showed better validation results ($R^2 = 0.738$, NSE = 0.734, RMSE = 528.57, P.E = 1.28%), it suffered from very high VIF values (>80), making its coefficients unreliable for interpretation. Therefore, Model 1 provides a good balance between prediction accuracy and reliability of coefficients, making it the most dependable model for practical estimation of $EI30_{month}$.

Upon a detail assessment of performance, it is evident that the models exhibit suboptimal accuracy in predicting monthly EI30 values. Nevertheless, scrutiny of Percentage Error (P.E) values reveals consistently low errors in R factor calculations across all models. On a monthly scale, notable discrepancies between computed $EI30_{month}$ values and actual $EI30_{month}$ values for specific months are discernible; however, these variations tend to converge when examined over extended periods. Given that R factor computation relies on long-term data series, the present models remain viable for determining the long-term rainfall erosivity factor (R) through the utilization of daily rainfall data. Capolongo et al. (2008) tried to develop of a simplified rainfall erosivity model in Basilicata (Sothern Italy). They computed the daily erosivity but their model performed poorly at daily scale, nevertheless, the errors exhibited a reduction when aggregating the erosivity data to monthly and annual scales.

The Rainfall erosivity factor using Model 1 (MJmm/ha.h.year) is equal to

$$R = \frac{1}{n}\left(\sum_{i=1}^{12}(EI30_{month})_i\right) \tag{6.17}$$

where, $(EI30_{month})_i = (10.995 \times Rain10 - 137.601 \times Days10)$ of the i^{th} month and n is the no. of years under consideration.

As the Model 1 is found to be the best MLR based empirical equation among the eleven models for computing the R factor with readily available rainfall data. So, this equtaion will be compared with nine widely used empirical methods of R factor.

The statistical significance and reliability of the coefficients of the best empirical equation Model 1 were evaluated using standard metrics, and the results are summarized in Table 6.4. The coefficient for Rain10 (10.995) shows a small standard error (1.158), a high t value (9.499), and an extremely low p value (8.88×10^{-16}) with a 95% confidence interval of [8.700, 13.289], indicating a strong positive and statistically significant effect. In contrast, the coefficient of Days10 (-137.601) exhibits a moderate standard error (31.365), a t value of -4.387, and a p-value of 2.72×10^{-5}, with a 95% confidence interval of [-199.785, -75.417], demonstrating a significant negative influence. The low standard errors and narrow confidence intervals of both coefficients indicate that these estimates are precise, while the high t values and extremely low p values confirm their statistical significance. Together, these metrics provide strong evidence that both the amount and frequency of rainfall play crucial but contrasting roles in controlling rainfall erosivity.

Table 6.4 The statistical significance of the coefficients of Model 1

	Coefficient	Std. Error	t value	p value	CI_lower	CI_upper
Rain10	10.995	1.158	9.499	8.88×10^{-16}	8.700	13.289
Days10	-137.601	31.365	-4.387	2.72×10^{-5}	-199.785	-75.417

6.5.2.3 Comparison with the widely used methods

Table 6.5 displays a comparison study between the newly developed empirical equation and 9 (Nine) widely used methods of calculating Rainfall Erosivity Factor (R) of the present time. The comparison is done based on the Percentage Error (P.E) in calculating the R factor. The actual value of the R factor of Guwahati is already calculated as 7623 MJmm/ha.h.year. The R factor value for the newly developed model is taken from Table 6.2, and for all the other methods, it is calculated by following the respective equation shown in Table 6.5 and using the daily data generated from the half-hourly data of Guwahati.

Table 6.5 Comparison of newly developed model with some existing and widely used methods

Sl. No.	Model	Reference	Recently used by	Computed R Factor (MJmm/ha.h.year)	Percentage Error (%)
1	$R = \frac{1}{n}(\sum_{i=1}^{12}(EI30_{month})_i)$ where, $EI30_{month}$= 10.995×Rain10 - 137.601×Days10	Newly developed		7404.65	2.86
2	$R=9.8 \times (81.5+0.38 \times P_a)$	(Babu et al., 2004)	(Kalambukattu and Kumar, 2017; Kayet et al., 2018; Tirkey et al., 2013)	6459.08	15.27
3	$R=9.8 \times (79 + 0.363 \times P_a)$	(Singh et al., 1981)	(Bera, 2017; Dutta et al., 2015; Farhan and Alnawaiseh, 2018; Ghosh et	6181.35	18.91

			al., 2013; Khare et al., 2017; Kumar et al., 2014; Kumar and Kushwaha, 2013; Singh et al. 2023)		
4	$R=0.5\times P_a\times 1.73$	(Roose, 1975)	(Devatha et al., 2015; Joshi et al., 2016; Sinha and Joshi, 2012)	972.94	87.237
5	$R = 1.735 \times 10^{(1.5\times\log_{10} F - 0.8188)}$	(Arnoldous, 1980)	(Akhila and Pramada, 2025; Ganasri and Ramesh, 2016; Magesh and Chandrasekar, 2016; Mondal et al., 2016; Prasannakumar et al., 2012; Samarinas et al., 2024; Shit et al., 2015)	1314.79	82.752
6	$R = 0.0483 \times P_a^{1.610}$ if $P_a < 850$ mm $R=587.8-1.219\times P_a+0.004105\times(P_a)^2$ if $P_a\geq 850$mm	(K. G. Renard and Freimund, 1994)	(Bhandari et al., 2015; Sheikh et al., 2011)	8218.94	7.820
7	$R=38.5+0.35\times P_a$	(El-Swaify and Arsyad, 1983)	(Chatterjee et al., 2014; Pal, 2016; Pal and Chakrabortty, 2019; Pal and Shit, 2017)	570.49	92.516
8	$R=972.75 + 9.95 \times P_a$	(Premlal, 1986)	(Fayas et al., 2019)	160.97	97.888
9	$R=-8.12+0.562\times P_a$	(Hurni, 1988)	(Alemu et al., 2025; Amsalu et al., 2014; Endalamaw et al., 2021; Endalew and Biru, 2022; Gelagay and Minale, 2016; Mustefa et al.,		846.11	88.900

			2019; Yesuph and Dagnew, 2019)		
10	$R=\frac{1}{n}\sum_{i=1}^{12}((0.689 \times P_i^{1.474})/100)$	(Xu et al., 2007)	(Xu et al., 2013)	137.37	98.198

R = Rainfall erosivity factor (MJmm/ha.h.year), P = Annual rainfall (mm), P_a = Mean annual rainfall (mm), P_i = Monthly rainfall of i^{th} month, n = No. of years, F=(1/n)×MFI, MFI = Modified Fornier Index = $\sum_{i=1}^{12}\frac{P_i^2}{P}$

The percentage of error of the above models are computed with respect to the R factor value of Guwahati calculated by using the half hourly rainfall data i.e 7623 MJmm/ha.h.year

An analysis of Table 6.5 reveals a consistent trend where nearly all existing methods exhibit a notable underestimation of the R factor value. The underestimation of the R factor directly affects the soil loss value as there is a directly proportional relationship between them as per RUSLE. Among the nine methods, the method by L. Xu et al., 2007 shows the highest P.E and the method by Renard & Freimund, 1994 shows the lowest P.E value. The performance of the newly developed equation is found to be quite impressive when compared with these methods. Notably, the newly developed equation outperforms two widely employed Indian methods proposed by Babu et al., 2004 and Singh et al., 1981.

The rainfall pattern of North East India is different from the rest of India. The orographic arrangement of rainfall dominates the rainfall pattern in North East India. Many high-intensity rainfall events occurred in this region, due to which models applicable for other parts of India may fail to produce satisfactory results in this region. As Rainfall erosivity factor is dependent on rainfall intensity, rainfall duration, etc., so it may be the reason that other models are underestimating the R factor when calculated by using the rainfall datasets of Guwahati. Moreover, due to unavailability of new methods, most of the methods taken for comparison in Table 6.5 are old but widely used for various recent studies all over the world (Chatterjee et al., 2014, Devatha et al., 2015, Ganasri & Ramesh, 2016, Joshi et al., 2016, Kayet et al., 2018, A. Kumar et al., 2014, Mondal et al., 2016, Mustefa et al., 2019, S. C. Pal & Chakrabortty, 2019, Prasannakumar et al., 2012, Lifen Xu et al., 2013, Yusof & Ahmad, 2016). The datasets used in developing those models are also old. So, it can be commented that as various climatic parameters are changing over the time hence use of those models in the present time may give an erroneous result. However, in our study, new rainfall data have been employed for development of the empirical equations. Consequently, utilizing these equations for current applications to compute the long-term Rainfall Erosivity Factor (R) may prove advantageous. With this development, the accuracy in soil loss calculation will be enhanced for this region. The accuracy in soil loss calculation is necessary as availability of observed data of soil loss, required for validation of the results, is very scarce.

6.5.2.4 Historical R Factor of the study area

The R factor for the Pamohi watershed was estimated using observed precipitation records for the historical period (1986–2014), obtained from IMD gridded datasets, and computed using Equation 6.17. The mean R factor of the watershed is 7208.64 MJmm/ha.h.year for that period. The maximum and minimum values of R factor are 7389.81 and 6912.84 MJmm/ha.h.year. The mean historical rainfall erosivity factor value is in close agreement with the value of 7623 MJmm/ha.h.year reported for Guwahati City. The findings highlight the reliability and efficiency of the empirical approach adopted in this research for assessing rainfall erosivity. The historical R factor is presented at Figure 6.5.

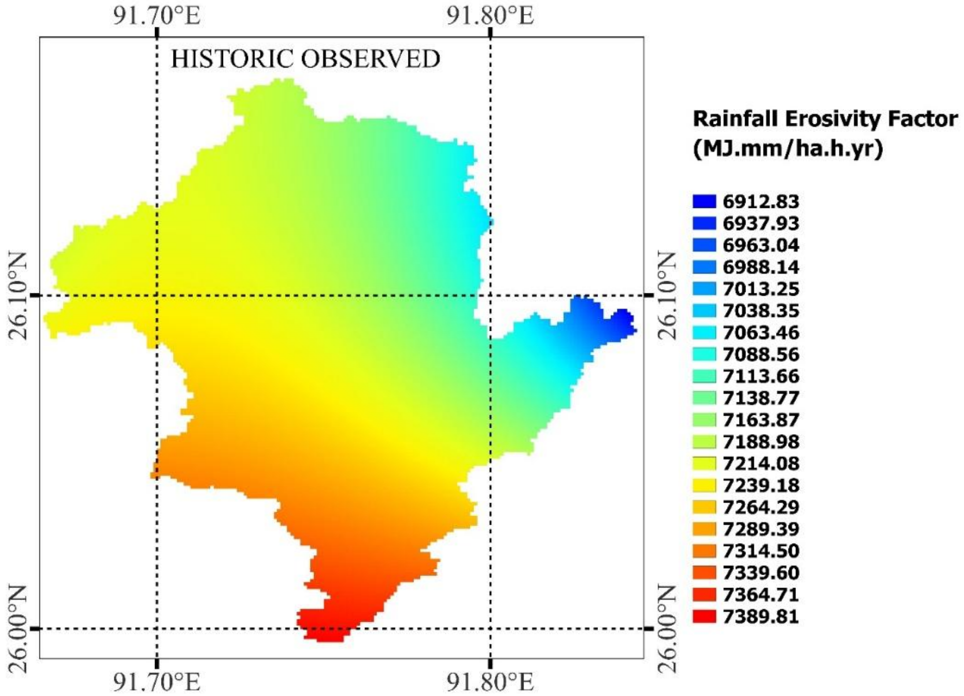

Figure 6.5 Historical Rainfall Erosivity Factor computed by newly developed Empirical equation

6.5.2.5 Performance Analysis of GCMs using various statistical parameters

Thirteen GCMs were assessed for the historical period (1986–2014) by comparing their simulated rainfall erosivity outputs with values derived from observed records. Model performance was evaluated using statistical indicators, Mean Absolute Error (MAE), Root Mean Square Error (RMSE), and Nash–Sutcliffe Efficiency (NSE) and the results are presented in Table 6.6. The MAE ranged from 241.09 to 647.83 MJmm/ha·h·yr, RMSE varied between 313.46 and 765.34 MJmm/ha·h·yr, and NSE values ranged from −0.4 to 0.76. To identify the most reliable models, rankings were assigned for each metric, and models with the lowest combined rank scores were considered as the most accurate and consistent. Based on this analysis, the five highest-ranking models were MPI-ESM1-2_HR, BCC-CSM2-MR, NorESM2-MM, INM-CM5-0, and INM-CM4-8. An ensemble mean generated from these five models was then compared to each of the 13 models and was found to outperform all of them, indicating superior overall accuracy. Consequently, this ensemble mean was adopted for projecting the future R factor of the Pamohi watershed.

Table 6.6 Performance analysis of GCMs using various statistical parameters

Name of GCM	Mean Absolute Error (MAE)	Root Square (RMSE)	Mean Error	Nash-Sutcliffe Efficiency (NSE)	Remarks
ACCESS_CM2	543.93	612.05		0.10	The top five models are MPI-ESM1-2_HR, BCC-CSM2-MR, NorESM2-MM, INM-CM5-0 and INM-CM4-8
ACCESS_ESM1-5	364.07	442.08		0.53	
BCC-CSM2-MR	255.54	319.85		0.75	
CanESM5	309.25	389.47		0.64	
EC-Earth3	439.88	483.17		0.44	
EC-Earth3-Veg	542.81	653.52		-0.02	
INM-CM4-8	310.41	374.10		0.66	
INM-CM5-0	289.49	355.18		0.70	
MPI-ESM1-2-HR	241.09	313.46		0.76	
MPI-ESM1-2-LR	419.37	501.01		0.40	
MRI-ESM2-0	413.47	440.95		0.53	
NorESM2-LM	647.83	765.34		-0.40	
NorESM2-MM	242.48	323.89		0.75	
Ensemble of five best performing models	215.92	310.17		0.77	

6.5.2.6 Projected R Factor

Bias-adjusted daily rainfall data for the projected periods were applied in Equation 10 to compute the rainfall erosivity factor for three future intervals, Near future (2015–2040), Mid future (2041–2070), and Far future(2071–2100) under the SSP245 and SSP585 climate scenarios. The computation was carried out using an ensemble formed from the five top perming GCMs as per Table 6.6.

In the near future period (2015–2040), the projected maximum rainfall erosivity values reached 7599 MJmm/ha.h.yr under SSP245 and 7690 MJmm/ha.h.yr under SSP585. The corresponding minimum values stood at 6824 MJmm/ha.h.yr and 7035 MJmm/ha.h.yr, respectively. As we move into the mid-century (2041–2070), both emission pathways show a further rise: maximum R values increased to 8048 MJmm/ha.h.yr under SSP245 and 8404 MJmm/ha.h.yr under SSP585. Minimum values also climbed to 7442 MJmm/ha.h.yr and 7737 MJmm/ha.h.yr, respectively. The far future (2071–2100) projections suggest a more substantial escalation, with SSP245 showing a maximum of 8177 MJmm/ha.h.yr and SSP585 peaking at 10,235 MJmm/ha.h.yr. The lowest values during this period were 7552 MJmm/ha.h.yr for SSP245 and 9347 MJmm/ha.h.yr for SSP585, confirming the intensifying trend under future climate scenarios. The spatial distribution of projected R factor are presented in Figure 6.6 and Graphical representation of Minimum, Maximum and Mean value R factor are shown in Figure 6.7.

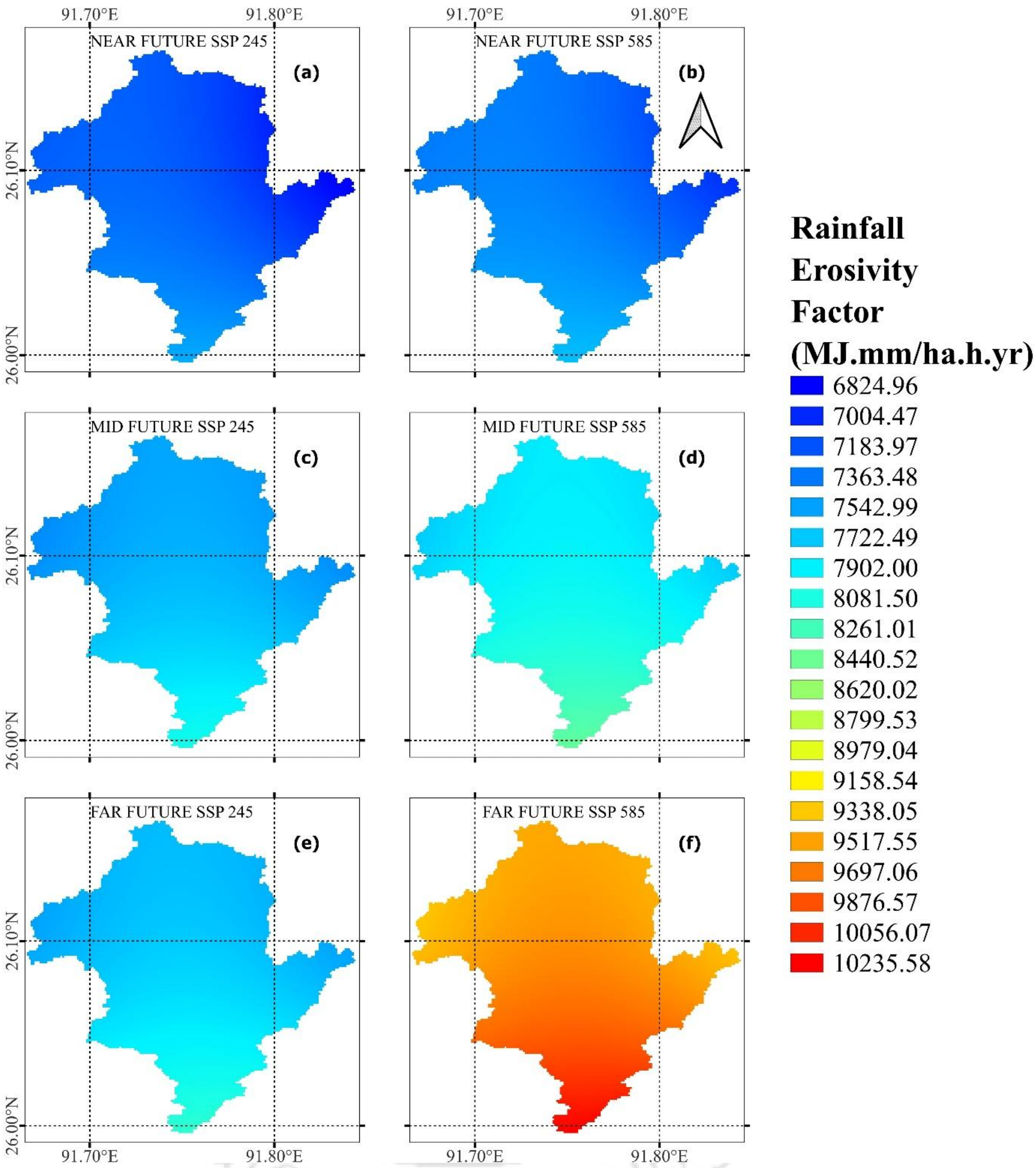

Figure 6.6 The spatial distribution of projected R Factor over different future periods under two CMIP6 climate scenarios

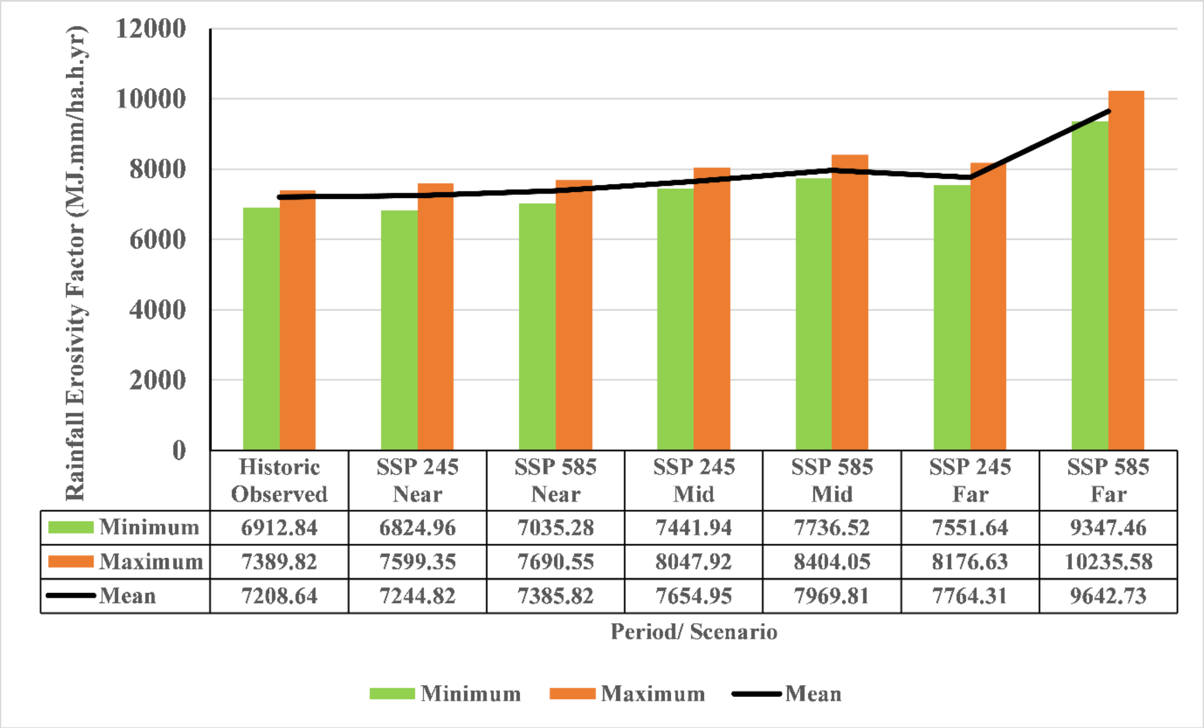

	Historic Observed	SSP 245 Near	SSP 585 Near	SSP 245 Mid	SSP 585 Mid	SSP 245 Far	SSP 585 Far
🟩 Minimum	6912.84	6824.96	7035.28	7441.94	7736.52	7551.64	9347.46
🟧 Maximum	7389.82	7599.35	7690.55	8047.92	8404.05	8176.63	10235.58
― Mean	7208.64	7244.82	7385.82	7654.95	7969.81	7764.31	9642.73

Figure 6.7 Graphical representation of Minimum, Maximum and Mean value Rainfall Erosivity Factor for Historical Period and Projected Rainfall Erosivity Factor under various future scenarios

6.5.2.7 Impact of Climate change on R Factor

For the Pamohi watershed, variations in the rainfall erosivity factor were assessed for three time horizons, Near future (2015–2040), Mid future (2041–2070), and Far future (2071–2100) under the projected scenarios SSP245 and SSP585. These variations were determined by deducting the R factor derived from historical precipitation records from the corresponding R factor values estimated for each future period.

The results demonstrate a consistent increasing trend in the R factor across emission pathways and future timeframes, reinforcing the widely anticipated escalation in erosive potential due to global warming. The empirical approach offers a simplified yet systematic estimation method that does not rely on high-resolution rainfall data, making it suitable for data-sparse regions and large-scale policy assessments.

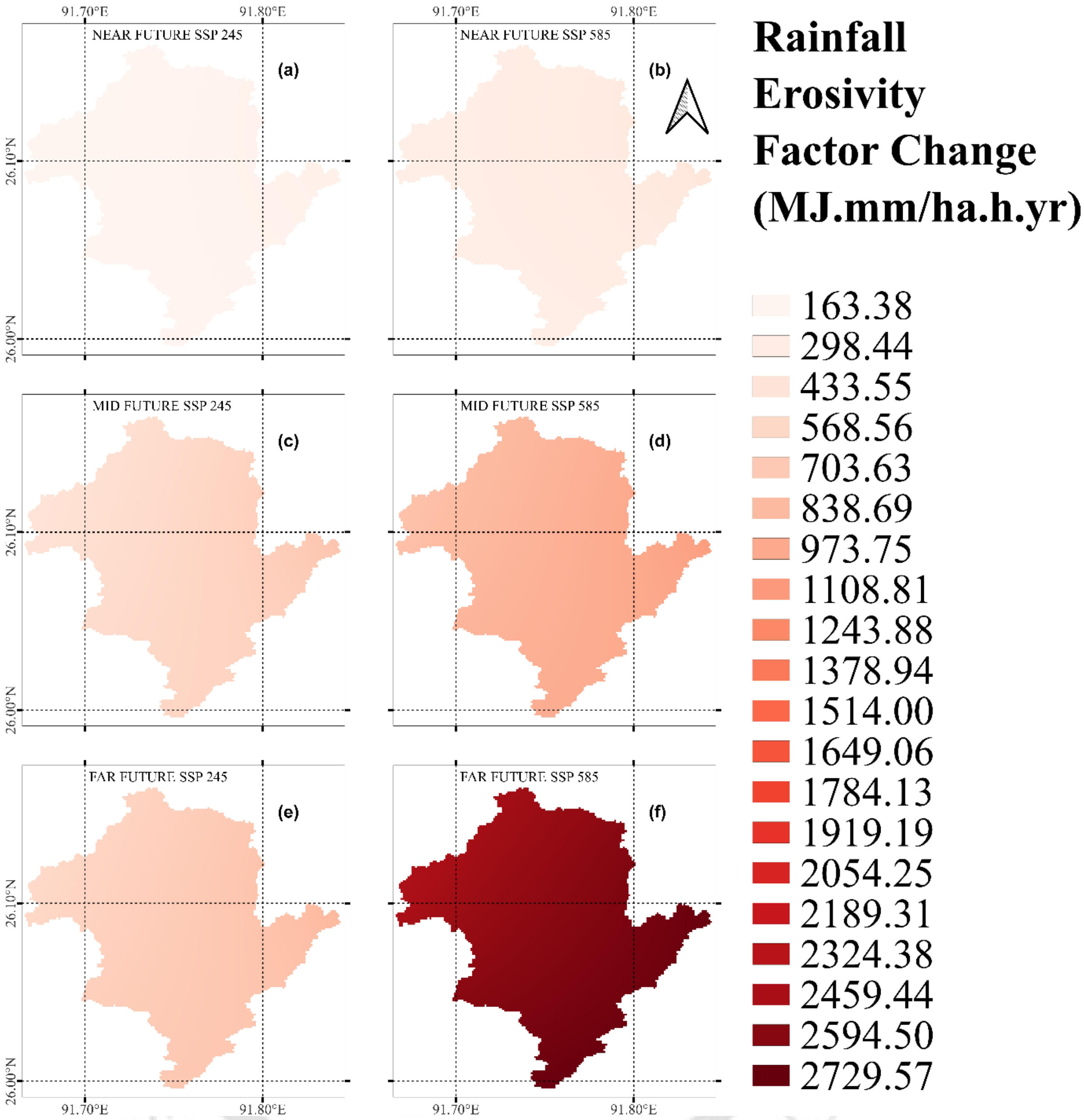

Figure 6.8 The spatial distribution of changes in R Factor over different future periods under two CMIP6 climate scenarios relative to historical period.

Our model projects a mean increase in the R factor of 192 MJ.mm/ha.h.yr under SSP 245 and 307 MJ.mm/ha.h.yr under SSP 585 during near future period. This upward trend becomes more pronounced in the mid future period (2041–2070), where the mean changes escalate to 575 MJ.mm/ha.h.yr for SSP 245 and 910 MJ.mm/ha.h.yr for SSP 585. In the far future period (2071–2100), the projections indicate a substantial rise in mean values, with an increase of 686 MJ.mm/ha.h.yr under SSP245 and a much higher increase of 2595 MJ.mm/ha.h.yr under SSP585. The spatial distribution of changes in R Factor over different future periods under climate change scenarios is presented in Figure 6.8.

6.6 Effect of Climate Change on Rainfall Erosivity Factor through Rainfall Disaggregation

6.6.1 Methodology

6.6.1.1 Rainfall Disaggregation

In NEOPRENE python Library, Neyman-Scott process is used to generate synthetic sub-daily rainfall data. The rainfall generation can be sub-divided into two steps i) Calibration and ii) Simulation, which are also the sub-libraries of NEOPRENE. The calibration process plays a crucial role in identifying the optimal set of parameters that accurately replicate the statistical characteristics of the given input data series. This step generates the finely tuned parameters required for effective simulation. NEOPRENE achieves this by employing Particle Swarm Optimization (PSO) to refine model parameters, ensuring that the modelled statistics closely align with the observed data. The optimization is carried out by minimizing the weighted Euclidean distance between the statistical properties of the observed and simulated datasets (Gad, 2022).

In the Calibration step several hyperparameters are set and the observed daily data are import to the calibrator. In the simulation step, a simulated time series of rainfall is generated with the help of the set of parameters received from the calibration step and the suitable hyperparameters. During the simulation process, users must specify the temporal extent of the generated rainfall series. The hyperparameters are not a part of Neyman Scott Process, however these parameters are needed to configure the calibration and simulation process. The knowledge about various information related to the rainfall of the area is required to set these hyperparameters. The hyperparameters for calibration step are seasonality type, seasonality user, temporal resolution, process, statistics, weights, number of iterations, cell intensity, number of bees, time between storms, number of storm cells, storm cell displacement, cell duration and number of initializations. The hyperparameters for simulation step are seasonality type, seasonality user, statistics, temporal resolution, process, initial year and final year.

There is also a third sub-library called "Analysis", which consist of several functionalities like comparison of simulated series with the observed series, daily to hourly rainfall disaggregation etc. The "disaggregate_rainfall" function of Analysis sub-library performs the disaggregation process. The function looks for a similar day in the synthetic time series, for each day to be disaggregated. To enhance the accuracy of the disaggregation process, data from the preceding day is also considered in the selection criteria. The approach involves identifying a sequence of days that exhibit the smallest Euclidean distance between the observed and synthetically generated data series. These selected days are then utilized as reference points to refine and improve the disaggregation procedure. Further details of the Neyman Scott Process and NEOPRENE python library can be found in (Diez-Sierra et al., 2023).

6.6.1.2 Rainfall Erosivity Factor

In the second approach the temporal resolution of the disaggregated rainfall is hourly, thus the term I_{30} has to be replaced by I_{60} in the Equation 6.8. Now, I_{60} is the maximum 60 minute intensity (mm/hr) of erosive rainfall event. Raj et al. (2022) also used I_{60} in place of I_{30} to compute the rainfall erosivity map of India using IMDAA hourly rainfall data. To derive the equivalent rainfall erosivity, the erosivity estimates initially obtained from 60-minute rainfall data were adjusted by applying a conversion factor of 1.79 (Das and Jain, 2023).

6.6.1.3 Performance Evaluation of GCM

The rainfall erosivity factor for the historical period (1986 to 2014) was estimated by the bias corrected CMIP6 model data of all the 13 GCMs given in Table 6.7. The rainfall erosivity factor estimated from all 13 GCMs was evaluated against the values obtained from the observed gridded rainfall datasets provided by the India Meteorological Department (IMD). This comparison was conducted for the historical period extending from 1986 to 2014 to assess the accuracy and reliability of the model projections. The following widely used statistical metrics are selected for evaluating the performance of GCM, Nash-Sutcliffe efficiency (NSE), Root mean square error (RMSE), Mean absolute error (MAE) and Percent bias (PBIAS) (Equation 6.2, 6.3, 6.5 and 6.6). These parameters will be employed to identify the five best-performing GCMs, as already discussed that utilizing an ensemble of well-performing models is known to reduce uncertainties in future projections.

To identify the top five best-performing GCMs, a robust multi-metric evaluation framework was employed. Four key statistical performance metrics as mentioned above were computed by comparing rainfall erosivity values derived from the historical simulations of 13 GCMs with those calculated using observed data. Each model was ranked individually for every metric, and a cumulative score was obtained by summing these ranks. GCMs with the lowest total scores were shortlisted. An additional constraint was imposed to enhance the reliability of the selection, that only models with an NSE value greater than 0.5 were considered eligible. This rigorous, criteria-driven process led to the selection of five GCMs that most effectively captured the historical rainfall erosivity patterns of the Pamohi watershed and these were subsequently applied for future projections. The methodological flowchart of the study is given in Figure 6.9.

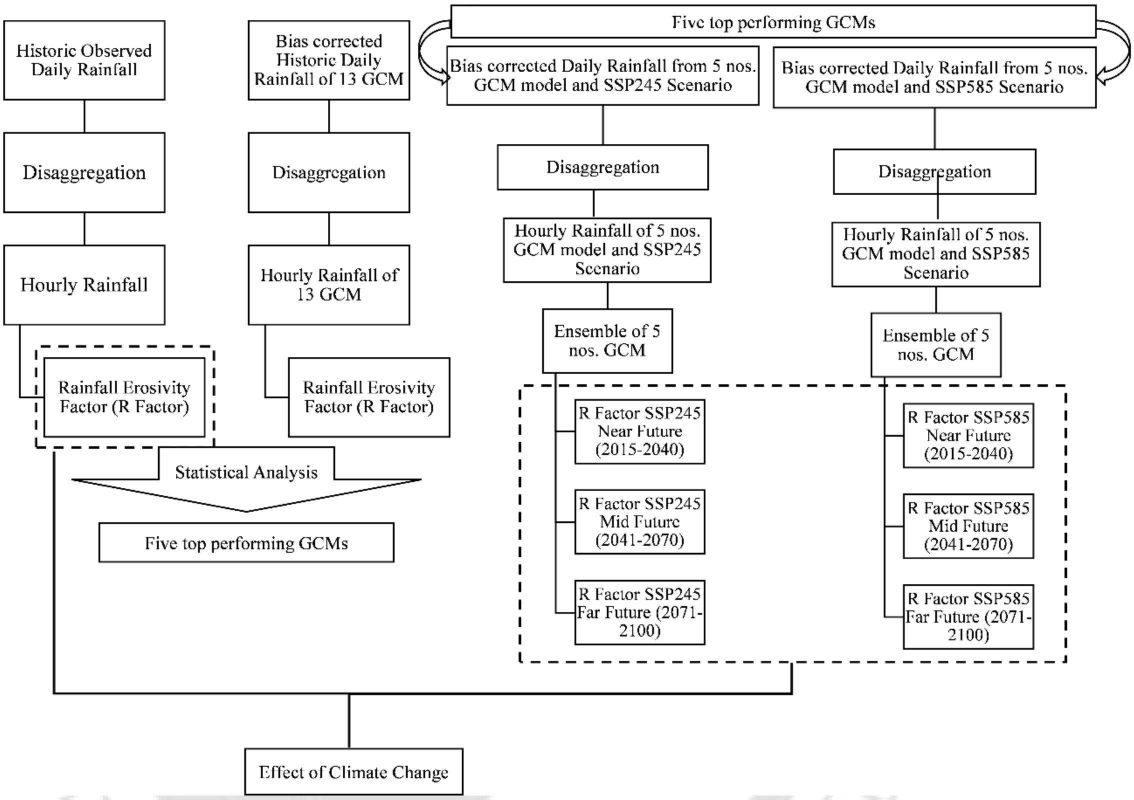

Figure 6.9 Methodological Flow chart of modelling effect of climate change on Rainfall Erosivity Factor

6.6.2 Results and Discussions

6.6.2.1 Performance Evaluation of GCMs

The performance of thirteen GCMs was evaluated over the historical period by comparing simulated rainfall erosivity values with those derived from observed data. Four statistical metrics PBIAS, MAE, RMSE and NSE were used to assess the accuracy of each model. Table 6.7 presents the performance of each GCM along with the calculated values of these metrics. The analysis revealed significant variability in model performance. PBIAS values ranged from –17.07% (MPI-ESM1-2-LR) to +3.76% (EC-Earth3-Veg), indicating the degree of underestimation or overestimation in the simulated values. The MAE and RMSE varies from 554 MJ.mm/ha.h.yr (MRI-ESM2-0) to 1489 MJ.mm/ha.h.yr (NorESM2-LM) and 662 MJ.mm/ha.h.yr (MRI-ESM2-0) to 1547 MJ.mm/ha.h.yr (NorESM2-LM) respectively, indicating varying degrees of alignment between simulated and observed rainfall erosivity values. NSE values varied widely from –4.10 to 0.82. Only five models MRI-ESM2-0, MPI-ESM1-2-HR, INM-CM5-0, ACCESS_ESM1-5, and CanESM5 exceeded the NSE threshold of 0.5, marking them as statistically acceptable for reliable projections. To determine the top performing models, the multi-metric evaluation framework was applied. Each model was ranked across all four metrics, and models with the lowest total scores were considered the most consistent and accurate. Applying the additional criterion of NSE > 0.5, five GCMs were shortlisted. These models not only demonstrated high agreement with historical erosivity values but also satisfied all performance thresholds, justifying their inclusion in the ensemble.

Table 6.7 Performance analysis of GCMs using various statistical parameters (Rainfall Disaggregation)

Name of GCM	Percent Bias (%)	Mean Absolute Error (MAE)	Root Mean Square Error (RMSE)	Nash-Sutcliffe Efficiency (NSE)	Remarks
ACCESS_CM2	-16.06	1152	1285	-0.36	The five best performing models are MRI-ESM2-0, MPI-ESM1-2-HR, INM-CM5-0, ACCESS_ESM1-5 and CanESM5
ACCESS_ESM1-5	1.42	655	733	0.56	
BCC-CSM2-MR	0.93	615	810	-0.16	
CanESM5	2.84	785	885	0.54	
EC-Earth3-Veg	3.76	736	829	0.30	
EC-Earth3	0.83	946	1054	0.47	
INM-CM4-8	-13.83	992	1282	-0.81	
INM-CM5-0	-3.98	951	1151	0.60	
MPI-ESM1-2-HR	-9.26	664	790	0.63	
MPI-ESM1-2-LR	-17.07	1225	1529	-4.10	
MRI-ESM2-0	2.40	554	662	0.82	
NorESM2-LM	-2.63	1489	1547	0.34	
NorESM2-MM	-15.66	1124	1166	0.04	
Ensemble of five best performing models	-1.31	334	401	0.90	

To reduce uncertainty and improve projection reliability, an ensemble was created by averaging outputs from the five selected GCMs. The statistical performance of this ensemble significantly outperformed individual models across all metrics. The ensemble achieved a PBIAS of -1.31%, MAE of 334, RMSE of 401, and an NSE of 0.90 indicating near-optimal alignment with observed erosivity data. This improvement confirms the findings of Eekhout and de Vente (2022), who emphasized the advantage of using multi-model ensembles in soil erosion assessments under climate change. The ensemble approach effectively balances variability across models, resulting in a more stable and robust projection framework by reducing model-specific biases and errors.

6.6.2.2 Historical R Factor

The R factor was calculated by 29 years observed historical precipitation product (1986 to 2015). The R factor was also calculated by average historical precipitation data of ensemble of the five top performing GCMs for the same time period. The spatial distribution of historical rainfall erosivity determined from both datasets is illustrated in Figure 6.10**.** The mean of rainfall erosivity factor are 7130 and 7106 MJ.mm/ha.h.yr calculated by observed historical precipitation and average historical precipitation data of ensemble of GCM respectively. The maximum values of R factor are 7674 and 7632 MJ.mm/ha.h.yr and minimum values of R factor are 6675 and 6797 MJ.mm/ha.h.yr calculated by observed historical precipitation and average historical precipitation data of ensemble of GCM respectively. The difference in mean of the R factor by the two historical precipitation dataset is only 14 MJ.mm/ha.h.yr, which implies a great matching. The historical rainfall erosivity value calculated in this study closely aligns with the value of 7623 MJ.mm/ha.h.yr reported by Das and Sarma (2021) for Guwahati City, which was derived using 19 years of observed half-hourly rainfall data. This agreement underscores the reliability and effectiveness of the disaggregation method employed in this study for estimating rainfall erosivity, adhering to the standard methodology outlined in the RUSLE handbook.

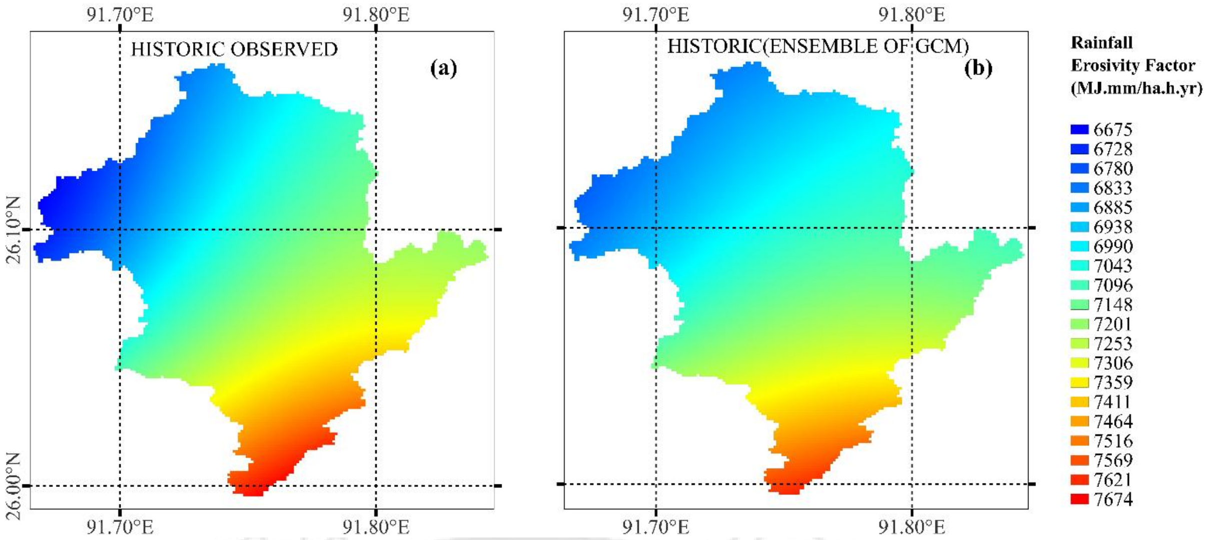

Figure 6.10 Rainfall Erosivity Factor for the historical period (1986 to 2014) using (a) observed historical precipitation product and (b) average historical precipitation data of ensemble of the five top performing GCMs

6.6.2.3 Future Rainfall Erosivity

The bias corrected daily precipitation of the future periods has been disaggregated to hourly interval and estimated the rainfall erosivity factor for the three future periods viz. Near Future (2015 to 2040), Mid Future (2041 to 2070) and Far Future (2071 to 2100) under SSP 245 and SSP 585 by the standard method as per RUSLE hand book. The rainfall erosivity factor has been estimated for ensemble of five top performing GCMs. The spatial distribution of rainfall erosivity factor of Pamohi watershed for three future periods under two CMIP6 projected pathways is shown in Figure 6.11.

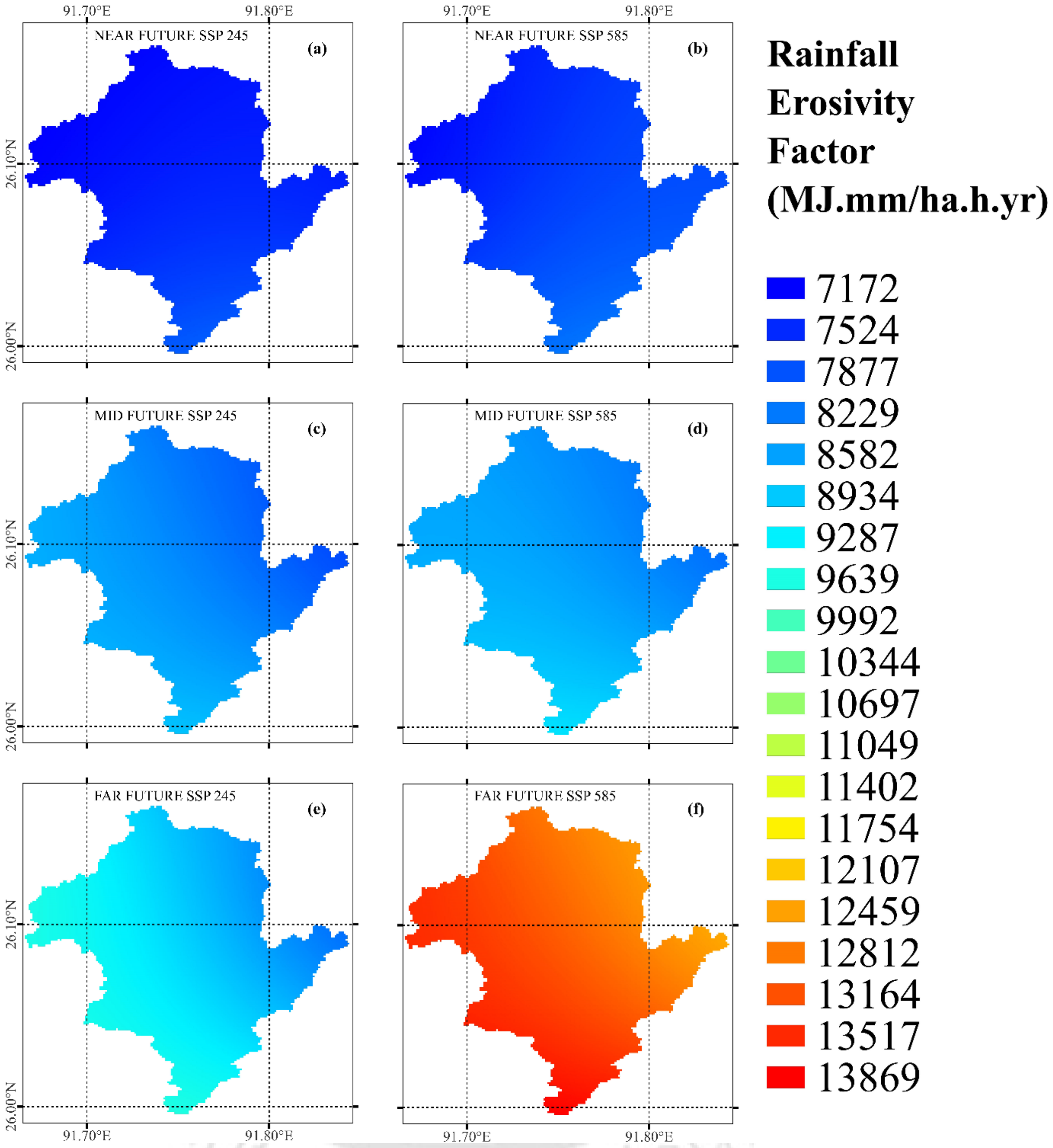

Figure 6.11 Rainfall Erosivity Factor for (a) Near future under SSP245, (b) Near future under SSP585, (c) Mid future under SSP245, (d) Mid future under SSP585, (e) Far future under SSP245 and (f) Far future under SSP585 projected pathway

For the near future period, the maximum rainfall erosivity values were observed as 7994 MJ.mm/ha.h.yr under SSP 245 and 8203 MJ.mm/ha.h.yr under SSP 585. Correspondingly, the minimum values recorded were 7172 MJ.mm/ha.h.yr for SSP 245 and 7211 MJ.mm/ha.h.yr for SSP 585. During the mid future period, the maximum rainfall erosivity values increased to 8890 MJ.mm/ha.h.yr and 9161 MJ.mm/ha.h.yr under

SSP 245 and SSP 585, respectively. The minimum values similarly rose to 7821 MJ.mm/ha.h.yr and 8145 MJ.mm/ha.h.yr under the respective pathways. In the far future period, a pronounced escalation in rainfall erosivity was evident. The maximum values reached 9683 MJ.mm/ha.h.yr under SSP 245 and 13869 MJ.mm/ha.h.yr under SSP 585. Likewise, the minimum values attained were 8161 MJ.mm/ha.h.yr and 12400 MJ.mm/ha.h.yr under SSP 245 and SSP 585, respectively. Figure 6.12 represents the overall summary of both historical and future rainfall erosivity factors.

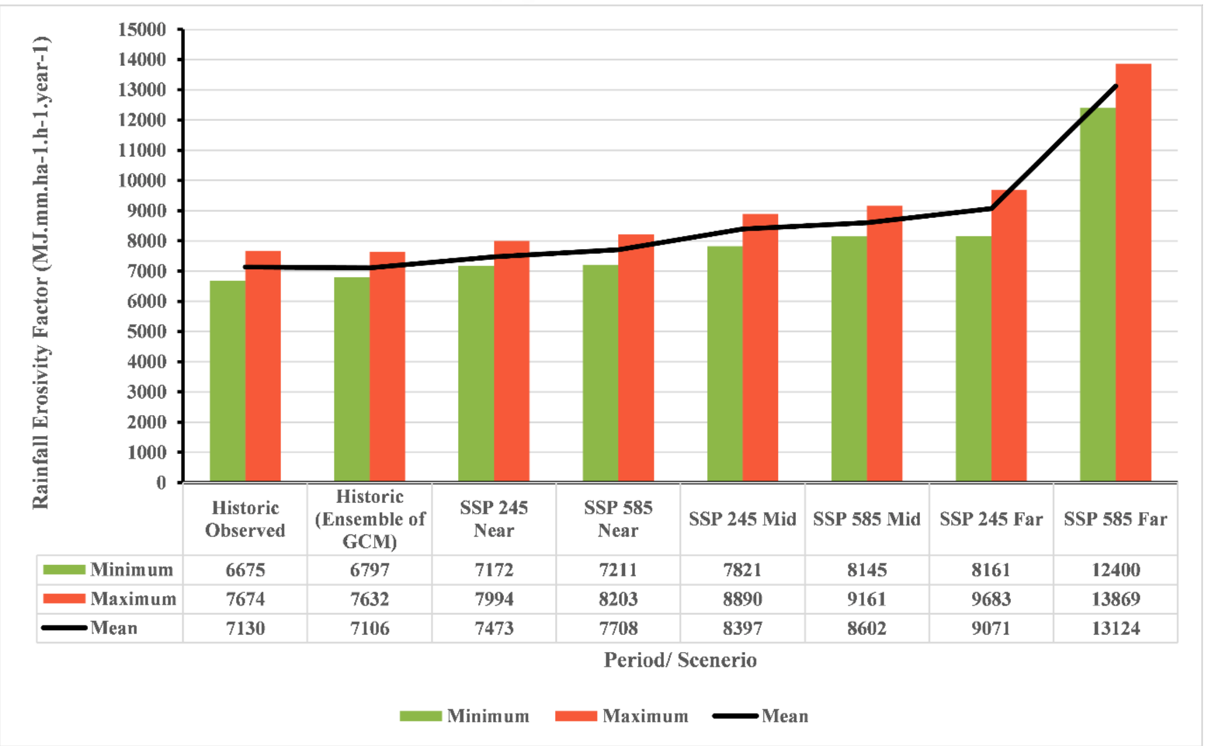

	Historic Observed	Historic (Ensemble of GCM)	SSP 245 Near	SSP 585 Near	SSP 245 Mid	SSP 585 Mid	SSP 245 Far	SSP 585 Far
🟩 Minimum	6675	6797	7172	7211	7821	8145	8161	12400
🟥 Maximum	7674	7632	7994	8203	8890	9161	9683	13869
▬ Mean	7130	7106	7473	7708	8397	8602	9071	13124

Figure 6.12 Minimum, Maximum and Mean value of Rainfall erosivity factor (MJ.mm/ha.hr.yr) for historical and future periods under two projected pathways

6.6.2.4 Climate change effect on Rainfall Erosivity Factor

The spatial distribution of change in rainfall erosivity factor of Pamohi watershed Near Future (2015 to 2040), Mid Future (2041 to 2070) and Far Future (2071 to 2100) periods under SSP 245 and SSP 585 projected pathways is shown in Figure 6.13. The change in rainfall erosivity factor is calculated by subtracting the R Factor estimated by observed historical precipitation from the R factor of future periods.

In the near future period, the mean changes in the R Factor are projected to be 344 MJ.mm/ha.h.yr under SSP 245 and 579 MJ.mm/ha.h.yr under SSP 585. For the mid future period, these values are expected to increase significantly, reaching 1267 MJ.mm/ha.h.yr under SSP 245 and 1472 MJ.mm/ha.h.yr under SSP 585. The far future period shows the most pronounced changes, with mean R Factor increases of 1941 MJ.mm/ha.h.yr under SSP 245 and a striking 5994 MJ.mm/ha.h.yr under SSP 585. These results indicate a progressive intensification in the mean R Factor over time, with substantially higher increases under SSP 585, particularly in the far future, underscoring the potential impact of high-emission scenarios on rainfall erosivity.

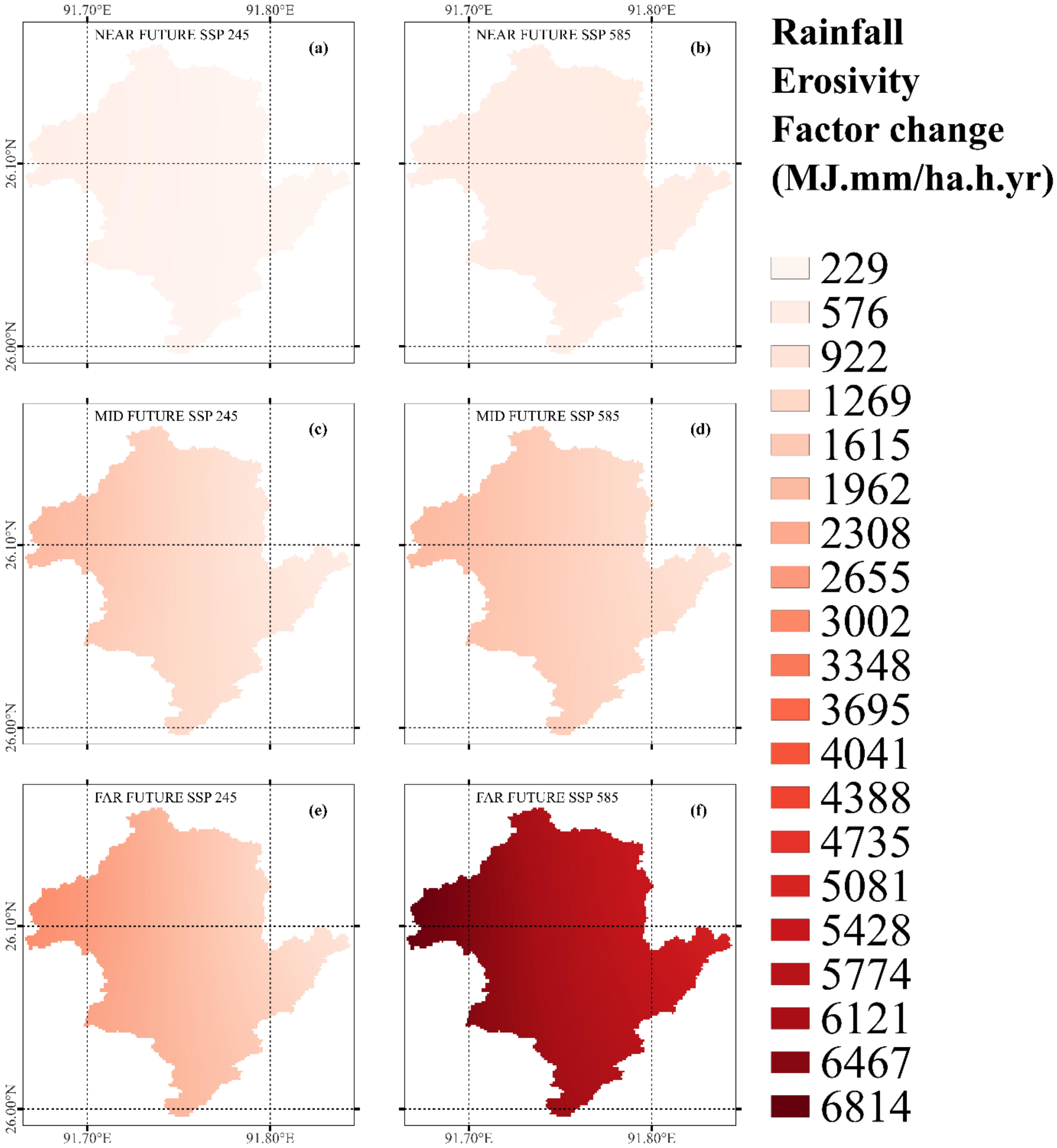

Figure 6.13 Change in Rainfall Erosivity Factor over Pamohi watershed in (a) Near future under SSP245, (b) Near future under SSP585, (c) Mid future under SSP245, (d) Mid future under SSP585, (e) Far future under SSP245 and (f) Far future under SSP585 projected path

In their study, Das and Jain (2023) reported minimal changes in the R Factor for our study area during 2015-2040, with values appearing to be below their lowest range of 500 MJ.mm/ha.h.yr. During 2041-2070, they identified R Factor changes in the range of 1000–2500 MJ.mm/ha.h.yr for this area. The values were identified through visual analysis of maps. However, their study did not extend for 2071–2100. Our findings corroborate these observations for 2015-2040 and 2041-2070. Specifically, during 2015-2040, the change in R Factor in our study was consistently below 500 MJ.mm/ha.h.yr across all points. Similarly, during 2041-2070, the changes in R Factor predominantly fell within the range of 500–2500 MJ.mm/ha.h.yr, aligning with the estimates by Das and Jain (2023). For 2071–2100, our analysis revealed a significant escalation in R Factor changes, ranging approximately from 500 to 7500 MJ.mm/ha.h.yr.

6.7 Comparison of the two methods with each other and with findings from other studies

In this study two approaches have been used to estimate rainfall erosivity factor under changing climate scenarios. Both approaches consistently showed an increasing trend in the rainfall erosivity factor, particularly under high-emission scenarios, though they differed in magnitude and sensitivity.

The disaggregation method, which generates high-resolution rainfall data from daily rainfall data, was found to be more responsive to extreme rainfall events. Under SSP 585 in the far future (2071–2100), it projected a mean R factor increase of 5994 MJ.mm/ha.h.yr (84.07%), compared to 2595 MJ.mm/ha.h.yr (33.77%) from the empirical equation. Even in the near future (2015–2040), differences were evident, the disaggregation approach projected increases of 4.81% (SSP245) and 8.20% (SSP585), while the empirical model estimated only 0.50% and 2.46%, respectively. The Figure 6.14 and Figure 6.15 are presenting line diagram of percentage change of R factor by both the methods.

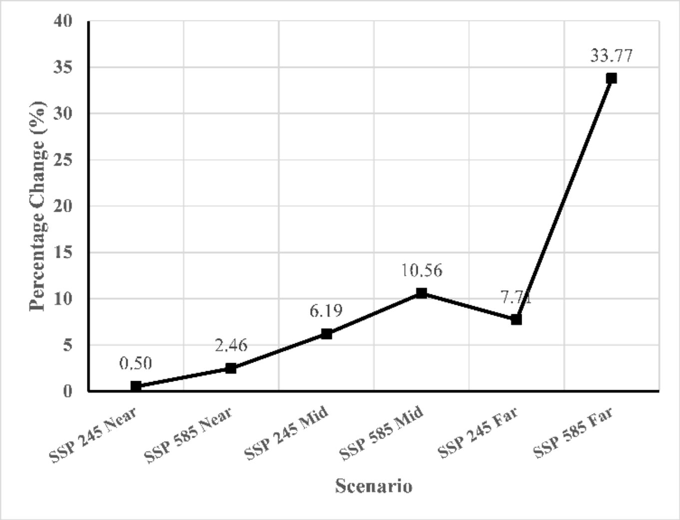

Figure 6.14 Line chart showing the change in Rainfall Erosivity Factor estimated for three future periods, Near Future (2015 to 2040), Mid Future (2041 to 2070) and Far Future (2071 to 2100) under SSP 245 and SSP 585 projected pathways through empirical equation

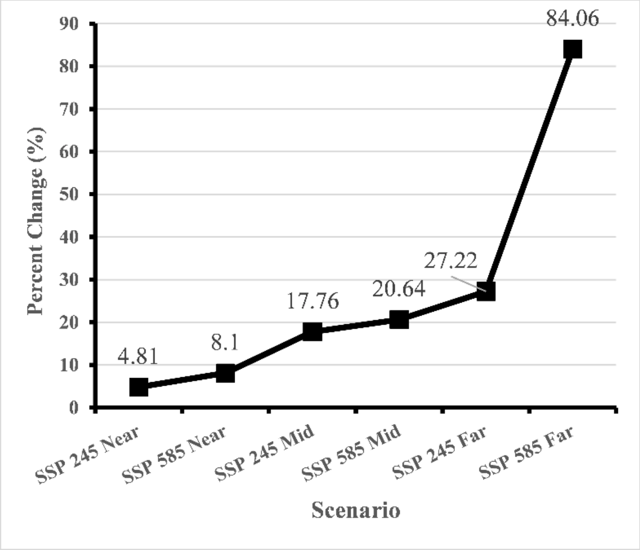

Figure 6.15 Line chart showing the change in Rainfall Erosivity Factor estimated for three future periods, Near Future (2015 to 2040), Mid Future (2041 to 2070) and Far Future (2071 to 2100) under SSP 245 and SSP 585 projected pathways through rainfall disaggregation

Comparisons with previous studies provide important context for interpreting these results. At the national scale, Das and Jain (2023) reported mid future increases of 22% (SSP245) and 31% (SSP585), which align closely with the mid-future disaggregation projections for the Pamohi watershed (17.77% and 20.64%). The empirical model is directionally consistent but remained more conservative (6.19% and 10.56%). At the regional scale, Islam and Chakma (2024) observed sharp increases in the Jhelum catchment (14.87% under SSP245, 94.24% under SSP585 by 2090). These values show the same rising pattern as the disaggregation method and emphasize the increased sensitivity of Himalayan basins to climate change, however, they exceed the empirical projections considerably. Importantly, these findings are not contradictory but rather illustrate the regional amplification of rainfall extremes compared to national or global averages. Similarly, Mondal et al. (2016) reported increasing rainfall erosivity trends in the Narmada basin, supporting that both the direction and scale of change observed in the present study are consistent with other Indian catchments. At the global scale, Panagos et al. (2022) projected increases of 27–34.3% by 2070 under various RCP scenarios. The disaggregation method results for the mid future (17.77%–20.64%) fall within this global range and the empirical model remains at the lower end.

Overall, the evidence suggests that the empirical model is computationally efficient, easy to use and suitable for large-scale or data-limited applications, but it tends to smooth the data and does not capture localized peaks in erosivity. This makes it particularly valuable for early-stage impact assessment and decision-making processes where data or computational resources are limited. On the other hand, the rainfall disaggregation approach demonstrates a superior ability to capture extremes, making it highly suitable for detailed erosion risk assessments and identifying erosion hotspots in climate-sensitive regions.

6.8 Conclusion

This study provides a comprehensive evaluation of how climate change influences rainfall erosivity in the Pamohi watershed, the primary watershed of “Deepor Beel”, the only major storage waterbody for the Guwahati city’s drainage. A key contribution of this research is the development of a Multiple Linear Regression (MLR) model based empirical equation that estimates the Rainfall Erosivity Factor using readily available daily rainfall data. The newly developed equation outperformed existing empirical approaches and was subsequently used to project future rainfall erosivity under different climate scenarios. Climate projections were carried out for three future time periods near future (2015-2040), mid future (2041-2070) and far future (2071-2100) under two projected pathways SSP245 and SSP585 under CMIP6 socioeconomic pathway. Both the empirical equation and disaggregation-based approach indicate a clear upward trend in rainfall erosivity factors across all scenarios. The disaggregation method captured more pronounced increases, while the empirical model provided a conservative estimate of the general trend. Historical validation showed strong agreement with observed rainfall data.

The outcomes of this study hold significant practical implications. They can be applied directly to estimate soil loss under changing climate conditions and provide critical guidance for designing soil conservation measures. Additionally, the results will inform flood mitigation planning for Guwahati City and support broader watershed management and climate adaptation strategies.

Chapter 7

Conclusion and Recommendation for Future work

7.1 A brief summary of the work performed

The present research comprehensively investigates the spatial and temporal variability of the Rainfall Erosivity Factor (R factor) across India using satellite-based rainfall datasets. The study first developed a high-resolution (0.1°) rainfall erosivity map of India using half-hourly IMERG data (2001–2020). The analysis quantified spatial heterogeneity, seasonal variability, and long-term trends in erosivity. It uncovers significant regional differences primarily controlled by rainfall patterns and terrain condition. The research also incorporated the concept of return period analysis to assess erosivity corresponding to various return periods. This novel approach provides a more realistic representation of soil loss potential under high erosive events, which enabling improved design criteria for soil conservation and watershed management structures. Further, the study carried out a calibration of the IMERG precipitation dataset using the IMD daily gridded rainfall data. It used a modified version of Daily Spatio-Temporal Disaggregation Calibration Algorithm (DSTDCA). The calibrated product is named as IMDMERG and it was used to regenerate the R factor map of the study area. The new map revealed additional zones of high rainfall erosivity in the study area. Finally, the study assessed the impact of future climate change on rainfall erosivity using CMIP6 projections under two Shared Socioeconomic Pathways viz. SSP245 and SSP585. The future rainfall erosivity was estimated using two approaches: (i) through a Multiple Linear Regression (MLR) model developed using daily rainfall data and (ii) by disaggregating daily rainfall into sub-daily intervals to compute the R factor following the standard procedure outlined in the RUSLE handbook. The results from both the methods showed a consistently increasing trend in the projected R factor for the Pamohi watershed under both scenarios.

7.1.1 Preparation of Rainfall Erosivity Map and its analysis of spatiotemporal variation

This chapter systematically presented the methodology, results, and in-depth analysis of the rainfall erosivity factor (R factor) across mainland India (excluding Ladakh). The study used 20 years (2001–2020) high temporal resolution satellite rainfall data from IMERG. This study successfully generated a high spatial resolution R factor map by implementing the methodology outlined in the RUSLE handbook and using IMERG half-hourly rainfall data. The map supports a detailed spatiotemporal understanding of rainfall erosivity across the study area.

The spatial distribution of the average annual R factor reveals significant variability caused by regional climatic conditions and orographic effects. The overall spatial average of the R factor across India is 2188.79 MJ.mm/ha.h.year, with values ranging from a minimum of 68.28 MJ.mm/ha.h.year in the cold and arid Lahul and Spiti region of Himachal Pradesh to a maximum of 18,864.2 MJ.mm/ha.h.year in Lakhimpur district of Assam. The major erosivity hotspots are located predominantly in North East India and the Western Ghats. The steep terrains of these regions and frequent intense rainfall events amplify rainfall erosivity via orographic lifting mechanisms.

The comparative analysis between the IMERG-based R factor and previously developed ground-based R factor maps offered crucial validation and insight into the robustness of satellite data. Specifically, comparison with the Panagos et al. (2017) global ground-based R factor map revealed that the IMERG-based mean R factor was approximately 58% of the ground-based mean during the common period (2007–2015). Spatial discrepancies were particularly present in regions like Meghalaya and the Western Ghats, where IMERG tended to capture high erosivity zones that the ground-based map missed. This may be due to limitations in rain gauge density and interpolation errors.

The study further validated the IMERG-based R factor through comparison with the historical Isoerodent map of India by Babu et al. (1978). Despite the temporal gap and limited gauge network used in the earlier map, the spatial patterns were found to broadly agree. However, the variations in magnitude can be attributed to the use of recent high-resolution satellite datasets, which effectively capture recent shifts in rainfall patterns and technological improvements in data quality. A detailed station-level comparison of IMERG based R factor was performed with the data of one IMD rain gauge station near Guwahati. The IMERG derived average R factor was about 10% higher than the station-based value. Although an anomalous year (2007) was observed, where the ground station indicated a sharp decrease while IMERG data showed an increase, however the overall temporal trend remained well aligned.

A non-dimensional R factor map was developed by normalizing the computed R factor values relative to the spatial mean to provide a generalized perspective. The results revealed that most of the area (63.48%) exhibiting values below the mean. This non-dimensional map serves as a powerful analytical tool to assess relative vulnerability across different regions independent of absolute magnitudes. The monthly analysis of the R factor highlighted distinct spatiotemporal patterns that closely follow the Indian monsoon dynamics. Erosivity was minimal during January and February, slowly increases during the Pre-Monsoon months (March–May). The Southwest Monsoon period (June–September) emerged as the most erosive phase, contributing the bulk of the annual erosivity. July exhibited the highest monthly mean erosivity (655.17 MJ.mm/ha.h.month) and maximum values exceeding 5792.10 MJ.mm/ha.h.month. Conversely, October to December (Post-Monsoon) demonstrated a spatial shift in erosivity hotspots towards coastal regions due to the Northeast Monsoon, especially affecting Tamil Nadu, Andhra Pradesh, and Kerala. These monthly insights emphasize the critical need to capture intra-annual variability for policy planning and soil conservation efforts. Seasonal analysis supported these findings and showed that the Southwest Monsoon was the dominant erosivity season contributing the largest spatial extent and magnitude of the R factor across India. Winter exhibited negligible erosivity with only sparse contributions from localized precipitation. Pre-monsoon and post-monsoon seasons had moderate spatial coverage of erosivity, largely concentrated in North East India and specific coastal regions.

Over the long term from 2001 to 2020 the spatial pattern of the R factor remained broadly stable but showed significant interannual variability. The R factor reached its highest peak in 2007 due to an exceptionally active monsoon phase while other years showed no clear long-term increasing or decreasing trend. A slight overall decreasing trend in the average annual R factor was observed. The application of the Modified Mann-Kendall test for trend analysis revealed that only 13.86% of the study area showed statistically significant trends, among which 12.04% significant decrease and 1.82% significant increase. Significant increasing trends were mainly observed in Rajasthan and parts of Northeast India. However, the Rajasthan region generally showed low absolute R factor values which indicates that the direction of the trend does not necessarily reflect the magnitude of its impact. The majority of the area (87%) showed no significant trend, confirming inter-annual fluctuations of rainfall erosivity in India. The study enhances the understanding of spatiotemporal variability of erosivity and offers vital insights for policymakers, researchers, and land managers focused on sustainable soil and water resource management.

7.1.2 Incorporating return period in the assessment of rainfall erosivity factor over India

The current research offers valuable findings regarding the analysis of the R factor in India corresponding to various return periods. The methodology of this study combines the standard procedure of frequency analysis with the R factor calculation method from the RUSLE handbook to estimate and map the rainfall erosivity factor. The R factor was computed using 20 years IMERG 0.1 degree spatial resolution satellite rainfall data having a 30 minute temporal resolution, spanning from 2001 to 2020. The mean annual R factor values for India corresponding to 2, 5, 10, 25, 50 and 100 year return periods were 1918.94, 2963.84, 3795.55, 4916.79, 5487.89 and 5806.90 MJ.mm/ha.h, respectively. The maximum values of the annual R factor for India were 18,556.12, 25,598.15, 35,815.77, 46,113.28, 49,545.78 and 51,262.03 MJ.mm/ha.h for the corresponding return periods.

Moreover, the analysis revealed that the mean annual R factor fell within the return level range of the 2 and 5 year return periods in 94.96% of cases. The spatial average R factor value of the study area also aligned with this range. The majority of the cases having the maximum annual R factor correspond to a return period range of 25 to 50 years. The country average of the maximum annual R factor value was found to be closer to the 50 year return period. Furthermore, it was observed that areas with the same average R factor value could exhibit significant differences in their return levels values corresponding to various return period. Consequently, relying solely on the average annual R factor would underestimate the soil loss potential of an area.

This study will contribute to enhance knowledge in the field of soil loss assessment and can be instrumental in the design and application of effective soil conservation measures and control structures. Stakeholders and policymakers will benefit from the flexibility to select specific return periods for designing soil conservation structures based on their specific requirements.

7.1.3 Calibration of IMERG dataset using IMD daily gridded dataset for computing Rainfall Erosivity Factor

The calibration of the IMERG dataset using the IMD daily gridded precipitation dataset marks a significant advancement in improving satellite precipitation products for hydrological research. The chapter clearly showed that satellite precipitation estimates provide detailed information across time and space. However, they need careful adjustment using ground-based observations to reduce biases and uncertainties. The study used a modified version of the Daily SpatioTemporal Disaggregation Calibration Algorithm (DSTDCA). The method combined the temporal richness of IMERG with the spatial reliability of IMD daily rainfall to create a refined high-resolution precipitation dataset named IMDMERG.

The results of this calibration indicate substantial improvements in the agreement between satellite-derived and gauge-based precipitation data. The IMERG Final satellite gauge product reported an overestimation of approximately 7% in mean annual rainfall compared to IMD observations. The IMDMERG dataset successfully aligned with the daily rainfall totals with IMD and provided greater consistency across the study area. This calibrationt preserved the sub-daily rainfall distribution patterns detected by IMERG while maintaining the ground-truth daily totals recorded by IMD.

The spatial evaluation of mean annual rainfall revealed that the IMDMERG dataset closely reproduced the spatial patterns of IMD rainfall. In contrast, the IMERG Final product displayed spatial anomalies in North East India and western ghat areas. It often underestimates or overestimates rainfall due to limitations in satellite retrieval algorithms under complex terrain and high rainfall intensity conditions. The difference map between IMDMERG and IMERG further highlighted that the most significant improvements occurred in these climatologically sensitive zones. The scatter plot analysis also underscored moderate agreement between the IMERG Final product and IMD datasets ($R^2 = 0.612$).

Beyond the calibration process, the chapter demonstrated the practical implications of the IMDMERG dataset in computing the Rainfall Erosivity Factor (R). Using the 20-year IMDMERG dataset (2001–2020), the study produced a detailed R factor map at 0.25° spatial resolution and 30-minute temporal resolution. The calibrated data yielded a mean R value of 3063 MJ.mm/ha.h.year, approximately 40% higher than the mean R factor computed using the IMERG Final product. The R factor maps derived from IMDMERG identified new erosivity hotspots particularly in the Western Ghats, Northeast India, and parts of the Eastern Ghats, regions where rainfall intensity and erosive potential are known to be high.

7.1.4 Climate change impact on Rainfall Erosivity Factor under CMIP6 shared socio-economic pathways

This study presents a comprehensive evaluation of how climate change influences rainfall erosivity of the Pamohi watershed, located in Guwahati, the largest city in the Eastern Himalayan region. The Global Climate Model (GCM) data used in climate projections are typically available at a daily temporal scale, while rainfall erosivity computation by standard method requires sub-daily rainfall data. To address this challenge, two approaches were explored in this study. The first approach is to develop a Multiple Linear Regression (MLR) model that enables the assessment of the R Factor directly from daily rainfall data and the second approach involves disaggregating daily rainfall into sub-daily intervals, enabling the direct application of the standard method for R Factor estimation.

The newly developed MLR model significantly outperformed existing widely used empirical models, resulting a very low percentage error of 2.86 %. This model was subsequently employed to project future rainfall erosivity under climate change scenarios for the Pamohi watershed. Climate projections were carried out for three future time slices, 2015–2040 (near future), 2041–2070 (mid future), and 2071–2100 (far future) considering two CMIP6 Shared Socioeconomic Pathways: SSP245 and SSP585. For the historical period, the R-factor ranged from 6912.84 to 7389.81 MJ.mm/ha.h.year, with a mean of 7208.64 MJmm/ha.h.year. Under SSP245, the R-factor is projected to increase to 7244.82, 7654.95, and 7764.31 MJmm/ha.h.year for the near, mid, and far future, respectively. Under the more extreme SSP585 pathway, projections show a sharper rise to 7385.82, 7969.81, and 9642.73 MJ.mm/ha.h.year for the same time periods. These results indicate a clear upward trend in rainfall erosivity across both scenarios. The projected percentage increases in the R-factor under SSP2-4.5 are 0.5%, 6.19%, and 7.71%, while under SSP585, the respective increases are 2.46%, 10.56%, and a substantial 33.77%. Notably, the only deviation from this trend is observed under the SSP245 scenario during the far future, where a slight decrease is projected.

The disaggregation of rainfall approach was also applied for the same future periods under identical climate change scenarios. The historical R factor estimated by disaggregated rainfall was found to be similar to the R factor computed by observed half hourly dataset. The R Factor for the historical period ranges from 6675 to 7674 MJ.mm/ha.h.yr with a mean of 7130 MJ.mm/ha.h.yr. In the near future period, the R Factor is projected to be 7473 MJ.mm/ha.h.yr under SSP 245 and 7708 MJ.mm/ha.h.yr under SSP 585. For the mid future, these values are expected to rise to 8397 MJ.mm/ha.h.yr and 8602 MJ.mm/ha.h.yr under SSP 245 and SSP 585, respectively. In the far future, the R Factor is projected to reach 9071 MJ.mm/ha.h.yr under SSP 245 and 13124 MJ.mm/ha.h.yr under SSP 585, indicating a more pronounced increase under the high-emission scenario. The estimated future R factor of the watershed shows an increasing trend for both the projected pathways. The projected percentage changes in the R factor under SSP 245 are 4.81%, 17.77%, and 27.22% for the near, mid, and far future periods, respectively. Similarly, under SSP 585 the resulted percentage changes are 8.20%, 20.64% and a substantial 84.07% across the same future periods.

The findings of this study were compared with analyses conducted at global, national, and regional scales and a strong consistency was observed with the results obtained from the rainfall disaggregation approach. The increasing trend in rainfall erosivity was also found in the MLR-based empirical model. The analysis shows that the empirical model is useful because it is simple and suitable for large-scale applications. However, it tends to smooth out local variations which leads to an underestimation of sharp erosivity peaks. It can be useful for initial decision-making contexts where extensive data or computational resources are not available. In contrast the rainfall disaggregation technique shows a strong ability to capture rainfall extremes. This makes it a more effective tool for detailed erosion risk assessments and identifying erosion-prone areas in climate-sensitive landscapes. The projections resulted here offer valuable insights for urban planners, environmental managers and policymakers working to alleviate the detrimental effects of climate change on soil and water management.

7.2 Key contribution of the thesis

1. A high-resolution, national-scale Rainfall Erosivity (R) factor map has been developed for mainland India (excluding the Ladakh region). A comprehensive spatio-temporal analysis of rainfall erosivity was conducted, revealing pronounced spatial and temporal heterogeneity across the country. In addition, a trend analysis and sensitivity analyses of the R factor were also performed.
2. The concept of return period was incorporated into the Rainfall Erosivity assessment, leading to the development of R factor maps corresponding to multiple return periods using high-resolution satellite-based precipitation data. A spatially distributed map representing the best-fitted probability distribution for

estimating the return level values of the annual R factor corresponding to different return periods was also developed.

3. The IMERG (Late) half-hourly satellite precipitation dataset was calibrated against IMD daily gridded rainfall data to produce a new rainfall dataset named IMDMERG. This newly developed dataset successfully retains the sub-daily rainfall distribution patterns captured by IMERG while preserving the ground-truth daily totals provided by IMD.
4. A Multiple Linear Regression (MLR) model was formulated to estimate the Rainfall Erosivity Factor for Guwahati and its surrounding areas using daily rainfall data.
5. The rainfall disaggregation approach was explored for assessing the rainfall erosivity of the Pamohi watershed located in Guwahati by employing the standard method for computing R factor.
6. Climate change impact assessment on rainfall erosivity was conducted for the Pamohi watershed using both the newly developed MLR model and the rainfall disaggregation approach.

7.3 Recommendation for future work

The scope of future research is discussed as follows:

1. In this study, the Rainfall Erosivity Factor for India was estimated using a high temporal and spatial resolution satellite-based precipitation product. Currently, the availability of rain gauge stations providing rainfall data at such fine temporal and spatial scales remains limited, posing constraints on purely observation-based erosivity assessments. In the future, this analysis may be revisited using observed rainfall data once a sufficiently dense network of high-resolution rain gauge stations becomes available across the country. Such advancements would help minimize uncertainties associated with satellite datasets and enhance the reliability of rainfall erosivity estimation at the national scale.
2. The return period analysis in this study was based on 20 years of data. Extending this period beyond 20 years in future studies would help in improving the reliability of return period estimates and provide better insights into extreme rainfall events. Based on this analysis, return period-based soil loss maps can also be prepared in the future. These maps will be useful for planning and designing soil conservation structures.

3. For assessing future rainfall erosivity, this study used bias-corrected precipitation data from 13 CMIP6 climate models and selected the top five models for analysis. Although this ensures consistency, the future studies can consider more climate models to include a wider range of possible outcomes. Also, only two future climate scenarios (SSP245 and SSP585) were explored here. Including more Shared Socioeconomic Pathways (SSPs) in future research will help provide a more complete picture of possible changes in rainfall erosivity under different future conditions.

References

Adler, R.F., Huffman, G.J., Chang, A., Ferraro, R., Xie, P.P., Janowiak, J., Rudolf, B., Schneider, U., Curtis, S., Bolvin, D., Gruber, A., Susskind, J., Arkin, P., Nelkin, E., 2003. The version-2 global precipitation climatology project (GPCP) monthly precipitation analysis (1979-present). J. Hydrometeorol. 4, 1147–1167. https://doi.org/10.1175/1525-7541(2003)004<1147:TVGPCP>2.0.CO;2

Adler, R.F., Sapiano, M.R.P., Huffman, G.J., Wang, J.J., Gu, G., Bolvin, D., Chiu, L., Schneider, U., Becker, A., Nelkin, E., Xie, P., Ferraro, R., Shin, D. Bin, 2018. The Global Precipitation Climatology Project (GPCP) monthly analysis (New Version 2.3) and a review of 2017 global precipitation. Atmosphere (Basel). 9. https://doi.org/10.3390/atmos9040138

Akhila, R., Pramada, S.K., 2025. Suitability of different Digital Elevation Models in the estimation of LS factor and soil loss. Environ. Monit. Assess. 197. https://doi.org/10.1007/s10661-025-13967-x

Akinwande, M.O., Dikko, H.G., Samson, A., 2015. Variance Inflation Factor: As a Condition for the Inclusion of Suppressor Variable(s) in Regression Analysis. Open J. Stat. 05, 754–767. https://doi.org/10.4236/ojs.2015.57075

Alam, M.A., Emura, K., Farnham, C., Yuan, J., 2018. Best-fit probability distributions and return periods for maximum monthly rainfall in Bangladesh. Climate 6, 1–16. https://doi.org/10.3390/cli6010009

Alemu, M.D., Laekemariam, F., Belay, S., Van Tol, J., Mengistu, A.G., 2025. Modeling soil erosion for sustainable landscape management using RUSLE in the landscapes of Abaya-Chamo Sub-Basin, Ethiopia. Model. Earth Syst. Environ. 11, 1–28. https://doi.org/10.1007/s40808-025-02337-8

Almagro, A., Oliveira, P.T.S., Nearing, M.A., Hagemann, S., 2017. Projected climate change impacts in rainfall erosivity over Brazil. Sci. Rep. 7, 1–12. https://doi.org/10.1038/s41598-017-08298-y

Alzahrani, F., Seidou, O., Alodah, A., 2023. Assessing the performance of daily to subdaily temporal disaggregation methods for the IDF curve generation under climate change. J. Water Clim. Chang. 14, 1339–1357. https://doi.org/10.2166/wcc.2023.507

Amsalu, Tadesse, Mengaw, Abebe, Amsalu, T, Mengaw, A, 2014. GIS Based Soil Loss Estimation Using RUSLE Model: The Case of Jabi Tehinan Woreda, ANRS, Ethiopia Keywords GIS, Remote Sensing, Multi-Criteria Evaluation (MCE), RUSLE, Weighted Overlay, Land Use/Land Cover (LULC), Soil Loss. Nat. Resour. 5, 616–626. https://doi.org/10.4236/nr.2014.511054

Arnoldous, H.M.J., 1980. An approximation of the rainfall factor in the Universal Soil Loss Equation, in: Boodt, M.D., Gabriels, D. (Eds.), Assessment of Erosion. John Wiley and sons Ltd., Chichester, UK, pp. 127–132.

Arnoldous, H.M.J., 1977. Methodology used to determine the maximum potential average annual soil loss due to sheet and rill erosion in Morocco. FAO Soils Bull.

34, 39–51.

Aronica, G., Ferro, V., 1997. Erosivité des précipitations en Calabre. Hydrol. Sci. J. 42, 35–48. https://doi.org/10.1080/02626669709492004

Azari, M., Oliaye, A., Nearing, M.A., 2021. Expected climate change impacts on rainfall erosivity over Iran based on CMIP5 climate models. J. Hydrol. 593, 125826. https://doi.org/10.1016/j.jhydrol.2020.125826

Babu, R., Dhyani, B.L., Kumar, N., 2004. Assessment of erodibility status and refined Iso-Erodent Map of India. Indian J. Soil Conserv. 32.

Babu, R., Tejwani, K.G., Agarwal, H.C., Bhusan, L.S., 1978. Distribution of Erosion Index and Iso – erodent maps of India. Indian J. Soil Conserv. 6, 1–12.

Bagarello, V., Di Stefano, C., Ferro, V., Pampalone, V., 2011. Using plot soil loss distribution for soil conservation design. Catena 86, 172–177. https://doi.org/10.1016/j.catena.2011.03.009

Bagarello, V., Di Stefano, C., Ferro, V., Pampalone, V., 2010. Statistical distribution of soil loss and sediment yield at Sparacia experimental area, Sicily. Catena 82, 45–52. https://doi.org/10.1016/j.catena.2010.04.006

Baishya, B., Sarma, A.K., 2024. Inferring sediment deposition trend in data scared wetland impacted by degraded urban catchment. Int. J. Sediment Res. https://doi.org/10.1016/j.ijsrc.2024.10.007

Benavidez, R., Jackson, B., Maxwell, D., Norton, K., 2018. A review of the (Revised) Universal Soil Loss Equation ((R) USLE): with a view to increasing its global applicability and improving soil loss estimates 6059–6086.

Bera, A., 2017. Assessment of soil loss by universal soil loss equation (USLE) model using GIS techniques: a case study of Gumti River Basin, Tripura, India. Model. Earth Syst. Environ. 3, 1–9. https://doi.org/10.1007/s40808-017-0289-9

Bergsma, E., Charman, P., Hurni, H., Moldenhauer, W.C., Panichapong, S., 1996. Terminology for Soil Erosion and Conservation, International Society of Soil Science. UK.

Bezak, N., Borrelli, P., Panagos, P., 2022. Exploring the possible role of satellite-based rainfall data in estimating inter- and intra-annual global rainfall erosivity. Hydrol. Earth Syst. Sci. 26, 1907–1924. https://doi.org/10.5194/hess-26-1907-2022

Bhandari, K.P., Aryal, J., Darnsawasdi, R., 2015. A geospatial approach to assessing soil erosion in a watershed by integrating socio-economic determinants and the RUSLE model. Nat. Hazards 75, 321–342. https://doi.org/10.1007/s11069-014-1321-2

Bhuiyan, M.A.E., Yang, F., Biswas, N.K., Rahat, S.H., Neelam, T.J., 2020. Machine Learning-Based Error Modeling to Improve GPM IMERG Precipitation Product over the Brahmaputra River Basin. Forecasting 2, 248–266. https://doi.org/10.3390/forecast2030014

Biasutti, M., Seager, R., 2015. Projected changes in US rainfall erosivity. Hydrol. Earth Syst. Sci. 19, 2945–2961. https://doi.org/10.5194/hess-19-2945-2015

Bonilla, C.A., Vidal, K.L., 2011. Rainfall erosivity in Central Chile. J. Hydrol. 410, 126–133. https://doi.org/10.1016/j.jhydrol.2011.09.022

Bordoloi, P.K., 2015. GUWAHATY CITY GUWAHATY CITY WATERLOGGING - DISASTER OR PROBLEM ?, in: AICTE-NEQIP Sponsored Two Days International Seminar at Guwahaty on Diaster Management – Issues and Challenges. https://doi.org/10.13140/RG.2.1.4182.3766

Borrelli, P., Robinson, D.A., Panagos, P., Lugato, E., Yang, J.E., Alewell, C., Wuepper, D., Montanarella, L., Ballabio, C., 2020. Land use and climate change impacts on global soil erosion by water (2015-2070). Proc. Natl. Acad. Sci. U. S. A. 117, 21994–22001. https://doi.org/10.1073/pnas.2001403117

Brown, L.C., Foster, G.R., 1987. Storm erosivity using idealized intensity distributions. Trans. ASAE, Am. Soc. Agric. Eng. 30, 379–386.

Burton, A., Fowler, H.J., Blenkinsop, S., Kilsby, C.G., 2010. Downscaling transient climate change using a Neyman-Scott Rectangular Pulses stochastic rainfall model. J. Hydrol. 381, 18–32. https://doi.org/10.1016/j.jhydrol.2009.10.031

Bushair, M.T., Kumar, P., Gairola, R.M., 2019. Evaluation and assimilation of various satellite-derived rainfall products over India. Int. J. Remote Sens. 40, 5315–5338. https://doi.org/10.1080/01431161.2019.1579389

Capolongo, D., Diodato, N., Mannaerts, C.M., Piccarreta, M., Strobl, R.O., 2008. Analyzing temporal changes in climate erosivity using a simplified rainfall erosivity model in Basilicata (southern Italy). J. Hydrol. 356, 119–130. https://doi.org/10.1016/j.jhydrol.2008.04.002

Chatterjee, S., Krishna, A.P., Sharma, A.P., 2014. Geospatial assessment of soil erosion vulnerability at watershed level in some sections of the Upper Subarnarekha river basin, Jharkhand, India. Environ. Earth Sci. 71, 357–374. https://doi.org/10.1007/s12665-013-2439-3

Chaudhary, S., Dhanya, C.T., 2020. Decision tree-based reduction of bias in monthly IMERG satellite precipitation dataset over India. H2Open J. 3, 236–255. https://doi.org/10.2166/h2oj.2020.124

Chen, Y., Wei, T., Li, J., Xin, Y., Ding, M., 2024. Future changes in global rainfall erosivity: Insights from the precipitation changes. J. Hydrol. 638, 131435. https://doi.org/10.1016/j.jhydrol.2024.131435

Chen, Y., Xu, M., Wang, Z., Gao, P., Lai, C., 2021. Applicability of two satellite-based precipitation products for assessing rainfall erosivity in China. Sci. Total Environ. 757, 143975. https://doi.org/10.1016/j.scitotenv.2020.143975

Cohen, M.J., Shepherd, K.D., Walsh, M.G., 2005. Empirical reformulation of the universal soil loss equation for erosion risk assessment in a tropical watershed. Geoderma 124, 235–252. https://doi.org/10.1016/j.geoderma.2004.05.003

Cook, H.L., 1937. The Nature and Controlling Variables of the Water Erosion Process. Soil Sci. Soc. Am. J. 1, 487–494. https://doi.org/10.2136/sssaj1937.036159950001000000085x

Cowpertwait, P., Ocio, D., Collazos, G., De Cos, O., Stocker, C., 2013. Regionalised spatiotemporal rainfall and temperature models for flood studies in the Basque Country, Spain. Hydrol. Earth Syst. Sci. 17, 479–494. https://doi.org/10.5194/hess-17-479-2013

Das, D.C., Babu, R., 1979. Computation and estimation of rainfall energy and erosion indices in metric units. Indian For. 105, 217–222.

Das, S., Jain, M.K., 2023. Unravelling the future changes in rainfall erosivity over India under shared socio-economic pathways. Catena 232, 107417. https://doi.org/10.1016/j.catena.2023.107417

Das, T., Sarma, A.K., 2021. Estimation of rainfall erosivity factor of Guwahati with high temporal resolution rainfall data, in: HYDRO 2020 INTERNATIONAL, 25th International Conference on Hydraulics, Water Resources and River Engineering. p. 80.

Dash, C.J., Adhikary, P.P., Das, N.K., Alam, N.M., Mandal, U., Mishra, P.K., 2018. Comparison of rainfall kinetic energy–intensity relationships for Eastern Ghats Highland region of India. Nat. Hazards 93, 547–558. https://doi.org/10.1007/s11069-018-3314-z

Dash, C.J., Das, N.K., Adhikary, P.P., 2019. Rainfall erosivity and erosivity density in Eastern Ghats Highland of east India. Nat. Hazards 97, 727–746. https://doi.org/10.1007/s11069-019-03670-9

de Mello, C.R., Ávila, L.F., Viola, M.R., Curi, N., Norton, L.D., 2015. Assessing the climate change impacts on the rainfall erosivity throughout the twenty-first century in the Grande River Basin (GRB) headwaters, Southeastern Brazil. Environ. Earth Sci. 73, 8683–8698. https://doi.org/10.1007/s12665-015-4033-3

Devatha, C.P., Deshpande, V., Renukaprasad, M.S., 2015. Estimation of Soil loss Using USLE Model for Kulhan Watershed, Chattisgarh- A Case Study. Aquat. Procedia 4, 1429–1436. https://doi.org/10.1016/j.aqpro.2015.02.185

Diez-Sierra, J., del Jesus, M., 2019. Subdaily rainfall estimation through daily rainfall downscaling using random forests in Spain. Water (Switzerland) 11. https://doi.org/10.3390/w11010125

Diez-Sierra, J., Navas, S., Del Jesus, M., 2023. NEOPRENE v1.0.1: A Python library for generating spatial rainfall based on the Neyman-Scott process. Geosci. Model Dev. 16, 5035–5048. https://doi.org/10.5194/gmd-16-5035-2023

Diez-sierra, J., Navas, S., Jesus, M., 2023. NEOPRENE v1 . 0 . 1 : a Python library for generating spatial rainfall based on the Neyman – Scott process 5035–5048.

Diodato, N., 2004. Estimating RUSLE’s rainfall factor in the part of Italy with a Mediterranean rainfall regime. Hydrol. Earth Syst. Sci. 8, 103–107. https://doi.org/10.5194/hess-8-103-2004

Diodato, N., Bellocchi, G., 2010. MedREM, a rainfall erosivity model for the Mediterranean region. J. Hydrol. 387, 119–127. https://doi.org/10.1016/j.jhydrol.2010.04.003

Diodato, N., Bellocchi, G., 2009. Assessing and modelling changes in rainfall erosivity at different climate scales. Earth Surf. Process. Landforms 34, 969–980.

Dutta, D., Das, S., Kundu, A., Taj, A., 2015. Soil erosion risk assessment in Sanjal watershed, Jharkhand (India) using geo-informatics, RUSLE model and TRMM data. Model. Earth Syst. Environ. 1, 1–9. https://doi.org/10.1007/s40808-015-0034-1

Duulatov, E., Chen, X., Amanambu, A.C., Ochege, F.U., Orozbaev, R., Issanova, G., Omurakunova, G., 2019. Projected rainfall erosivity over Central Asia based on CMIP5 climate models. Water (Switzerland) 11, 1–16. https://doi.org/10.3390/w11050897

Eekhout, J.P.C., de Vente, J., 2022. Global impact of climate change on soil erosion and potential for adaptation through soil conservation. Earth-Science Rev. 226, 103921. https://doi.org/10.1016/j.earscirev.2022.103921

El-Swaify, S.A., Arsyad, S., 1983. Soil erosion by water, in: The Handbook on Natural Systems Information for Planners. The MacMillan Co. Inc., New York, pp. 99–161.

Emberson, R.A., 2023. Dynamic Rainfall Erosivity Estimates Derived from GPM IMERG data. Egusph. Prepr. Repos.

Endalamaw, N.T., Moges, M.A., Kebede, Y.S., Alehegn, B.M., Sinshaw, B.G., 2021. Potential soil loss estimation for conservation planning, upper Blue Nile Basin, Ethiopia. Environ. Challenges 5, 100224. https://doi.org/10.1016/j.envc.2021.100224

Endalew, T., Biru, D., 2022. Results in Geophysical Sciences Soil erosion risk and sediment yield assessment with Revised Universal Soil Loss Equation and GIS : The case of Nesha watershed , Southwestern Ethiopia. Results Geophys. Sci. 12, 100049. https://doi.org/10.1016/j.ringps.2022.100049

Fan, J. rong, Chen, Y., Yan, D., Guo, F. fen, 2013. Characteristics of rainfall erosivity based on tropical rainfall measuring mission data in Tibet, China. J. Mt. Sci. 10, 1008–1017. https://doi.org/10.1007/s11629-013-2378-1

Farhan, Y., Alnawaiseh, S., 2018. Spatio-Temporal Variation in Rainfall Erosivity over Jordan Using Annual and Seasonal Precipitation. Nat. Resour. 09, 242–267. https://doi.org/10.4236/nr.2018.96016

Fayas, C.M., Abeysingha, N.S., Nirmanee, K.G.S., Samaratunga, D., Mallawatantri, A., 2019. Soil loss estimation using rusle model to prioritize erosion control in KELANI river basin in Sri Lanka. Int. Soil Water Conserv. Res. 7, 130–137. https://doi.org/10.1016/j.iswcr.2019.01.003

Fenta, A.A., Yasuda, H., Shimizu, K., Haregeweyn, N., Kawai, T., Sultan, D., Ebabu, K., Belay, A.S., 2017. Spatial distribution and temporal trends of rainfall and erosivity in the Eastern Africa region. Hydrol. Process. 31, 4555–4567. https://doi.org/10.1002/hyp.11378

Ferro, V., Giordano, G., Iovino, M., 1991a. Isoerosivity and erosion risk map for sicily. Hydrol. Sci. J. 36, 549–564. https://doi.org/10.1080/02626669109492543

Ferro, V., Giordano, G., Iovino, M., 1991b. Isoerosivity and erosion risk map for sicily. Hydrol. Sci. J. 36, 549–564. https://doi.org/10.1080/02626669109492543

Ferro, V., Porto, P., Yu, B., 1999. A comparative study of rainfall erosivity estimation for southern Italy and southeastern Australia. Hydrol. Sci. J. 44, 3–24. https://doi.org/10.1080/02626669909492199

Fuller, W., 1914. Flood flows. Trans. Am. Soc. Civ. Eng. 77.

Gad, A.G., 2022. Particle Swarm Optimization Algorithm and Its Applications: A

Systematic Review, Archives of Computational Methods in Engineering. Springer Netherlands. https://doi.org/10.1007/s11831-021-09694-4

Gafforov, K.S., Bao, A., Rakhimov, S., Liu, T., Abdullaev, F., Jiang, L., Durdiev, K., Duulatov, E., Rakhimova, M., Mukanov, Y., 2020. The assessment of climate change on rainfall-runoff erosivity in the Chirchik-Akhangaran Basin, Uzbekistan. Sustain. 12. https://doi.org/10.3390/SU12083369

Gairola, R.M., Prakash, S., Pal, P.K., 2015. Improved rainfall estimation over the Indian monsoon region by synergistic use of Kalpana-1 and rain gauge data. Atmosfera 28, 51–61. https://doi.org/10.1016/s0187-6236(15)72159-4

Ganasri, B.P., Ramesh, H., 2016. Assessment of soil erosion by RUSLE model using remote sensing and GIS - A case study of Nethravathi Basin. Geosci. Front. 7, 953–961. https://doi.org/10.1016/j.gsf.2015.10.007

Gelagay, H.S., Minale, A.S., 2016. Soil loss estimation using GIS and Remote sensing techniques: A case of Koga watershed, Northwestern Ethiopia. Int. Soil Water Conserv. Res. 4, 126–136. https://doi.org/10.1016/j.iswcr.2016.01.002

Ghosh, K., Kumar De, S., Bandyopadhyay, S., Saha, S., 2013. Assessment of Soil Loss of the Dhalai River Basin, Tripura, India Using USLE. Int. J. Geosci. 04, 11–23. https://doi.org/10.4236/ijg.2013.41002

Gobinath, R., Ganapathy, G.P., Gayathiri, E., Salunkhed, A.., Pourghasemie, H.., 2022. Ecoengineering practices for soil degradation protection of vulnerable hill slopes, in: Computers in Earth and Environmental Sciences. pp. 255–270.

Gonzalez-Hidalgo, J.C., Batalla, R.J., Cerda, A., de Luis, M., 2012. A regional analysis of the effects of largest events on soil erosion. Catena 95, 85–90. https://doi.org/10.1016/j.catena.2012.03.006

Hadda, M.S., Sur, H.S., Sandhu, K.S., 1991. Relationship between daily rainfall depth and erosivity. J. Indian Soc. Soil Sci. 39, 37–39.

Hamed, K.H., 2008. Trend detection in hydrologic data: The Mann-Kendall trend test under the scaling hypothesis. J. Hydrol. 349, 350–363. https://doi.org/10.1016/j.jhydrol.2007.11.009

Hamed, K.H., Rao, A.R., 1998. A modified Mann-Kendall trend test for autocorrelated data. J. Hydrol. 204, 182–196.

Hamidreza, S., Mohsen, S., 2017. Spatiotemporal mapping of rainfall erosivity index for different return periods in Iran. Nat. Hazards. https://doi.org/10.1007/s11069-017-2752-3

Hateffard, F., Mohammed, S., Alsafadi, K., Enaruvbe, G.O., Heidari, A., Abdo, H.G., Rodrigo-Comino, J., 2021. CMIP5 climate projections and RUSLE-based soil erosion assessment in the central part of Iran. Sci. Rep. 11, 1–17. https://doi.org/10.1038/s41598-021-86618-z

He, L., Wang, G.Q., Fu, X.D., 2010. Disaggregation model of daily rainfall and its application in the Xiaolihe Watershed, Yellow River. J. Environ. Informatics 16, 11–18. https://doi.org/10.3808/jei.201000173

Hernando, D., Romana, M.G., Hernando, D., Romana, M.G., 2015. Estimating the rainfall erosivity factor from monthly precipitation data in the Madrid Region (Spain) 55–62. https://doi.org/10.1515/johh-2015-0003

Heumann, C., Shalabh, M.S., 2016. Introduction to Statistics and Data Analysis. Springer International Publishing, Capetown, South Africa.

Hsu, K.L., Gao, X., Sorooshian, S., Gupta, H. V., 1997. Precipitation estimation from remotely sensed information using artificial neural networks. J. Appl. Meteorol. 36, 1176–1190. https://doi.org/10.1175/1520-0450(1997)036<1176:PEFRSI>2.0.CO;2

Huffman, G.J., Adler, R.F., Arkin, P., Chang, A., Ferraro, R., Gruber, A., Janowiak, J., McNab, A., Rudolf, B., Schneider, U., 1997. The Global Precipitation Climatology Project (GPCP) Combined Precipitation Dataset. Bull. Am. Meteorol. Soc. 78, 5–20. https://doi.org/10.1175/1520-0477(1997)078<0005:TGPCPG>2.0.CO;2

Huffman, G.J., Adler, R.F., Bolvin, D.T., Gu, G., Nelkin, E.J., Bowman, K.P., Hong, Y., Stocker, E.F., Wolff, D.B., 2007. The TRMM Multisatellite Precipitation Analysis (TMPA): Quasi-global, multiyear, combined-sensor precipitation estimates at fine scales. J. Hydrometeorol. 8, 38–55. https://doi.org/10.1175/JHM560.1

Huffman, G.J., Stocker, E.F., Bolvin, D.T., Nelkin, E.J., Jackson, T., 2019. GPM IMERG Final Precipitation L3 Half Hourly 0.1 degree x 0.1 degree V06, Goddard Earth Sciences Data and Information Services Center (GES DISC).

Hurni, H., 1988. Degradation and conservation of the resources in the Ethiopian highlands. Mt. Res. Dev. 8, 123–130.

ICONA, 1988. Agresividad de la lluvia en España. Valores del factor R de la ecuación universal de pérdidas de suelo. [Rainfall erosivity in Spain. R-factor values for the Universal Soil Loss Equation].

IPCC, 2019. Special Report on climate change, desertification, land degradation, sustainable land management, food security, and greenhouse gas fluxes in terrestrial ecosystems (SR2).

Islam, S.U., Chakma, S., 2024. Evaluating the long-term influence of climate change on rainfall erosivity in the Jhelum Catchment: a GCM-based analysis. Environ. Dev. Sustain. https://doi.org/10.1007/s10668-024-05286-x

ISRO, 2021. Desertification and Land Degradation Atlas of India, Assessment and Analysis of Changes over 15 years Based on Remote sensing, Indian Space Research Organization, Government of India. https://doi.org/10.1201/9781351115629

Issaka, S., Ashraf, M.A., 2017. Impact of soil erosion and degradation on water quality: a review. Geol. Ecol. Landscapes 1, 1–11. https://doi.org/10.1080/24749508.2017.1301053

Jain, S.K., 2019. Water resources management in India-Challenges and the way forward. Curr. Sci. 117, 569–576.

Jebari, S., Berndtsson, R., Olsson, J., Bahri, A., 2012. Soil erosion estimation based on rainfall disaggregation. J. Hydrol. 436–437, 102–110. https://doi.org/10.1016/j.jhydrol.2012.03.001

Joshi, V., Susware, N., Sinha, D., 2016. Estimating soil loss from a watershed in Western Deccan, India, using Revised Universal Soil Loss Equation. Landsc. Environ. 10, 13–25. https://doi.org/10.21120/le/10/1/2

Joyce, R.J., Janowiak, J.E., Arkin, P.A., Xie, P., 2004. CMORPH: A method that produces global precipitation estimates from passive microwave and infrared data at high spatial and temporal resolution. J. Hydrometeorol. 5, 487–503. https://doi.org/10.1175/1525-7541(2004)005<0487:CAMTPG>2.0.CO;2

Kalambukattu, J., Kumar, S., 2017. Modelling soil erosion risk in a mountainous watershed of Mid-Himalaya by integrating RUSLE model with GIS. Eurasian J. Soil Sci. 6, 92–105. https://doi.org/10.18393/ejss.286442

Karale, R.L., Narula, K.K., Dayal, V., Saini, K.M., 1989. Data base management system for erosivity values. J. Indian Soc. Remote Sens. 17, 23–31.

Kayet, N., Pathak, K., Chakrabarty, A., Sahoo, S., 2018. Evaluation of soil loss estimation using the RUSLE model and SCS-CN method in hillslope mining areas. Int. Soil Water Conserv. Res. 6, 31–42. https://doi.org/10.1016/j.iswcr.2017.11.002

Kendall, M.G., 1975. Rank Correlation Methods, 4th Editio. ed. Charles Griffin, London.

Khare, D., Mondal, A., Kundu, S., Mishra, P.K., 2017a. Climate change impact on soil erosion in the Mandakini River Basin, North India. Appl. Water Sci. 7, 2373–2383. https://doi.org/10.1007/s13201-016-0419-y

Khare, D., Mondal, A., Kundu, S., Mishra, P.K., 2017b. Climate change impact on soil erosion in the Mandakini River Basin, North India. Appl. Water Sci. 7, 2373–2383. https://doi.org/10.1007/s13201-016-0419-y

Kim, J., Han, H., Kim, B., Chen, H., Lee, J.H., 2020. Use of a high-resolution-satellite-based precipitation product in mapping continental-scale rainfall erosivity: A case study of the United States. Catena 193, 104602. https://doi.org/10.1016/j.catena.2020.104602

Kousar, S., Khan, A.R., Ul Hassan, M., Noreen, Z., Bhatti, S.H., 2020. Some best-fit probability distributions for at-site flood frequency analysis of the Ume River. J. Flood Risk Manag. 13, 1–11. https://doi.org/10.1111/jfr3.12640

Kumar, A., Devi, M., Deshmukh, B., 2014. Integrated Remote Sensing and Geographic Information System Based RUSLE Modelling for Estimation of Soil Loss in Western Himalaya, India. Water Resour. Manag. 28, 3307–3317. https://doi.org/10.1007/s11269-014-0680-5

Kumar, P., Varma, A.., Kubota, T., Yamaji, M., Tashima, T., Mega, T., Ushio, T., 2022. Long-Term High-Resolution Gauge Adjusted Satellite Rainfall Product Over India. Earth Sp. Sci. 9. https://doi.org/https://doi.org/10.1029/2022EA002595

Kumar, S., Kushwaha, S.P.S., 2013. Modelling soil erosion risk based on RUSLE-3D using GIS in a Shivalik sub-watershed. J. Earth Syst. Sci. 122, 389–398. https://doi.org/10.1007/s12040-013-0276-0

Lal, R., 2001. Soil Degradation by Erosion. L. Degrad. Dev. 12, 519–539.

Langat, P., K., Kumar, L., Koech, R., 2019. Identification of the Most Suitable Probability and Mean Streamflow. Water,11,734 1–24.

Lee, J., Heo, J., 2011. Evaluation of estimation methods for rainfall erosivity based on annual precipitation in Korea. J. Hydrol. 409, 30–48.

https://doi.org/10.1016/j.jhydrol.2011.07.031

Li, D., Qi, Y., Zhou, T., 2021. Changes in rainfall erosivity over mainland China under stabilized 1.5 ℃ and 2 ℃ warming futures. J. Hydrol. 603, 126996. https://doi.org/10.1016/j.jhydrol.2021.126996

Li, X., Li, Z., Lin, Y., 2020. Suitability of trmm products with different temporal resolution (3-hourly, daily, and monthly) for rainfall erosivity estimation. Remote Sens. 12, 1–21. https://doi.org/10.3390/rs12233924

Loureiro, N. de S., Coutinho, M. de A., 2001. A new procedure to estimate the RUSLE EI30index, based on monthly rainfall data and applied to the Algarve region, Portugal. J. Hydrol. 250, 12–18. https://doi.org/10.1016/S0022-1694(01)00387-0

Ma, Z., Xu, J., Zhu, S., Yang, J., Tang, G., Yang, Y., Shi, Z., Hong, Y., 2020. AIMERG: A new Asian precipitation dataset (0.1°/half-hourly, 2000-2015) by calibrating the GPM-era IMERG at a daily scale using APHRODITE. Earth Syst. Sci. Data 12, 1525–1544. https://doi.org/10.5194/essd-12-1525-2020

Maeda, E.E., Pellikka, P.K.E., Siljander, M., Clark, B.J.F., 2010. Potential impacts of agricultural expansion and climate change on soil erosion in the Eastern Arc Mountains of Kenya. Geomorphology 123, 279–289. https://doi.org/10.1016/j.geomorph.2010.07.019

Magesh, N.S., Chandrasekar, N., 2016. Assessment of soil erosion and sediment yield in the Tamiraparani sub-basin, South India, using an automated RUSLE-SY model. Environ. Earth Sci. 75, 1–17. https://doi.org/10.1007/s12665-016-6010-x

Mahmoud, M.T., Mohammed, S.A., Hamouda, M.A., Mohamed, M.M., 2021. Impact of topography and rainfall intensity on the accuracy of imerg precipitation estimates in an arid region. Remote Sens. 13, 1–17. https://doi.org/10.3390/rs13010013

Mangukiya, N.K., Mehta, D.J., Jariwala, R., 2022. Flood frequency analysis and inundation mapping for lower Narmada basin, India. Water Pract. Technol. 17, 612–622. https://doi.org/10.2166/wpt.2022.009

Mann, H.B., 1945. Nonparametric tests against trend. Econometrica 13, 245–259.

Mannaerts, C.M., Gabriels, D., 2000. A probabilistic approach for predicting rainfall soil erosion losses in semiarid areas. Catena 40, 403–420. https://doi.org/10.1016/S0341-8162(00)00089-8

Martins, S.G., Avanzi, C., Silva, M.L.N., Curi, N., Norton, L.D., Fonseca, S., 2010. Rosividade Da Chuva E Tempo De Retorno Na Bacia Experimental Da Aracruz, Região Dos Tabuleiros Costeiros Brasileiros. Rev. Bras. Cienc. do Solo 34, 999–1004. https://doi.org/10.1590/S0100-06832010000300042

Maximillian, J., Brusseau, M.L., Glenn, E.P., Matthias, A.D., 2019. Pollution and Environmental Perturbations in the Global System, 3rd ed, Environmental and Pollution Science. Elsevier Inc. https://doi.org/10.1016/b978-0-12-814719-1.00025-2

McCool, D.K., Williams, J.D., 2008. Soil Erosion by Water. Encycl. Ecol. Five-Volume Set 3284–3290. https://doi.org/10.1016/B978-008045405-4.00296-2

Mega, T., Ushio, T., Kubota, T., Kachi, M., Aonashi, K., Shige, S., 2014. Gauge adjusted global satellite mapping of precipitation (GSMaP-Gauge). 2014 31th URSI Gen. Assem. Sci. Symp. URSI GASS 2014 1–4. https://doi.org/10.1109/URSIGASS.2014.6929683

Mirhosseini, G., Srivastava, P., Stefanova, L., 2013. The impact of climate change on rainfall Intensity-Duration-Frequency (IDF) curves in Alabama. Reg. Environ. Chang. 13, 25–33. https://doi.org/10.1007/s10113-012-0375-5

Mishra, V., Bhatia, U., Tiwari, A.D., 2020. Bias-corrected climate projections for South Asia from Coupled Model. Sci. Data 1–13. https://doi.org/10.1038/s41597-020-00681-1

Mitra, A.K., Bohra, A.K., Rajeevan, M.N., Krishnamurti, T.N., 2009. Daily indian precipitation analysis formed from a merge of rain-gauge data with the TRMM TMPA satellite-derived rainfall estimates. J. Meteorol. Soc. Japan 87 A, 265–279. https://doi.org/10.2151/jmsj.87A.265

Mondal, A., Khare, D., Kundu, S., 2016. Change in rainfall erosivity in the past and future due to climate change in the central part of India. Int. Soil Water Conserv. Res. 4, 186–194. https://doi.org/10.1016/j.iswcr.2016.08.004

Morgan R.P.C., 1986. Soil Erosion and Conservation, Third Edit. ed. Blackwell Publishing.

Mukhopadhyay, P., Prasad, V.S., Krishna, R.P.M., Deshpande, M., Ganai, M., Tirkey, S., Sarkar, S., Goswami, T., Johny, C.J., Roy, K., Mahakur, M., Durai, V.R., Rajeevan, M., 2019. Performance of a very high-resolution global forecast system model (GFS T1534) at 12.5 km over the Indian region during the 2016–2017 monsoon seasons. J. Earth Syst. Sci. 128, 1–18. https://doi.org/10.1007/s12040-019-1186-6

Murali Krishna, U. V., Das, S.K., Deshpande, S.M., Doiphode, S.L., Pandithurai, G., 2017. The assessment of Global Precipitation Measurement estimates over the Indian subcontinent. Earth Sp. Sci. 4, 540–553. https://doi.org/10.1002/2017EA000285

Mustefa, M., Fufa, F., Takala, W., 2019. GIS estimation of annual average soil loss rate from Hangar River watershed using RUSLE. J. Water Clim. Chang. 1–11. https://doi.org/10.2166/wcc.2019.181

Nandgude, S., Shinde, V., Mahale, D., Singh, M., 2013. Synthesis of Rainfall Characteristics for Predicting the Erosivity Pattern of Wakavali Region in Maharashtra, India. J. Hydrol. Eng. 18, 92–98. https://doi.org/10.1061/(asce)he.1943-5584.0000496

Nazzareno, D., Bellocchi, G., 2014. Storminess and Environmental Change: Climate Forcing and Responses in the Mediterranean Region. https://doi.org/10.1007/978-94-007-7948-8

Nearing, M.A., 2001. Potential changes in rainfall erosivity in the U.S. with climate change during the 21st century. J. Soil Water Conserv. 56, 229–232.

Oliveira, P.T.S., Nearing, M.A., Moran, M.S., Goodrich, D.C., Wendland, E., Gupta, H.V., 2014. Trends in water balance components across the Brazilian Cerrado. Water Resour. Resea 50, 7100–7114. https://doi.org/10.1002/2013WR014979.Reply

Onof, C., Chandler, R.E., Kakou, A., Northrop, P., Wheater, H.S., Isham, V., 2000. Rainfall modelling using poisson-cluster processes: A review of developments. Stoch. Environ. Res. Risk Assess. 14, 384–411. https://doi.org/10.1007/s004770000043

Pai, D.S., Sridhar, L., Rajeevan, M., Sreejith, O.P., Satbhai, N.S., Mukhopadhyay, B., 2014. Development of a new high spatial resolution (0.25° × 0.25°) long period (1901-2010) daily gridded rainfall data set over India and its comparison with existing data sets over the region. Mausam 65, 1–18. https://doi.org/10.54302/mausam.v65i1.851

Pal, S., 2016. Identification of soil erosion vulnerable areas in Chandrabhaga river basin: a multi-criteria decision approach. Model. Earth Syst. Environ. 2, 1–11. https://doi.org/10.1007/s40808-015-0052-z

Pal, S.C., Chakrabortty, R., 2019. Simulating the impact of climate change on soil erosion in sub-tropical monsoon dominated watershed based on RUSLE, SCS runoff and MIROC5 climatic model. Adv. Sp. Res. 64, 352–377. https://doi.org/10.1016/j.asr.2019.04.033

Pal, S.C., Shit, M., 2017. Application of RUSLE model for soil loss estimation of Jaipanda watershed, West Bengal. Spat. Inf. Res. 25, 399–409. https://doi.org/10.1007/s41324-017-0107-5

Pampalone, V., Ferro, V., 2020. Estimating soil loss of given return period by USLE-M-type models. Hydrol. Process. 34, 2324–2336. https://doi.org/10.1002/hyp.13730

Panagos, P., Ballabio, C., Meusburger, K., Spinoni, J., Alewell, C., Borrelli, P., 2017a. Towards estimates of future rainfall erosivity in Europe based on REDES and WorldClim datasets. J. Hydrol. 548, 251–262. https://doi.org/10.1016/j.jhydrol.2017.03.006

Panagos, P., Borrelli, P., Matthews, F., Liakos, L., Bezak, N., Diodato, N., Ballabio, C., 2022a. Global rainfall erosivity projections for 2050 and 2070. J. Hydrol. 610, 127865. https://doi.org/10.1016/j.jhydrol.2022.127865

Panagos, P., Borrelli, P., Matthews, F., Liakos, L., Bezak, N., Diodato, N., Ballabio, C., 2022b. Global rainfall erosivity projections for 2050 and 2070. J. Hydrol. 610, 127865. https://doi.org/10.1016/j.jhydrol.2022.127865

Panagos, P., Borrelli, P., Meusburger, K., Yu, B., Klik, A., Lim, K.J., Yang, J.E., Ni, J., Miao, C., Chattopadhyay, N., Sadeghi, S.H., Hazbavi, Z., Zabihi, M., Larionov, G.A., Krasnov, S.F., Gorobets, A. V., Levi, Y., Erpul, G., Birkel, C., Hoyos, N., Naipal, V., Oliveira, P.T.S., Bonilla, C.A., Meddi, M., Nel, W., Al Dashti, H., Boni, M., Diodato, N., Van Oost, K., Nearing, M., Ballabio, C., 2017b. Global rainfall erosivity assessment based on high-temporal resolution rainfall records. Sci. Rep. 7, 1–12. https://doi.org/10.1038/s41598-017-04282-8

Panagos, P., Meusburger, K., Ballabio, C., Borrelli, P., Alewell, C., 2014. Science of the Total Environment Soil erodibility in Europe : A high-resolution dataset based on LUCAS. Sci. Total Environ. 479–480, 189–200. https://doi.org/10.1016/j.scitotenv.2014.02.010

Patowary, S., Sarma, A.K., 2018. GIS-Based Estimation of Soil Loss from Hilly Urban Area Incorporating Hill Cut Factor into RUSLE. Water Resour. Manag. 32, 3535–

3547. https://doi.org/10.1007/s11269-018-2006-5

Patowary, S., Sarma, B., Sarma, A.K., 2019. A Revision of OPTEMP-LS Model for Selecting Optimal EMP Combination for Minimizing Sediment and Water Yield from Hilly Urban Watersheds. Water Resour. Manag. 33, 1249–1264. https://doi.org/10.1007/s11269-018-2180-5

Pérez, R.E., Cortés-Molina, M., Navarro-González, F.J., 2021. Analysis of rainfall time series with application to calculation of return periods. Sustainability 13. https://doi.org/10.3390/su13148051

Pheerawat, P., Udmale, P., 2017. Impacts of climate change on rainfall erosivity in the Huai Luang watershed, Thailand. Atmosphere (Basel). 8. https://doi.org/10.3390/atmos8080143

Plangoen, P., Babel, M., 2014. Projected Rainfall Erosivity Changes under Future Climate in the Upper Nan Watershed, Thailand. J. Earth Sci. Clim. Change 05. https://doi.org/10.4172/2157-7617.1000242

Poornima, S., Pushpalatha, M., Jana, R.B., Patti, L.A., 2023. Rainfall Forecast and Drought Analysis for Recent and Forthcoming Years in India. Water (Switzerland) 15. https://doi.org/10.3390/w15030592

Prakash, S., Mitra, A.K., AghaKouchak, A., Liu, Z., Norouzi, H., Pai, D.S., 2018. A preliminary assessment of GPM-based multi-satellite precipitation estimates over a monsoon dominated region. J. Hydrol. 556, 865–876. https://doi.org/10.1016/j.jhydrol.2016.01.029

Prakash, S., Mitra, A.K., Pai, D.S., AghaKouchak, A., 2016. From TRMM to GPM: How well can heavy rainfall be detected from space? Adv. Water Resour. 88, 1–7. https://doi.org/10.1016/j.advwatres.2015.11.008

Prasannakumar, V., Vijith, H., Abinod, S., Geetha, N., 2012. Estimation of soil erosion risk within a small mountainous sub-watershed in Kerala, India, using Revised Universal Soil Loss Equation (RUSLE) and geo-information technology. Geosci. Front. 3, 209–215. https://doi.org/10.1016/j.gsf.2011.11.003

Premlal, 1986. Development of an erosivity map for SriLanka. Report submitted by Department of Agricultural Engineering, University.

Rahman, A.S., Rahman, A., Zaman, M.A., Haddad, K., Ahsan, A., Imteaz, M., 2013. A study on selection of probability distributions for at-site flood frequency analysis in Australia. Nat. Hazards 69, 1803–1813. https://doi.org/10.1007/s11069-013-0775-y

Raj, R., Saharia, M., Chakma, S., Rafieinasab, A., 2022. Mapping rainfall erosivity over India using multiple precipitation datasets. Catena 214, 106256. https://doi.org/10.1016/j.catena.2022.106256

Reddy, M.V., Mitra, Ashis K., Momin, I.M., Mitra, Ashim K., Pai, D.S., 2019. Evaluation and inter-comparison of high-resolution multi-satellite rainfall products over India for the southwest monsoon period. Int. J. Remote Sens. 40, 4577–4603. https://doi.org/10.1080/01431161.2019.1569786

Renard, K.., Freimund, J.., 1994. Using monthly precipitation data to estimate the R-factor in the revised USLE. J. Hydrol. 157, 287–306.

Renard, K.G., Foster, G.R., Weesies, G., McCool, D., Yoder, D., 1997. Predicting soil erosion by water: a guide to conservation planning with the Revised Universal Soil Loss Equation (RUSLE), Agricultural Handbook No. 703. US Department of Agriculture, Washington, D.C. https://doi.org/DC0-16-048938-5 65–100.

Renard, K.G., Freimund, J.R., 1994. Using monthly precipitation data to estimate the R-factor in the revised USLE. J. Hydrol. 157, 287–306.

Roose, E.J., 1975. Erosion et ruisellement en Afrique de l’ouest:vingt annees de mesures en petites parcelles experimentales. Cyclo. ORSTOM.

Sadeghi, S.H., Zabihi, M., Vafakhah, M., Hazbavi, Z., 2017. Spatiotemporal mapping of rainfall erosivity index for different return periods in Iran. Nat. Hazards 87, 35–56. https://doi.org/10.1007/s11069-017-2752-3

Sadeghi, S.H.R., Hazbavi, Z., 2015. Trend analysis of the rainfall erosivity index at different time scales in Iran. Nat. Hazards 77, 383–404. https://doi.org/10.1007/s11069-015-1607-z

Salleh, F.H.M., Zainudin, S., Arif, S.M., 2017. Multiple linear regression for reconstruction of gene regulatory networks in solving cascade error problems. Adv. Bioinformatics 2017, 14. https://doi.org/10.1155/2017/4827171

Samarinas, N., Tsakiridis, N.L., Kalopesa, E., Zalidis, G.C., 2024. Soil Loss Estimation by Water Erosion in Agricultural Areas Introducing Artificial Intelligence Geospatial Layers into the RUSLE Model. Land 13. https://doi.org/10.3390/land13020174

Sarma, A.K., Chandramouli, V., Singh, B., Goswami, P., Rajbongshi, N., 2005. Urban Flood Hazard Mitigation of Guwahati City by Silt monitoring and watershed modeling. Report submitted to Ministry of Human Resources Department (MHRD) by Deptt. of Civil Engineering, IIT Guwahati.

Sarma, A.K., Sarma, B., Das, S., 2016. Estimating Sustainable Carrying Capacity of Flood Prone Hilly Urban Areas, in: Urban Hydrology, Watershed Management and Socio-Economic Aspects. pp. 289–304. https://doi.org/10.1007/978-3-319-40195-9

Sarma, B., Sarma, A.K., 2016. Optimal Allocation of Ecological Management Practices in a Hilly Urban Watershed, in: Urban Hydrology, Watershed Management and Socio-Economic Aspects. pp. 35–47. https://doi.org/10.1007/978-3-319-40195-9

Sarma, B., Sarma, A.K., Mahanta, C., Singh, V.P., 2015. Optimal ecological management practices for controlling sediment yield and peak discharge from hilly urban areas. J. Hydrol. Eng. 20, 1–14. https://doi.org/10.1061/(ASCE)HE.1943-5584.0001154

Sarma, B., Sarma, A.K., Singh, V.P., 2013. Optimal Ecological Management Practices (EMPs) for Minimizing the Impact of Climate Change and Watershed Degradation Due to Urbanization. Water Resour. Manag. 27, 4069–4082. https://doi.org/10.1007/s11269-013-0396-y

Sen, P.K., 1968. Estimates of the regression coefficient based on Kendall’s Tau. J. Am. Stat. Assoc. 63, 1379–1389.

Shamshad, A., Azhari, M.N., Isa, M.H., Hussin, W.M.A.W., Parida, B.P., 2008. Development of an appropriate procedure for estimation of RUSLE EI30index and preparation of erosivity maps for Pulau Penang in Peninsular Malaysia. Catena 72, 423–432. https://doi.org/10.1016/j.catena.2007.08.002

Sharda, V.N., Ojasvi, P.R., 2006. Development of daily rainfall erosivity model for sub-humid climate of outer Himalayas. Indian J. Soil Conserv. 199–203.

Sheikh, a H., Palria, S., Alam, A., 2011. Integration of GIS and Universal Soil Loss Equation (USLE) for soil loss estimation in a Humalayan Watershed. Recent Res. Sci Tech. 3, 51–57.

Shiono, T., Ogawa, S., Miyamoto, T., Kameyama, K., 2013. Expected impacts of climate change on rainfall erosivity of farmlandsin Japan. Ecol. Eng. 61, 678–689. https://doi.org/10.1016/j.ecoleng.2013.03.002

Shit, P.K., Nandi, A.S., Bhunia, G.S., 2015. Soil erosion risk mapping using RUSLE model on jhargram sub-division at West Bengal in India. Model. Earth Syst. Environ. 1, 28 (1–12). https://doi.org/10.1007/s40808-015-0032-3

Singh, A.K., Singh, V., Singh, K.K., Tripathi, J.N., Kumar, A., Soni, A.K., Sateesh, M., Khadke, C., 2018. A Case Study: Heavy Rainfall Event Comparison Between Daily Satellite Rainfall Estimation Products with IMD Gridded Rainfall Over Peninsular India During 2015 Winter Monsoon. J. Indian Soc. Remote Sens. 46, 927–935. https://doi.org/10.1007/s12524-018-0751-9

Singh, A.K., Tripathi, J.N., Singh, K.K., Singh, V., Sateesh, M., 2019. Comparison of different satellite-derived rainfall products with IMD gridded data over Indian meteorological subdivisions during Indian Summer Monsoon (ISM) 2016 at weekly temporal resolution. J. Hydrol. 575, 1371–1379. https://doi.org/10.1016/j.jhydrol.2019.02.016

Singh, G., Babu, R., Chandra, S., 1981. Soil Loss Prediction Research in India. Cent. Soil Water Conserv. Res. Train. Institute, Dehradun Bulletin Nos. T-12/D-9.

Singh, J., Singh, O., 2020a. Assessing rainfall erosivity and erosivity density over a western Himalayan catchment, India. J. Earth Syst. Sci. 129. https://doi.org/10.1007/s12040-020-1362-8

Singh, J., Singh, O., 2020b. Exploring seasonality and erosivity of rainfall over a lower Himachal Himalayan catchment, India. Arab. J. Geosci. 13. https://doi.org/10.1007/s12517-020-05679-y

Singh, M.C., Sur, K., Al-Ansari, N., Arya, P.K., Verma, V.K., Malik, A., 2023. GIS integrated RUSLE model-based soil loss estimation and watershed prioritization for land and water conservation aspects. Front. Environ. Sci. 11. https://doi.org/10.3389/fenvs.2023.1136243

Sinha, D., Joshi, V.U., 2012. Application of universal soil loss equation (USLE) to recently reclaimed badlands along the Adula and Mahalungi Rivers, Pravara Basin, Maharashtra. J. Geol. Soc. India 80, 341–350. https://doi.org/10.1007/s12594-012-0152-6

Smithen, A.A., Schulze, R.E., 1982. The Spatial Distribtion in Southern Africa of Rainfall Erosivity for Use in the USLE. Water SA 8, 74–78.

Socolofsky, S., Adams, E., Entekhabi, D., 2001. Disaggregation of daily rainfall for continuous watershed modeling. J. Hydrogic Eng. 6, 300–309.

Stocking, M.A., 2001. Land Degradation. Int. Encycl. Soc. Behav. Sci.

Stocking, M.A., Elwell, H.A., 1976. Rainfall erosivity over Rhodesia. Trans. Inst. Br. Geogr. 1, 231–245.

Taguas, E. V., Carpintero, E., Ayuso, J.L., 2011. Assessing land degradation risk through the long-term analysis of erosivity: A case study in Southern Spain. L. Degrad. Dev. 24, 179–187. https://doi.org/10.1002/ldr.1119

Tayşi, H., Özger, M., 2022. Disaggregation of future GCMs to generate IDF curves for the assessment of urban floods. J. Water Clim. Chang. 13, 684–706. https://doi.org/10.2166/wcc.2021.241

Teng, H., Ma, Z., Chappell, A., Shi, Z., Liang, Z., Yu, W., 2017. Improving rainfall erosivity estimates using merged TRMM and gauge data. Remote Sens. 9. https://doi.org/10.3390/rs9111134

Thakur, M.K., Desamsetti, S., Naga Rajesh, A., Koteswara Rao, K., Narayanan, M.S., Lakshmi Kumar, T. V., 2020a. Exploring the rainfall data from satellites to monitor rainfall induced landslides – A case study. Adv. Sp. Res. 66, 887–894. https://doi.org/10.1016/j.asr.2020.05.015

Thakur, M.K., Kumar, T.V.L., Narayanan, M.S., Kundeti, K.R., Barbosa, H., 2020b. Analytical study of the performance of the IMERG over the Indian landmass. Meteorol. Appl. 27, 1–11. https://doi.org/10.1002/met.1908

Tirkey, A., Pandey, A.C., Nathawat, M.S., 2013. Use of Satellite Data , GIS and RUSLE for Estimation of Average Annual Soil Loss in Daltonganj Watershed of Jharkhand (India) 20–30. https://doi.org/10.18005/JRST0101004

Tiwari, H., Rai, S.P., Kumar, D., Sharma, N., 2016. Rainfall erosivity factor for India using modified fourier index. J. Appl. Water Eng. Res. 4, 83–91. https://doi.org/10.1080/23249676.2015.1064038

Torri, D., Borselli, L., Guzzetti, F., Calzolari, M.C., Bazzoffi, P., Ungaro, F., Bartolini, D., Salvador, M.P.S., 2006. Italy, in: Boardman, J., Poesen, J. (Eds.), Soil Erosion in Europe. John Wiley & Sons Ltd., Chichester, United Kingdom, pp. 245–261.

Towheed, A., Roshni, T., 2021. Linking climate change to soil loss estimation in the kosi river basin, India. J. Water Clim. Chang. 12, 2338–2363. https://doi.org/10.2166/wcc.2021.259

USDA-Agricultural Research Service, 2013. Science Documentation Revised Universal Soil Loss Equation Version 2. https://doi.org/https://www.ars.usda.gov/ARSUserFiles/60600505/RUSLE/RUSLE2_Science_Doc.pdf

Vantas, K., Sidiropoulos, E., Loukas, A., 2020. Estimating current and future rainfall erosivity in greece using regional climate models and spatial quantile regression forests. Water (Switzerland) 12, 1–20. https://doi.org/10.3390/w12030687

Verma, P., Ghosh, S.K., 2018. Study of GPM-imerg rainfall data product for gangotri glacier. Int. Arch. Photogramm. Remote Sens. Spat. Inf. Sci. - ISPRS Arch. 42, 383–388. https://doi.org/10.5194/isprs-archives-XLII-5-383-2018

Volpi, E., Fiori, S., Grimaldi, S., Lombardo, F., Koutsoyiannis, D., 2015. One hundred years of return period: Strengths and limitations. Water Resour. Res. 51, 8570–8585. https://doi.org/10.1111/j.1752-1688.1969.tb04897.x

Vrieling, A., Hoedjes, J.C.B., van der Velde, M., 2014. Towards large-scale monitoring of soil erosion in Africa: Accounting for the dynamics of rainfall erosivity. Glob. Planet. Change 115, 33–43. https://doi.org/10.1016/j.gloplacha.2014.01.009

Vrieling, A., Sterk, G., Jong, S.M.., 2010. Satellite-based estimation of rainfall erosivity for Africa. J. Hydrol. 395, 235–241.

Wang, W., Yin, S., He, Z., Chen, D., Wang, H., Klik, A., 2023. Projections of rainfall erosivity in climate change scenarios for mainland China. Catena 232, 107391. https://doi.org/10.1016/j.catena.2023.107391

Wilks, D.S., 1993. Comparisoonf Three-ParametePr robabilityD istributionsfo r Representing Annual Extreme and Partial Duration Precipitation Series. Water Resour. Res. 29, 3543–3549.

Wischmeier, W.H., 1959. A Rainfall Erosion Index for a Universal Soil-Loss Equation. Soil Sci. Soc. Am. J. 23, 246–249. https://doi.org/10.2136/sssaj1959.03615995002300030027x

Wischmeier, W.H., Smith, D.D., 1978. Predicting rainfall erosion losses - A guide to conservation planning, Agricultural Research Service Handbook No. 537. USDA, Washington, D.C. https://doi.org/10.1029/TR039i002p00285

Wischmeier, W.H., Smith, D.D., 1958. Rainfall energy and its relationship to soil loss. Eos, Trans. Am. Geophys. Union 39, 285–291. https://doi.org/10.1029/TR039i002p00285

Xie, P., Xiong, A.Y., 2011. A conceptual model for constructing high-resolution gauge-satellite merged precipitation analyses. J. Geophys. Res. Atmos. 116, 1–14. https://doi.org/10.1029/2011JD016118

Xie, Y., Yin, S. qing, Liu, B. yuan, Nearing, M.A., Zhao, Y., 2016. Models for estimating daily rainfall erosivity in China. J. Hydrol. 535, 547–558. https://doi.org/10.1016/j.jhydrol.2016.02.020

Xin, Z., Yu, X., Li, Q., Lu, X.X., 2011. Spatiotemporal variation in rainfall erosivity on the Chinese Loess Plateau during the period 1956-2008. Reg. Environ. Chang. 11, 149–159. https://doi.org/10.1007/s10113-010-0127-3

Xu, J., Ma, Z., Tang, G., Ji, Q., Min, X., Wan, W., Shi, Z., 2019. Quantitative evaluations and error source analysis of fengyun-2-based and gpm-based precipitation products over mainland China in summer, 2018. Remote Sens. 11. https://doi.org/10.3390/rs11242992

Xu, J., Zhu, S., Ma, Z., Liu, H., Shangguan, Y., Yang, Y., 2021. Calibrating GPM IMERG Late-Run product using ground-based CPC daily precipitation data: a case study in the Beijing-Tianjin-Hebei urban agglomeration. Remote Sens. Lett. 12, 848–858. https://doi.org/10.1080/2150704X.2021.1942576

Xu, L., Xie, Y., Fu, S.H., Liu, B.Y., Lu, B.J., Yuan, A.P., 2007. Simple method of estimating rainfall erosivity under different rainfall amount of Beijing. Res. Soil Water Conserv. 6, 398–402.

Xu, L., Xu, X., Meng, X., 2013. Risk assessment of soil erosion in different rainfall scenarios by RUSLE model coupled with Information Diffusion Model: A case study of Bohai Rim, China. Catena 100, 74–82. https://doi.org/10.1016/j.catena.2012.08.012

Yang, D., Kanae, S., Oki, T., Koike, T., Musiake, K., 2003. Global potential soil erosion with reference to land use and climate changes. Hydrol. Process. 17, 2913–2928. https://doi.org/10.1002/hyp.1441

Yang, X., Yu, B., Xie, X., 2015. Predicting changes of rainfall erosivity and hillslope erosion risk across greater Sydney region, Australia. Int. J. Geospatial Environ. Res. 2, 2.

Yesuph, A.Y., Dagnew, A.B., 2019. Soil erosion mapping and severity analysis based on RUSLE model and local perception in the Beshillo Catchment of the Blue Nile Basin, Ethiopia. Environ. Syst. Res. 8, 1–21. https://doi.org/10.1186/s40068-019-0145-1

Yu, B., Hashim, G.M., Eusof, Z., 2001. Estimating the R-factor with limited rainfall data: a case study from peninsular Malaysia. J. Soil Water Conserv. 56, 101–105.

Yusof, K.W., Ahmad, M.H., 2016. Evaluation of rainfall-runoff erosivity factor for cameron highlands , pahang , malaysia. J. Ecol. Eng. 17, 1–8. https://doi.org/10.12911/22998993/63338

Zhang, W.B., Xie, Y., Liu, B.Y.., 2002. Rainfall erosivity estimation using daily rainfall amounts. Sci. Geogr. Sin. 22, 705–711.

Zhou, J., Bao, Y., He, X., Wen, A., Jiang, G., Long, Y., Li, J., 2023. Risk analysis of rainfall erosion on upland adjacent to riparian zone of the Three Gorges Reservoir. Catena 232, 107458. https://doi.org/10.1016/j.catena.2023.107458

Zhu, Q., Chen, X., Fan, Q., Jin, H., Li, J., 2011. A new procedure to estimate the rainfall erosivity factor based on Tropical Rainfall Measuring Mission (TRMM) data. Sci. China Technol. Sci. 54, 2437–2445. https://doi.org/10.1007/s11431-011-4468-z

Figure – Photographs captured during manual extraction of 19 years half hourly data at the office of IMD Guwahati

List of Publication

Journals

1. **Tapasranjan Das** and Arup Kumar Sarma (2025). Incorporating return period in the assessment of rainfall erosivity of India using high temporal resolution satellite precipitation product. *Journal of Earth System Science*, 134, 10. https://doi.org/10.1007/s12040-024-02452-7
2. **Tapasranjan Das** and Arup Kumar Sarma (2025). Climate change impact on rainfall erosivity factor using disaggregation model under CMIP6 shared socio-economic pathways. *Theoretical and Applied Climatology*, 156, 381. https://doi.org/10.1007/s00704-025-05608-7
3. **Tapasranjan Das** and Arup Kumar Sarma (2026). Development of a rainfall erosivity computation model for an Eastern Himalayan City to study the effect of climate change under CMIP6 socio-economic pathways. Acta Geophysica. Springer Nature (Under review)

Under Preparation

1. Spatiotemporal variations of rainfall erosivity over Mainland India
2. IMDMERG - A 20 years 0.25-degree half hourly interval high resolution rainfall dataset (2001 to 2020) for Mainland India

Conferences

1. **Tapasranjan Das** and Arup Kumar Sarma (2020) "Estimation of rainfall erosivity factor of Guwahati with high temporal resolution rainfall data". Proceedings of 25th International Conference on Hydraulics, Water Resources and Coastal Engineering, HYDRO 2020 INTERNATIONAL, 26th -28th March, 2021, NIT Rourkela, India. (**Best Presentation Award**).
2. **Tapasranjan Das** and Arup Kumar Sarma (2020), "Return period analysis of rainfall erosivity", (H005-0003) presented at 2020 AGU, Fall Meeting, 1-17 Dec.
3. **Tapasranjan Das** and Arup Kumar Sarma (2022), "Trend analysis of rainfall erosivity of India", (H51E-07) presented at 2022 AGU, Fall Meeting, 12-16 Dec.